EVALUATION OF FATIGUE BEHAVIOUR OF LASER BEAM WELDED AEROSPACE SUPERALLOY HAYNES 282

By

Richard Apreku Buckson

A Thesis Submitted to the Faculty of Graduate Studies of
The University of Manitoba
in partial fulfillment of the requirements of the degree of

Doctor of Philosophy

Department of Mechanical Engineering
University of Manitoba
Winnipeg, Manitoba

Abstract

In 2005, a new, wrought, nickel-base superalloy Haynes 282 was developed. Characteristic of superalloys, Haynes 282 was produced to be used for components, specifically aero and land-based gas turbine engines, which are subjected to high temperatures. The manufacture and/or repair of aero and land-based gas turbine engines require the use of joining processes, an example being welding. However, it was observed that laser beam welding (LBW) of the new superalloy resulted in cracking in the heat affected zone (HAZ) of the alloy. Accordingly, an aspect of this research involves the development of a procedure for preventing or minimizing cracking of the alloy. This is achieved through microstructural modification of the alloy prior to welding through the use of appropriate heat treatment. However, at the core of this research is the main objective of methodically studying the effect of LBW on the high temperature fatigue crack growth (FCG) behaviour of Haynes 282, and how to mitigate any negative effects. Findings from this research show that LBW causes a deleterious effect on the FCG behaviour by increasing the FCG rate. Thus, although this research resulted in a procedure that minimizes cracking during welding of the new alloy, the minimized level of cracking is not tolerable under dynamic loading. Therefore, a procedure to make the minimized level of cracking tolerable during dynamic service is developed. This is achieved by developing two post weld heat treatments, including a new thermal treatment schedule developed in this work, which significantly improved the FCG resistance of the new alloy after LBW. Additionally, Low cycle fatigue (LCF) tests results indicate strong fatigue deformation resistance of Haynes 282. On the other hand, FCG tests results show that, in contrast to common assumption, the loading frequency was observed to have an effect on the FCG behaviour at room temperature. Prior to this research, there was limited publication on the fatigue behaviour of Haynes 282. Hence, the study of the cyclic deformation characteristics and growth behaviour of

fatigue crack in Haynes 282 in this research provides valuable information that helps establish design criteria to safeguard against component failure by fatigue.

Acknowledgments

I immensely thank my supervisor, Dr. O.A. Ojo, for his valuable research contribution, guidance, support and encouragement towards this research project. Furthermore, I extend my appreciation to my advisory committee members, Drs. N. Bassim and A. Shalaby, for their indispensable support and advice during the pursuit of this project.

I am grateful to Haynes International Incorporation, USA, for the supply of test materials and Standard Aero Ltd, Winnipeg, Canada for welding the materials.

I received immense technical assistance from Don Madis, Mike Boswisk, Dr. Khan and Jon Van Dorp. I thank all of them for their support. I would also like to thank my colleagues and friends – Dr. Lawrence Oshoba, Dr. Oyedele Ola, Mark Amegadzie, and Omudhohwo Oshobe.

I extend my special gratitude to my fiancée, Nana Tsiquayeaba, for being my backbone during stressful times and urging me on with her encouraging words. She made the journey look easier even when the destination seemed out of reach.

Dedication

This dissertation is dedicated to my parents, Mr. & Mrs. Buckson, and my fiancée, Nana Tsiquayeaba.

TABLE OF CONTENTS

List of Tables

List of Figures

List of Copyrighted Materials for which permission was obtained

CHAPTER 1

INTRODUCTION

1.1 General Overview

The aerospace industry is a significant component of the economy of any nation. In Canada, it is an essential sector of its economy, a top employer, and a major contributor to research and development [1].

Aerospace manufacturing constitutes an important segment in the aerospace industry. It involves the use of advanced technology to develop guided missiles, space vehicles, aircraft, aircraft engines, propulsion units, and associated parts [2]. A characteristic feature of aircraft gas turbines and rocket engines is their high temperature operating environment. This necessitates the use of appropriate heat resistant materials that can withstand the operating demands from the high temperature environment. As a result, the aerospace industry relies heavily on the use of superalloys for the fabrication of aircraft gas turbines and rocket engines.

Superalloys are a group of heat-resistant alloys developed for the manufacture of components subjected to high temperatures. They have high strength and good resistance to corrosion at high temperatures. The present research focuses on Haynes 282 which is a new (introduced in the fall of 2005) [3], wrought, gamma prime precipitation strengthened nickel-based superalloy developed for high temperature structural applications such as aero and land- based gas turbine engines. An attractive characteristic of Haynes 282 is its combination of high creep strength, high thermal stability, and good fabricability [4] compared to existing superalloys such as IN 718 and Waspaloy.

Typical of materials used in the design of equipment and structural components employed in advanced engineering applications, Haynes 282 is subjected to fluctuating (cyclic) stresses during its service life. Consequently, it is susceptible to various types of fatigue failure, amongst which are strain-controlled low cycle fatigue (LCF) and fatigue crack growth (FCG).

Strain-controlled LCF can be a primary consideration in the design of products for industrial purposes [5] and salient LCF data are often necessary for the establishment of design criteria to safeguard against component failure by fatigue. Strain-controlled LCF mainly focuses on the resistance to fatigue crack initiation and early crack growth [6]. However, for some manufactured components, pre-existing flaws and sharp design features can substantially decrease or nearly eliminate the crack initiation portion of the fatigue life of the component. Hence, the useful life of such components are governed by the rate of the FCG [7]. Hence, to obtain a complete picture of the fatigue performance of a material, it is useful to study both the strain-controlled LCF and FCG behaviour of the material. Nevertheless, it is commonly assumed that all parts contain pre-existing cracks. Consequently, research on life prediction or service extension of components made from superalloys has been primarily centered on their FCG characteristics [8].

Several factors can affect the rate of fatigue crack propagation; stress ratio, frequency and temperature of the environment are examples [8]. Consequently, the present research focuses on the effects of LBW, stress ratio, frequency, and temperature on the FCG behaviour of Haynes 282.

Welding is an attractive, economical and commonly used joining method used for the fabrication of new components and/or the repair of damaged components. LBW is a type of high energy beam welding technique, which melts and joins metal by heating them with a laser beam. The major advantages which distinguish LBW from others include are: production of deep and narrow welds

at high welding speeds, narrow heat affected zone, little distortion of joined pieces, and welding of dissimilar metals in varying sizes.

1.2 Research Objective

Since the application of welding as a fabrication or repair method can potentially influence the fatigue behaviour of welded components, it is important to study the fatigue behaviour of welded Haynes 282. Accordingly, the main objective of this PhD thesis was to determine the effect of LBW on the high temperature FCG behaviour of Haynes 282 superalloy and to develop procedures to mitigate any deleterious effects resulting. Therefore, the knowledge generated will help in improving fatigue properties of both unwelded and laser welded Haynes 282 which ultimately will lead to high reliability and superior performance of components made from it.

1.3 Major Findings

Prior to this work, publication on the fatigue behaviour of Haynes 282 superalloy was scarce. This research provides useful information on the fatigue behaviour of Haynes 282 both in the unwelded and welded conditions.

LCF test results showed that the stress response of Haynes 282 during cyclic deformation consisted of an initial cyclic hardening followed by a regime of cyclic softening to specimen failure. This gives an indication on the path that the new alloy arrives at its final flow stress level, hence is useful in determining appropriate loading for the alloy during service. Additionally, the cyclic

deformation parameters indicated that Haynes 282 has high fatigue deformation resistance. On the other hand, FCG test results showed that an increase in the stress ratio led to a rise in the FCG rate. However, contrary to common assumptions, the loading frequency was observed to affect the FCG behaviour at room temperature (25°C). Furthermore, an increase in temperature from 25°C to 600°C at a testing frequency of 15 Hz resulted in an increase in the FCG at all stress intensities. However, at a frequency of 0.05 Hz and over a relatively large stress intensity range (ΔK), the FCG rate decreased with increasing in temperature.

Microstructural analysis of laser beam welded Haynes 282 specimens showed evidence of cracking in the HAZ. Hence, prior to performing fatigue test on welded specimens, it was necessary that a procedure be developed to prevent or minimize cracking of the alloy. This was achieved through microstructural modification of the alloy through pre-weld heat treatments. Based on the results of the crack measurements performed in this work, the optimum pre-weld heat treatment that minimized cracking was found to be 1100°C/2 h/furnace cooling. However, it was determined from subsequent FCG tests performed on welded specimens that the minimized level of cracking achieved using 1100°C/2 h/furnace cooling was not tolerable under dynamic loading. Therefore, a procedure to make the minimized level of cracking tolerable during dynamic loading was developed. This was achieved by developing two post weld heat treatments which in this research have been identified as Heat Treatment B (solution heat treatment of 1150°C/2 h/water-cool, followed by ageing heat treatments of 1010°C/2 h/air-cool and 788°C/8 h/air-cool) and Heat Treatment C (solution heat treatment 1130°C/2 h/water-cool, followed by ageing heat treatments of 1010°C/2 h/air-cool and 788°C/8 h/furnace-cool).

1.4 Thesis Organization

This thesis is composed of five chapters. Chapter 1 provides a brief background of the subject matter and delves into the significance of the present study. Chapter 2 consists of a literature review of the physical and welding metallurgy of nickel-based superalloys in general, followed by a detailed review of Haynes 282. The concept of fatigue and its relevance is also elaborated. Chapter 3 presents the details of the experimental procedures and instruments used. Chapter 4 presents and discusses the results of the experimental work. Chapter 5 provides a summary of the major findings and conclusions as well as suggestions for future work.

CHAPTER 2

LITERATURE REVIEW

This chapter provides a review of the literature on the physical metallurgy of nickel-based superalloys in general, followed by a comprehensive review of the metallurgy of Haynes 282. Subsequently, the concept of fatigue, parameters that define the fatigue of a material, and the factors that influence fatigue are discussed. This is followed by a review of selected welding processes, welding metallurgy, and the fatigue of welded components.

2.1 Superalloys

Superalloys can be broadly classified into two classes: precipitation or age strengthened alloys, and solid solution-strengthened alloys [6]. The main distinguishing feature between these two classes is with regards to the manner through which the alloy is strengthened. For precipitation strengthened alloys, the presence of the hardening phase, gamma prime (ɣ′), is responsible for the strengthening of the alloy. On the other hand, strengthening of solid solution-strengthened alloys is a 'function' of different elements combined to form the alloy. Furthermore, while precipitation strengthened alloys have superior strength at high temperatures, solid solution strengthened alloys possess better fabricability and are usually less expensive [6]. For highly demanding applications, such as hot sections of gas turbine engines, precipitation strengthened alloys are employed [6].

Precipitation strengthened alloys could be nickel-, iron-nickel-, or cobalt-based**.** Usually, gas turbine engine structural components are fabricated out of materials that are nickel-based or iron-

nickel-based precipitation strengthened superalloys. As mentioned previously, the present research focuses on the use of a wrought, nickel-based precipitation-strengthened superalloy, Haynes 282.

2.2 Microstructure of Wrought Nickel-Base Superalloys

Nickel-based superalloys are alloys of nickel (Ni), chromium (Cr) and cobalt (Co), and also contain minute amounts of ten or more other elements**.** The amount of these elements varies from alloy to alloy; consequently, there is a certain degree of variability in the microstructure of wrought nickel-based superalloys [9]. Nevertheless, there are major phases that are generally representative of all wrought superalloys. The impact of these phases on the mechanical and physical properties are discussed in subsequent subsections.

2.2.1 The Gamma (ɣ) Phase

The gamma (ɣ) phase is an austenitic face centered cubic (FCC) matrix that usually contains a high percentage of solid solution elements, such as molybdenum (Mo), cobalt (Co), aluminum (Al), chromium (Cr), titanium (Ti), tungsten (W) and niobium (Nb). These elements differ from Ni in atomic diameter by 1-18% and typically occupy substitutional atomic positions in nickel crystal lattices [9]. This leads to a distorted lattice with a spherical symmetrical stress field. The interaction of this stress field with that around a dislocation produces an elastic solute atom-dislocation interaction that leads to solid solution strengthening. In essence, the interaction of the stress fields around solute atoms and dislocations increases the stress required to move a dislocation by a quantity given by Mott and Nabarro [10-11] as:

$$\Delta\sigma = G\delta^{4/3}c\left[\frac{c^{2/3}}{2\pi}\left(In\,\frac{1}{c}\right)^{4}\right]^{1/3} \quad \text{.....(2.1)}$$

where δ is the lattice misfit, *G* is the modulus, σ is the stress and '*c*' is the solute concentration.

Besides improving strength, the Ni-ɣ phase has the ability to withstand harsh temperatures and time excursions [9]. This capability is attributed to various factors such as:

1) the high tolerance of Ni for alloying without phase instability due to its nearly filled third electron shell [11].
2) the tendency of elemental Cr addition to form Cr_2O_3 – a rich protective scale with low cation vacancy content, thereby restricting the diffusion rate of metallic elements outwards, and preventing the diffusion of non-metallic elements, such as oxygen (O), nitrogen (N) and sulphur (S) inward [11].
3) the strong tendency to form Al_2O_3 – a rich scale with excellent resistance to oxidation similar to that of Cr_2O_3 [12].

2.2.2 Gamma Prime (ɣ')

The precipitation of ɣ′ – an FCC LI_2 ordered intermetallic compound Ni_3 (Al, Ti) - is responsible for the high temperature strength of nickel-based superalloys [9]. Figure 2.1 shows a typical unit cell of the LI_2 crystal structure of the ɣ′ phase. The ɣ′ particle forms in alloys that contain Ti and Al in quantities that are above its solubility in nickel rich ɣ matrix as a coherent precipitate phase.

Besides Al and Ti serving as the major constituents of the ɣ′ phase, it has been suggested that the ɣ′ phase may also contain several other solute elements in trace amounts, which results in more

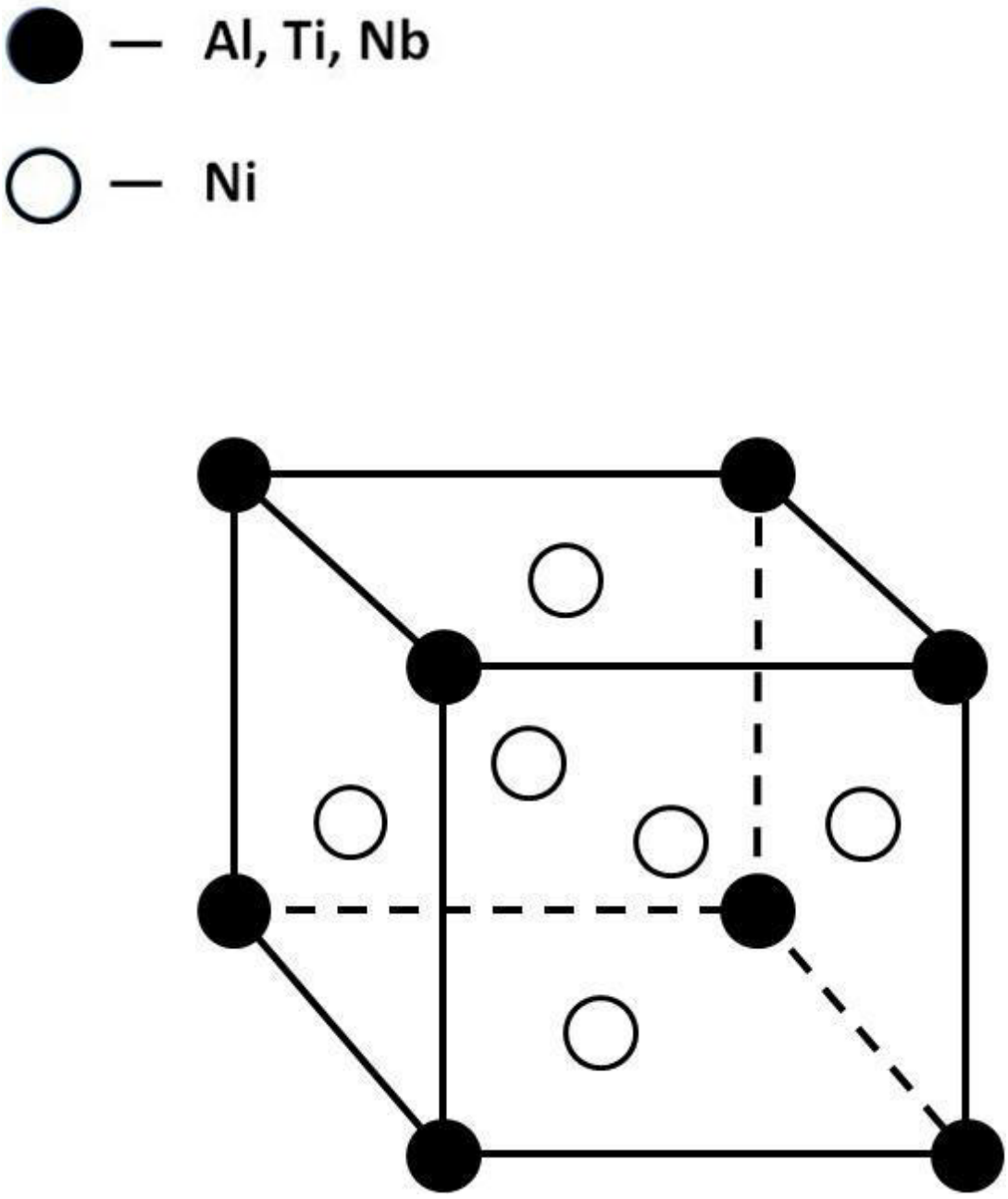

Figure 2.1 unit cell showing LI_2 ordered FCC lattice of ɣ' phase

complex chemical compositions [9]. Although the ɣ′ precipitate is coherent with the matrix, a small misfit at the ɣ-ɣ′ interface exists [13]. The magnitude of this misfit is known to influence the morphology of ɣ′ precipitate [14]. On the other hand, the mechanical properties of nickel-based superalloys are strongly influenced by the morphology, distribution and size of ɣ′ precipitates within the ɣ matrix [9].

Interactions between the ɣ′ particles and moving dislocations can influence the strength of the material. If the particle size is small, there is a tendency for moving dislocations to shear the particle, whereas when the particle is large, it is by-passed. In the event that the precipitates are sheared under applied strain (compressive or tensile), the strength of a ɣ′ precipitation strengthened nickel-based alloy will then depend on (i) order hardening and (ii) coherency hardening [9].

2.2.2.1 Order Hardening

Strengthening of a material through the phenomenon of order hardening occurs when the ordered ɣ′ coherent precipitates are sheared by a glide dislocation that moves through the matrix, thus creating an anti-phase boundary (APB) fault on the slip plane of the precipitate phase in the process [9]. In essence, pairs of dislocation that travel through a ɣ-ɣ′ system shear the ɣ′ phase particles which leads to the formation of APB. The first dislocation is followed by the second dislocation that restores the order in the sheared particles by removing the APB that was formed by the first. Eventually, the amount of energy required for dislocations to pass through precipitates increases due to an ordering effect which is created in the ɣ-ɣ′ system by the dislocations that shear the ɣ′ precipitate phase [15]. Therefore, higher APB energy means higher forces required for dislocations to shear through the alloy matrix. Nickel-based superalloys with high volume fraction of ɣ′ exhibit

a significant increase in strength with increasing temperature up to 800°C. This is due to the increase in the degree of ordered hardening with increase in temperature [16]. For a single dislocation, the increase in strength is given by Brown [17] as:

$$\Delta\tau = \gamma_0^{3/2} / 2b[4\, fr/\, \pi\Gamma]^{1/2} \quad \text{.....(2.2)}$$

and for a dislocation pair

$$\Delta\tau = \gamma_0^{3/2} / 2b\{[4\gamma_o fr/\pi\Gamma]^{1/2} - f\} \quad \text{.....(2.3)}$$

where γ_o is the specific APB energy, *r* is the average dimension of the particle intersected by a slip band, *b* is the Burgers vector of the matrix, *f* is the volume fraction of the precipitates and Γ is the line tension of dislocation.

2.2.2.2 Coherency Hardening

The interaction of glide dislocations with the elastic coherency strain field around coherent γ′ precipitates leads to a phenomenon known as coherency hardening, which is also known as misfit hardening [9]. In essence, the coherent strain field around a precipitate makes it difficult for glide dislocation to penetrate the γ′ precipitates during both γ′ cutting and by-passing situations encountered during deformation. The strain field is a result of the lattice misfit measured as the degree of disregistry between the γ and the γ′ phases. The interaction of this strain field and glide dislocations ultimately increases the critical resolved shear stress (CRSS) required by a moving dislocation to cut through or by-pass a particle [18]. For coherency hardening, the increase in yield strength or the CRSS $\Delta\tau_{CRSS}$ is given as:

$$\Delta\tau_{CRSS} = 3G_{\Sigma^{3/2}} \left[\frac{hf}{2b}\right]^{1/2} \quad \text{.....(2.4)}$$

where G is the modulus, ε is the constrained lattice strain and h is the mean particle diameter. b and f are as defined in equations (2.2) and (2.3).

2.2.2.3 Dislocation By-passing of ɣ′

The size of the ɣ′ precipitate also has an influence on the strength of precipitation strengthened nickel-based superalloys [9]. The tendency for a moving dislocation to by-pass large ɣ′ particles, either by looping or dislocation climb becomes considerably higher as the size of the ɣ′ particles increase. The chemistry of an alloy determines the critical size for the change in mechanism from cutting into by-passing. The critical size can range from about 300 Å to 2500 Å; alloys that have high Al + Ti, ɣ′ volume fractions have higher sizes. The contribution of the ɣ′ particle by-passing to increase in critical resolved shear strength due to dislocation looping is given by Orowan [18] as:

$$\Delta\tau_{CRSS} = 0.2\ Gb\phi 2/\lambda\ \text{In}\ h/2b \quad \text{.....(2.5)}$$

where h is the mean particle diameter, ϕ is the angle between the Burgers vector and tangent to the dislocation line, λ is the mean interparticle spacing, and G the shear modulus of the matrix lattice. Usually, the relationship in equation (2.5) only applies to particle sizes larger than those observed in conditions that correspond to peak strength [9].

2.2.2.4 Carbides

Carbides form an important part of the microstructure of superalloys [19]. There are several types of carbides that can form in superalloys, and the formation of a particular type of carbide is dependent on the composition of the superalloy. Some examples of carbides are M_6C, MC, M_7C_3 and $M_{23}C_6$. $M_{23}C_6$, and MC carbides are the most common carbides. A list of various carbides found in different nickel based superalloy materials are shown in Table 2.1.

The amount of carbon (C) in wrought nickel-base superalloys varies from 0.02 to about 0.2 percent, and it is the C content that determines the amount of carbides [16]. The combination of C with reactive and refractory elements such as (Ti), tantalum (Ta), Nb and hafnium (Hf) during solidification from melt leads to the formation of a wide range of carbide type. Carbide formation begins once the C concentration exceeds 0.05 wt. % [20]. Characteristically, carbides are hard, relatively stable and vary in sizes that range from a few to hundreds of microns. Additionally, carbides have an FCC structure with no distinct orientation with the matrix and are more brittle than the ɣ matrix. Carbides positively influence high temperature strength, ductility and creep properties of nickel-based alloys when they are present in an optimum amount and are properly distributed along grain boundaries. However, the distribution of carbides in non-preferred morphologies and/or their absence can result in coalescence of voids and excess grain boundary sliding during high temperature deformation and processing. Features that characterize different types of carbides include [19]:

a) Carbide type – MC
   I. MC type carbides are monocarbides with the general formula MC, where ‘M’ stands for metallic elements, such as Ti, Ta, Nb, or W.

Table 2.1 Different types of carbide in Ni-based superalloys [19].

Alloy	Carbides
713 LC	$(Nb_{0.66}Ti_{0.33})C$; $Cr_{23}C_6$
Hastelloy X	$M_{23}C_6$; M_6C
IN-100	Ti(CN) or (Ti, Mo)C; $Cr_{23}C_6$ or $Cr_{21}Mo_2C_6$
Inconel 718	NbC
MAR M-200	(Ti, Nb, W)C; $Cr_{21}Mo_2C_6$; $(NiCo)_3(CrW)_3C$
MAR M-246	(Ti, Ta, Ni)C; $(Ni, Co, W, Cr)_6C$
Nimonic 75	Cr_7C_3
Rene 41	TiC, M_6C, $M_{23}C_6$
Udimet 700	$(Ti_{0.8}Mo_{0.2})C$; $(Cr_{0.85}Mo_{0.09}Ni_{0.03}Ti_{0.02})_{23}C_6$
Waspaloy	TiC; $Cr_{23}C_6$

Source – Metallurgical and Mechanical Properties of Ni-based Superalloy Friction Welds, M.Sc. Thesis by Sathian Sujith (1999). Reprinted with permission from Sathian Sujith's Supervisor, Dr. Tom North, (15th December, 2014).

II. High temperature tensile strength properties are improved through precipitation of MC carbides.

III. It is stable at elevated temperatures.

IV. Precipitation of MC carbides is associated with the effective removal of C from the matrix and thus little C is available for the formation of other carbides (e.g. $M_{23}C_6$).

V. Large amounts of carbide precipitation result into poor weldability.

b) Carbide type – $M_{23}C_6$

$M_{23}C_6$ has a cubic structure and the tendency to form at grain boundary regions [19]. In $M_{23}C_6$ type carbide, the 'M' is usually Cr, but can be replaced by Fe and to a lesser extent by W, Mo or Co [9]. Discrete carbides are relatively more preferred since they pin and limit grain boundary movement [19]. However, continuous carbides are highly deleterious [21]. Within the temperature range of 870°C to 980°C there is continuous carbide formation with the particles having an aspect ratio of 30 to 50 which favours crack nucleation at the interface between the carbide and the matrix [19].

c) Carbide type – M_6C

M_6C has a cubic lattice structure and forms when the Mo and W contents are sufficiently high [9]. M_6C carbides are more stable than $M_{23}C_6$ carbides [19]. It has been shown that when Mo or W exceeds 6-8 wt.% in nickel-base alloys, M_6C together with $M_{23}C_6$ can precipitate along grain boundaries and the composition of these M_6C carbides can widely vary from M_3C to $M_{13}C$ [22]. During the processing of wrought alloy, M_6C carbides have been reported to be more efficient in grain size control, because they are more stable up to a higher temperature than $M_{23}C_6$ carbides [23].

2.3 Haynes 282

Haynes 282 alloy is a unique Ni-Cr-Co-Mo-Al-Ti superalloy [24]. It is a gamma prime precipitation strengthened alloy which is in the class of Rene 41 and Waspaloy. However, it has compositional modifications [3] as shown in Table 2.2. The tensile strength, creep rupture strength, as well as physical properties of the alloy are presented in Tables 2.3 – 2.5, respectively [25].

The major phases in Haynes 282 alloy prior to and after standard heat treatment include primary (γ) phase, MC type carbide and carbonitride [3].

The attributes of Haynes 282 alloy makes it appropriate for critical gas turbine applications, such as sheet fabrications, and cases found in compressor, combustor and turbine sections [4]. Furthermore, in aircraft gas turbines, Haynes 282 is a good candidate for exhaust and nozzle components. In land based gas turbines, it is useful for transition sections and other hot gas path components [4].

2.3.1 Metallurgy of Haynes 282

Haynes 282 has a nominal chemical composition (weight %) of 1.5Al, 2.1Ti, 10Co, 20Cr, 8.5Mo, 1.5Fe, 0.3Mn, 0.15Si, 0.06C, 0.005B, and balance nickel [3]. The 20% Cr content is essential for providing resistance to both oxidation and hot corrosion, while Co is used to regulate the γ′ solvus. Haynes 282 derives its creep strength from its Mo constituent. The hardening phase, γ′, of the alloy is formed from the Al and Ti elements. Minute alterations in the amount of these two elements significantly influence the fabricability and other properties of gamma prime strengthened alloys.

Table 2.2 Chemistry of wrought Haynes alloy 282 and other Ni-base superalloys in its class.

Element	Weight Percent (wt.%)			
	Haynes 282	Waspaloy	Rene 41	Haynes 263
Nickel (Ni)	57 bal.	58 bal.	52 bal.	52 bal.
Chromium (Cr)	20	19	19	20
Cobalt (Co)	10	13.5	11	20
Molybdenum (Mo)	8.5	4.3	10	6
Titanium (Ti)	2.1	3	3.1	2.4 max
Aluminum (Al)	1.5	1.5	1.5	0.6 max
Zirconium (Zr)	-	0.05	-	-
Iron (Fe)	1.5 max	2 max	5 max	0.7 max
Manganese (Mn)	0.3 max	0.1 max	0.1 max	0.4
Silicon (Si)	0.15 max	0.15 max	0.5 max	0.2
Carbon (C)	0.06	0.08	0.09	0.06
Boron (B)	0.005	0.006	0.006	0.005

Table 2.3 Average tensile properties of Haynes 282 alloy* [25].

Temperature °C	0.2% Yield Strength (MPa)	Ultimate Tensile Strength (MPa)	% Elongation	%RA
Room Temp.	715	1147	30	31
600	645	1023	32	33
700	648	983	29	28
800	590	750	26	29
900	404	458	41	56
1000	75	115	77	98

*Solution Annealing: 1135°C + Age-Hardening: 1010°C/2 h/air-cool + 788°C/8 h/air-cool

Source – Alloy digest Haynes 282 (2006). Reprinted with permission from Haynes International, Inc (19th December, 2014).

Table 2.4 Creep-rupture properties of weld metal to base metal of Haynes 282 alloy* [25].

Temperature °C	Stress (MPa)	Material	Time to 1% Creep (h)	Time to Rupture (h)
760	345	Base Metal*	96.8	237.5
		All Weld Metal**	197.0	364.8
927	48	Base Metal*	335.6	792.3
		All Weld Metal**	648.0	950.5

*Solution Annealed + Age-Hardened, **GMAW Welded + Solution Annealed + Age-Hardened

Source – Alloy digest Haynes 282 (2006). Reprinted with permission from Haynes International, Inc (19th December, 2014).

Table 2.5 Mechanical/physical properties of Haynes 282 alloy* [25].

Melting Range	1300-1375°C
Density	8270 Kg/m^3
Thermal Conductivity at 1000°C	28.9 W/m·k
Coefficient of Thermal Expansion at 1000°C	16.9 µm/m·k
Young Modulus at 1000°C	140GPa
Shear Modulus at 1000°C	51GPa
Poisson Ratio at 1000°C	0.363

*Age-Hardened at 1010°C/2 h/air-cool + 788°C/2 h/air-cool

Source – Alloy digest Haynes 282 (2006). Reprinted with permission from Haynes International, Inc (19th December, 2014).

Hence, to produce the optimum combination of features in Haynes 282, the Al and Ti levels in the alloy were prudently selected. Small alloying additions such as C and boron (B) are necessary to provide improvement in mechanical properties [3].

Normally, after fabrication, Haynes 282 is subjected to a solution annealing temperature in the range of 2050˚F to 2100˚F (1121˚C to 1149˚C) [3]. The solution annealing temperature is beyond the solvus of $M_{23}C_6$. To obtain optimum properties, a rapid cool is preferable. If cooling is done at an appropriate rate, little, if any, the ɣ′ phase will be present in 282 alloy after solution annealing and the material will be ductile. Upon completion of solution annealing, Haynes 282 is subjected to precipitation heat treatment which consists of a two-step heat treatment of 1850˚F (1010˚C)/2 h/air-cool + 1450˚F (788˚C)/8 h/air-cool. In comparison to the solution annealed condition, in the precipitation heat treatment condition Haynes 282 experiences both secondary intragranular and grain boundary precipitation. The first step of the precipitation heat treatment is above the ɣ′ solvus temperature of 1827˚F (997˚C) and, therefore, does not lead to strengthening of the alloy. The aim of the first step of the heat treatment is believed to be the formation of Cr rich $M_{23}C_6$ carbides at the grain boundaries in the most suitable morphology for optimum mechanical properties. The ɣ′ phase is formed from the second step of the heat treatment [3].

The equilibrium fraction of the ɣ′ phase has a major influence on both mechanical properties and fabricability [3]. High levels of ɣ′ are required for high strength, both creep and tensile. On the other hand, low ɣ′ levels are needed for enhanced fabricability. Consequently, the amount of the ɣ′ phase in the 282 alloy was carefully balanced. The most influential constituents that determine the amount ɣ′ phase in the alloy is the amount of Al and Ti. The intermediate level of equilibrium ɣ′ allows the Haynes 282 alloy to have exceptional fabricability while also possessing excellent strength [3].

2.4 Fatigue of Materials

Fatigue of materials and structural components refers to the deformation and fracture due to cyclic, repeatedly applied stresses or strains [6]. Fatigue accounts for at least 90 percent of all service failures due to mechanical causes [26]. Fatigue failure typically occurs under the influence of cyclic loads in which the peak values are considerably smaller than the 'safe' loads estimated from the static testing data. The nature of fatigue behaviour is often divided into two categories, namely LCF and high cycle fatigue (HCF) [27]. The partition of these two categories can be seen in Figure 2.2.

LCF is representative of situations where a small number of cycles are required to cause failure, typically less than 10^5 cycles [27]. Usually, LCF conditions have high amplitudes. A distinguishing feature of LCF is that the peak stresses are above the yield strength [6]; therefore, it normally involves a considerable amount of plasticity at a macroscopic level [27]. Hence, it is often characterized in terms of strain. Take off and landing of aeroplanes are common examples of LCF conditions [28]. On the other hand, HCF describes cases where the number of cycles is typically greater than 10^6 [27]. This is characterized by small scale yielding due to lower stress levels [27], hence, the strains are confined to the elastic region [6]. Consequently, it is often characterised in terms of stress [27]. HCF can arise from resonant vibratory stress cycles at frequencies which can reach thousands of cycles per second [29]. Additionally, HCF damage can result from intake of debris into the engine; this is termed as foreign-object damage (FOD). Furthermore, HCF cracks can also initiate from the frictional contact between blade dovetail and disk under fretting fatigue conditions [29].

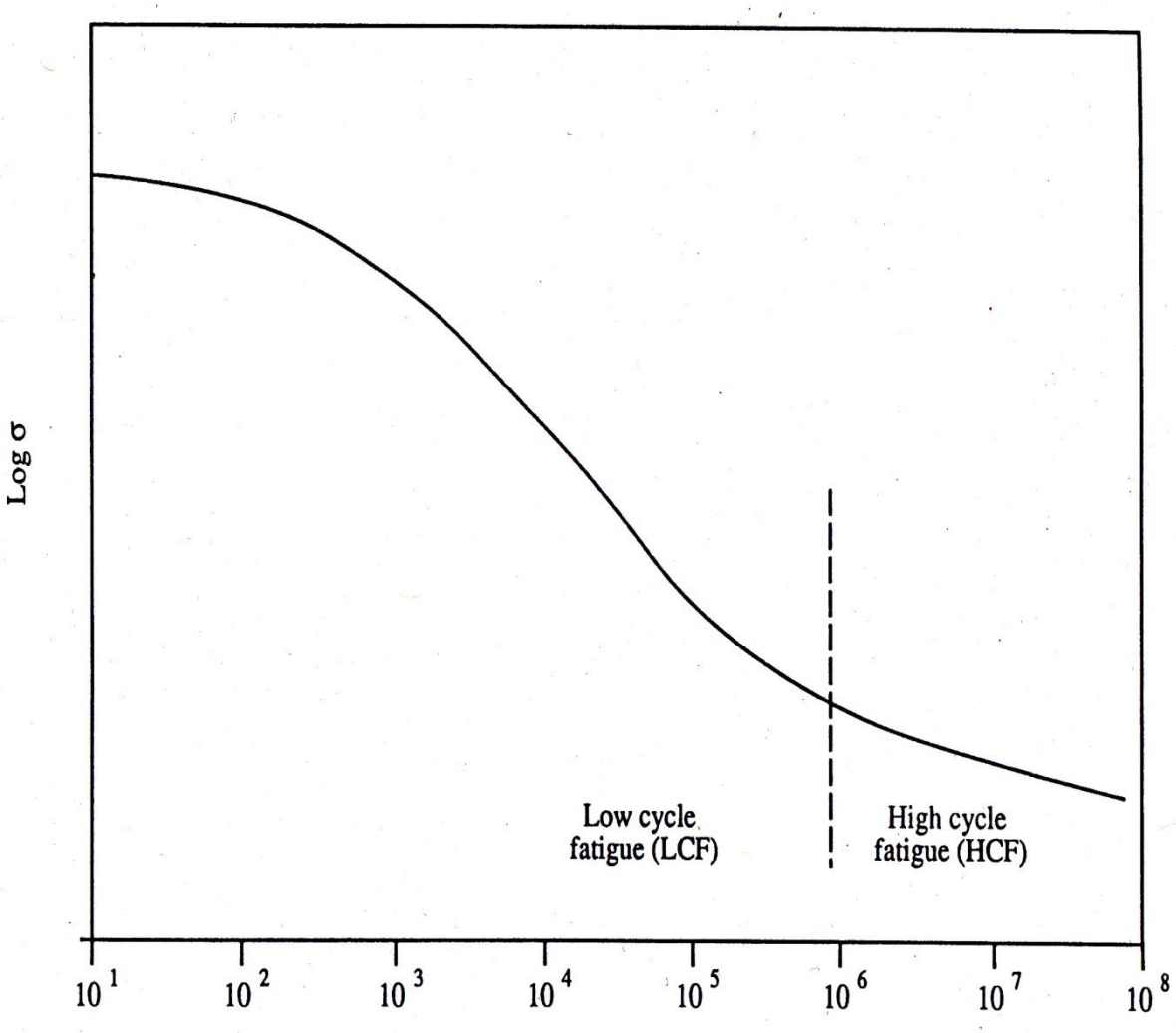

Figure 2.2 Typical S-N diagram showing transition from LCF to HCF [27].

Source – In-Situ short crack characterization of a nickel-based superalloy at ambient and elevated temperatures, Ph.D. Thesis by Robert Stephens (1991). Reprinted with permission from author (17th December, 2014).

Fatigue life can be divided into crack initiation and propagation phases [6]. Correspondingly, there are two fundamentally different experimental approaches to the study of the fatigue life of a component: the total fatigue life approach and the flaw tolerant (damage tolerant) approach [29]. The total fatigue life approach is based on smooth specimens [6], an example of which is the typical smooth hourglass shaped LCF specimens. It mainly focuses on the resistance to fatigue crack initiation and early crack growth. The plastic strains are responsible for the LCF damage as established independently by Coffin [30] and Manson [31]. They proposed an empirical relationship between the number of load reversals to fatigue failures and the plastic strain amplitude. This so-called Coffin-Manson relationship is the most widely used total-fatigue life approach to LCF [6]. On the other hand, the flaw tolerant approach to fatigue mainly focuses on the resistance to FCG [6]. This approach is closely related to the development of fracture mechanics. The fundamental premise here is that engineering components are not free of flaws, but with pre-existing cracks that can propagate during service. The growth of cracks is often a significant part of the fatigue life of structures. Non-destructive techniques (such as visual, dye-penetrant, X-ray techniques, ultrasonic, magnetic, or acoustic-emission methods) are usually employed in the determination of the initial crack size.

Fracture mechanics analysis is used to calculate the final critical crack sizes at which the catastrophic failure is anticipated. The useful life is then defined as the number of fatigue cycles required to propagate the crack from its initial size to the final size. The flaw-tolerant approach is widely utilized in aerospace and nuclear industries where catastrophic failures could result in the loss of human lives [6]. The economic advantages of the damage tolerance approach have been the driving force for much of the FCG data generated for nickel-based alloys and the development of turbine disc alloys with improved crack propagation resistance [32].

To predict the fatigue life of a component using the flaw-tolerant approach, it is necessary to know the rate at which flaws grow [6]. The crack growth rate data are generated through testing in the laboratory. A sharp crack is initiated in the specimen prior to testing. Obtaining separate and complete information on the two fatigue phases (crack initiation and propagation) is not feasible. Smooth specimen fatigue tests, to some extent, measure some portion of the crack propagation phase. Therefore, it is difficult to obtain information about the initial phase of crack growth in tests of precracked specimens. Hence, obtaining a complete picture of the fatigue performance of a material requires both total fatigue life and flaw-tolerant fracture mechanics approaches [6].

2.4.1 Design Concepts

Over the years, the design philosophies for fatigue have changed from the original safe-life approach to a fail-safe design philosophy and later to incorporating a damage-tolerant design philosophy [27]. The safe-life design approach involves designing for either a finite or infinite life during which time there is no significant fatigue damage [27]. This suggests that structural inspection ideally will not reveal any information on the current damage state of the component. The fail-safe design approach takes into account the fact that fatigue cracks may occur, hence, the structure is designed so that cracks will not lead to failure of the structure prior to being detected by routine inspection [27]. The damage-tolerant design approach assumes the existence of cracks in structures and components at the very first fatigue cycle [27]. It requires the identification and understanding of all critical areas in a component, which must be evaluated as potential sites for failure [27].

During the late 1960s, LCF was seen as the main mode of damage for rotating components such as discs and spacers of gas turbine engines [33]. By 1975, LCF performance had become the failure criteria for over 75 percent of the main rotating components of advanced military engines such as the F100 [34]. Engine manufacturers, with the aim of preventing disastrous failures, began to forecast disc and spacer design lives on the basis of LCF crack initiation behaviour [33]. The underlying principle of this design philosophy is that a set of components is retired after a specified cyclic life which is based on the number of cycles required to initiate an LCF crack in 1 out of 1000 components. The main drawback of this approach is that 999 components are discarded in a crack free condition. Furthermore, this design philosophy does not account for the number of cycles needed to propagate a crack to a subcritical length. Since the propagation of a crack could make up a significant fraction of a component's life, an alternative design approach known as retirement-for-cause (RFC), which permits a component to remain in service until a crack is detected, is more preferable [33]. RFC falls under the category of the flaw-tolerant (damage-tolerant) approach.

2.4.2 Low Cycle Fatigue:

The stress-strain response curve in a fatigue cycle is known as the hysteresis loop [6]. The hysteresis loop schematically shown in Figure 2.3 illustrates the important parameters associated with LCF testing. In a total strain range-controlled fatigue test, the cycling always occurs between the same total strain limits. If the stress necessary to attain a given total strain increases with each cycle, then the material is said to show cyclic-strain hardening. An example is shown in Figure 2.4(a). On the other hand, if the stress necessary to attain a given total strain decreases with each

Image removed due to copyright restrictions.

Figure 2.3 Schematic of a hysteresis loop showing the important parameters in LCF testing [6].

Source – High-temperature low cycle fatigue and crack growth behaviours of three superalloys: Hastelloy X, Haynes 230, and Haynes 188, Ph.D. Thesis by Yulin Lu (2005), Page Number 13, The University of Tennessee.

Image removed due to copyright restrictions.

Figure 2.4 Stress-strain behaviour for materials exhibiting cyclic-strain (a) hardening and (b) softening [6].

Source – High-temperature low cycle fatigue and crack growth behaviours of three superalloys: Hastelloy X, Haynes 230, and Haynes 188, Ph.D. Thesis by Yulin Lu (2005), Page Number 13, The University of Tennessee.

cycle, then the material is said to show cyclic-strain softening. An example is shown in Figure 2.4(b). Consequently, during fatigue testing, changes occur in both the plastic-strain range ($\Delta\varepsilon_p$) and elastic-strain range ($\Delta\varepsilon_e$). Cyclic strain hardening and softening usually occur at the beginning of the fatigue life (within 10% to 20% of the total fatigue life). Afterwards, the hysteresis loops become coincident to define a stabilized or saturated cyclic stress-strain behaviour. Another stable hysteresis loop will be formed if the total strain changes and the cycling is continued. A change in the total strain will result in a new stable hysteresis loop, and so on. The curve that connects the tips of the stable hysteresis loops is termed the cyclic stress-strain curve, which is an important representation of LCF data [6]. Figure 2.5 [35] shows a schematic example of a cyclic stress-strain curve. The cyclic stress-strain curve is usually be represented by a power-law relationship [6],

$$\Delta\sigma/2 = K'(\Delta\varepsilon_p/2)^{n'} \quad \text{.....(2.6)}$$

where $\Delta\sigma/2$ is the stress amplitude and $\Delta\varepsilon_p/2$ is the plastic strain amplitude of the stable hysteresis loop, n' is the cyclic strain-hardening exponent, and K' the cyclic strength coefficient.

The plastic strain range became an important parameter in the LCF life presentation following the introduction of the Coffin-Manson Law [30, 31] in the early 1950s. Typically the plastic strain amplitude ($\Delta\varepsilon_p/2$) is plotted against the number of reversals to failure ($2N_f$) on log-log coordinates [6]. A straight line usually results (Coffin-Manson Law), as shown in Figure 2.6. This straight line is described by equation (2.7):

$$\Delta\varepsilon_p/2 = \varepsilon_f'(2N_f)^c \quad \text{.....(2.7)}$$

where ε_f' is the fatigue ductility coefficient, defined by the strain intercept at $2N_f = 1$, and c is the fatigue ductility exponent. The fatigue ductility coefficient of a material is a measure of its cyclic

Image removed due to copyright restrictions.

Figure 2.5 Schematic of a cyclic stress-strain curve established with stable or half-life hysteresis loops. Circles represent the tips of stable loops for a particular total strain range [35].

Source – High-temperature low cycle fatigue and crack growth behaviours of three superalloys: Hastelloy X, Haynes 230, and Haynes 188, Ph.D. Thesis by Yulin Lu (2005), Page Number 16, The University of Tennessee.

Image removed due to copyright restrictions.

Figure 2.6 Schematic representation of the LCF life showing the total strain amplitude, plastic strain amplitude, and elastic strain amplitude [6].

Source – High-temperature low cycle fatigue and crack growth behaviours of three superalloys: Hastelloy X, Haynes 230, and Haynes 188, Ph.D. Thesis by Yulin Lu (2005), Page Number 18, The University of Tennessee.

ductility [36]. A smaller value of *c* means a higher value of the fatigue life. It has been shown that $c = -1/(1 + 5n')$ [37]. Thus, materials with larger values of n' have longer LCF lives [6]. Similarly, a relationship exists for the elastic strain and fatigue life [38], mainly used in HCF data representation [6],

$$\Delta\varepsilon_e/2 = \sigma_a/E = \sigma_f' (2N_f)^b \quad \text{.....(2.8)}$$

where $\Delta\varepsilon_e/2$ is the elastic strain amplitude, σ_a is the alternating stress amplitude, *E* the Young's modulus, σ_f' is the fatigue-strength coefficient defined by the stress intercept at $2N_f = 1$, and *b* the fatigue-strength exponent. A smaller value of *b* denotes a longer life. It has been shown that $b = -n'/(1 + 5n')$ [37]. Thus, lower values of n' result in longer HCF lives.

2.4.3 Fatigue Crack Growth

The fatigue failure of a component begins with the initiation of a crack from a flaw or stress raiser, which then propagates until a critical length is reached at which point failure of the component occurs [6]. The rate at which a crack propagates depends on the stress, microstructure and environment ahead of the crack tip.

FCG is driven by external forces while the microstructure of the material serves as the resistive force [28]. Hence, crack advance is restrained by either reducing the driving force or toughening the material [39]. Toughening may be either intrinsic or extrinsic. Intrinsic toughening is achieved by increasing the inherent resistance of the material to cracking, for instance, by increasing the ductility of the microstructure. Extrinsic toughening is achieved by invoking external mechanisms which, through microstructural manipulation, reduce the effective external force [28].

The FCG path is categorized by the type of loading [40]. In general, fracture can occur by one of three modes (types) of loading (or a combination of these modes in the case of mixed-mode fracture) [29]. These three modes are identified as Modes I, II, and III. Mode I is the tensile opening mode in which the crack faces are displaced in a direction normal to the crack plane. Mode II corresponds to the crack faces that slide in a direction normal to the crack front and is also referred to as the in-plane sliding mode. Mode III corresponds to the crack faces that shear parallel to the crack front direction and is also referred to as the anti-plane shear mode [29].

Specifically, Mode 1 is categorized as planar crack growth and often includes fatigue striations [40]. Mode II, on the other hand, is referred to as crystallographic FCG. In Mode I, crack growth consists of simultaneous or alternating flow along two slip systems on a minute scale, thus leading to a macroscopically planar crack path that is perpendicular to the loading axis. Striations are formed as the crack opens and blunts during the fatigue cycling process. Upon closure, the compressive forces are not sufficiently high to plastically deform the crack tip back to the original formation; hence, the crack advances a distance. The striations are seen as parallel ridges perpendicular to the direction of the FCG, with the spaces between striations directly related to the distance that the crack travelled during that cycle. However, not all fatigued samples will show striations, since striation development is strongly influenced by the value of ΔK, stress state, environment, and composition of alloy. In Mode II, the crack extends by single shear in the direction of the primary slip system. With a loading axis of <001> in the FCC materials, the single shear happens on the {111} planes, which results in a macroscopically zigzag crack path [40].

As mentioned earlier, flaws may be present in many structural components before services. The useful fatigue life is then the time or the number of cycles to grow a dominant flaw of the initial size to a critical dimension, at which catastrophic failure is expected [6]. To predict the fatigue

lives of these components for design and maintenance purposes, it is necessary to know the rates at which flaws/cracks grow [6].

The crack-growth rate data are generated through testing in laboratory. A specimen of a special geometry is designed, and a sharpened crack is initiated. The crack length is monitored and recorded as a function of the number of load cycles or elapsed time [6]. Various crack-length monitoring techniques are employed. Examples include the use of a calibrated travelling microscope, eddy-current techniques, electropotential measurements, compliance measurements, acoustic-emission detectors, etc. The crack growth rate is expressed in terms of the crack length increment per cycle or unit time, *da/dN* or *da/dt*, respectively. Figure 2.7 shows a typical FCG curve under a constant load range. As the number of loading cycles is increased, the crack length increases. By using graphical procedures or through computation, the FCG rate can be determined from such a curve. From these methods, the crack growth rates that result from a given cyclic load are $(da/dN)a_i$ and $(da/dN)a_j$ when the crack is of lengths, a_i and a_j, respectively [6].

One of the critical tasks in the flaw tolerant approach to predict the fatigue life is to relate the crack growth rate data to a loading parameter [6]. Under conditions of small scale yielding, the stress intensity factor (K) can uniquely characterize the stress environment near the crack tip [29]. When yielding in front of the crack becomes extensive, the crack needs to be characterized by using elastic plastic fracture mechanics (EPFM). Two of the popular EPFM parameters are the J-integral and crack tip opening displacement (CTOD). The J-integral is a fracture mechanics parameter that was proposed by Rice [41] as a method of characterizing the stress-strain field at the tip of a crack. It involves the use of the mathematical integration of a path selected far enough from the crack tip to be elastically analyzed, and then substituted for an inelastic region close to the crack-tip region.

Image removed due to copyright restrictions.

Figure 2.7 Typical FCG curves under a constant load range [6].

Source – High-temperature low cycle fatigue and crack growth behaviours of three superalloys: Hastelloy X, Haynes 230, and Haynes 188, Ph.D. Thesis by Yulin Lu (2005), Page Number 20, The University of Tennessee.

The CTOD, on the other hand, can be understood in the following manner: the yielding of the material leads to a rearrangement of stresses at the crack tip. This rearrangement can be treated by an effective crack length which is longer than the actual crack length. The physical reasoning that supports this is that both plasticity and an increased crack length increase the compliance of the material. The tip of the effective crack would lie inside the plastic zone of the actual crack. The effective crack, therefore, can be imagined to have a finite opening at the tip of the actual crack. This opening is defined as the CTOD [29].

2.4.3.1 Linear Elastic Fracture Mechanics

Paris [36] established that the rate of fatigue crack propagation per cycle, da/dN, is a single valued function and can be defined through linear elastic fracture mechanics (LEFMs). This function, ΔK, is called the "stress intensity range" and defined as:

$$\Delta K = K_{max} - K_{min} \quad \text{.....(2.9)}$$

where K_{max} is the maximum stress intensity and K_{min} is the minimum stress intensity in each cycle. The alternating stress intensity ratio, *R*, is defined as:

$$R = K_{min}/K_{max} \quad \text{.....(2.10)}$$

The stress intensity, *K*, defines the magnitude of the stress field at the crack tip, hence, it is a function of the nominal applied stress, the crack length and the crack-tip geometry. *K* can be given as:

$$K = f(\sigma, a, \text{geometry}) \quad \text{.....(2.11)}$$

where σ is the nominal external stress and *a* is the crack length. The functionality that relates σ, *a*, and geometry to *K* depends on the configuration of the cracked component, as well as manner and position in which the loads are applied. These functions have been determined for many common specimen configurations, and various work [42] have described procedures for the determination of these functions for non-standard configurations.

It is usually desirable to estimate the useful component life for the purposes of design and failure analyses. The number of fatigue cycles to failure can be determined by using the Paris-power law, equation (2.12):

$$\frac{da}{dN} = C\Delta K^m \quad \text{.....(2.12)}$$

For instance, if the following assumptions are made: *initial flaw size to be* a_0 , *final crack size,* a_f, *Y remains constant as the crack grows,* and $\Delta K = Y\Delta\sigma\sqrt{a}$. Then, the number of fatigue cycles to failure can be determined by integrating equation (2.12)

$$\mathrm{CY^m(\Delta\sigma)^m} \int_0^{N_f} dN = \int_{a_0}^{a_f} \frac{da}{a^{m/2}} \quad \text{.....(2.13)}$$

Thus, the fatigue life is given by

$$\mathrm{N_f} = \frac{2}{(m-2)CY^m(\Delta\sigma)^m} \left[\frac{1}{(a_0)^{\frac{m-2}{2}}} - \frac{1}{(a_f)^{\frac{m-2}{2}}} \right] \quad \text{.....(2.14)}$$

for $m \neq 2$

$$\mathrm{N_f} = \frac{1}{CY^2(\Delta\sigma)^2} \ln\frac{a_f}{a_o} \quad \text{.....(2.15)}$$

for $m = 2$. The assumption that Y remains constant is generally not valid. Hence, the integration is usually numerically done. It can be observed from equation (2.14) that when $a_0 << a_f$ (which is usually true for ductile alloys), the fatigue life, N_f, is not sensitive to the final crack length, a_f, but strongly dependent on the choice of a_0 [6].

The majority of experimental data show a good agreement with the Paris-power law relationship, equation (2.12), given that there is a proper selection of the constants C and m [6]. However, this observation is valid only within a particular range of crack growth rates. At the extreme values of ΔK, both above and below those of the Paris regime, the Paris-power law does not hold. The whole log (da/dN) versus log (ΔK) curve, which is typically used to represent FCG rate data, assumes a sigmoidal shape thus defining three distinct regimes as shown in Figure 2.8. In Regime I, there exists a threshold stress intensity factor range, ΔK_{th}, such that at $\Delta K < \Delta K_{th}$, the crack practically does not grow. Above the threshold, there is a steep increase in da/dN with increasing ΔK. The Paris-power law applies in Regime II. In Regime III, the K_{max}, value approaches that of the fracture toughness, K_c. The crack growth rates rapidly increase, thus leading to catastrophic failures [6].

2.5 Irreversibility of Cyclic Slip

Fatigue cracks can grow even when the maximum value of stress intensity that corresponds to the threshold value ($K_{max,o}$) in the loading cycle is a small fraction of the corresponding value of fracture toughness K_{IC} for monotonic loads [29]. The concept of irreversibility of cyclic slip is central to why fatigue cracks are much more effective in causing failure. An analogy to irreversibility of cyclic slip is a frog on a slippery pole: the frog can jump and climb, for instance, 10 cm and slip back, perhaps 8 cm. The frog has a net jump of 2 cm in every cycle and gradually

Image removed due to copyright restrictions.

Figure 2.8 Typical FCG diagram showing three different regimes [6].

Source – High-temperature low cycle fatigue and crack growth behaviours of three superalloys: Hastelloy X, Haynes 230, and Haynes 188, Ph.D. Thesis by Yulin Lu (2005), Page Number 24, The University of Tennessee.

the frog can reach the top of the pole, something that it could not have achieved with a single jump. The net jump of 2 cm is the irreversibility of the cyclic slip for the frog [29].

In materials, the irreversibility of cyclic slip occurs due to the irreversibility of forward and reverse motions of dislocations in the glide plane [29]. Irreversibility of slip can occur due to one or more of the following mechanisms [29]:

1) cross slip of screw dislocations that lead to different paths for their forward and reverse glide. Thus, planar slip materials have less irreversibility,
2) climb of dislocations at higher temperatures will also facilitate irreversibility which lead to accumulation of damage,
3) interaction between dislocations can lead to formation of jogs or Lomer Cotrell locks which are irreversible. In other words, dislocation tangling during crack opening can impede the reversal of slip while the crack is closing,
4) irreversibility can also result from asymmetry in the tension and compression portion of the fatigue cycle due to back stress on the glide plane (Bauschinger effect), and
5) oxides formed at the crack surface can enhance slip irreversibility since high modulus oxides will tend to repel dislocations (by image forces), and hence prevent them from slipping out of the crack tip surface.

2.6 Crack Closure

Crack closure can influence the response of the material during FCG [40]. Closure can be caused by a variety of reasons including surface roughness, plastic wake effects, oxides or fretting debris [27]. Figure 2.9 shows these mechanisms of crack closure.

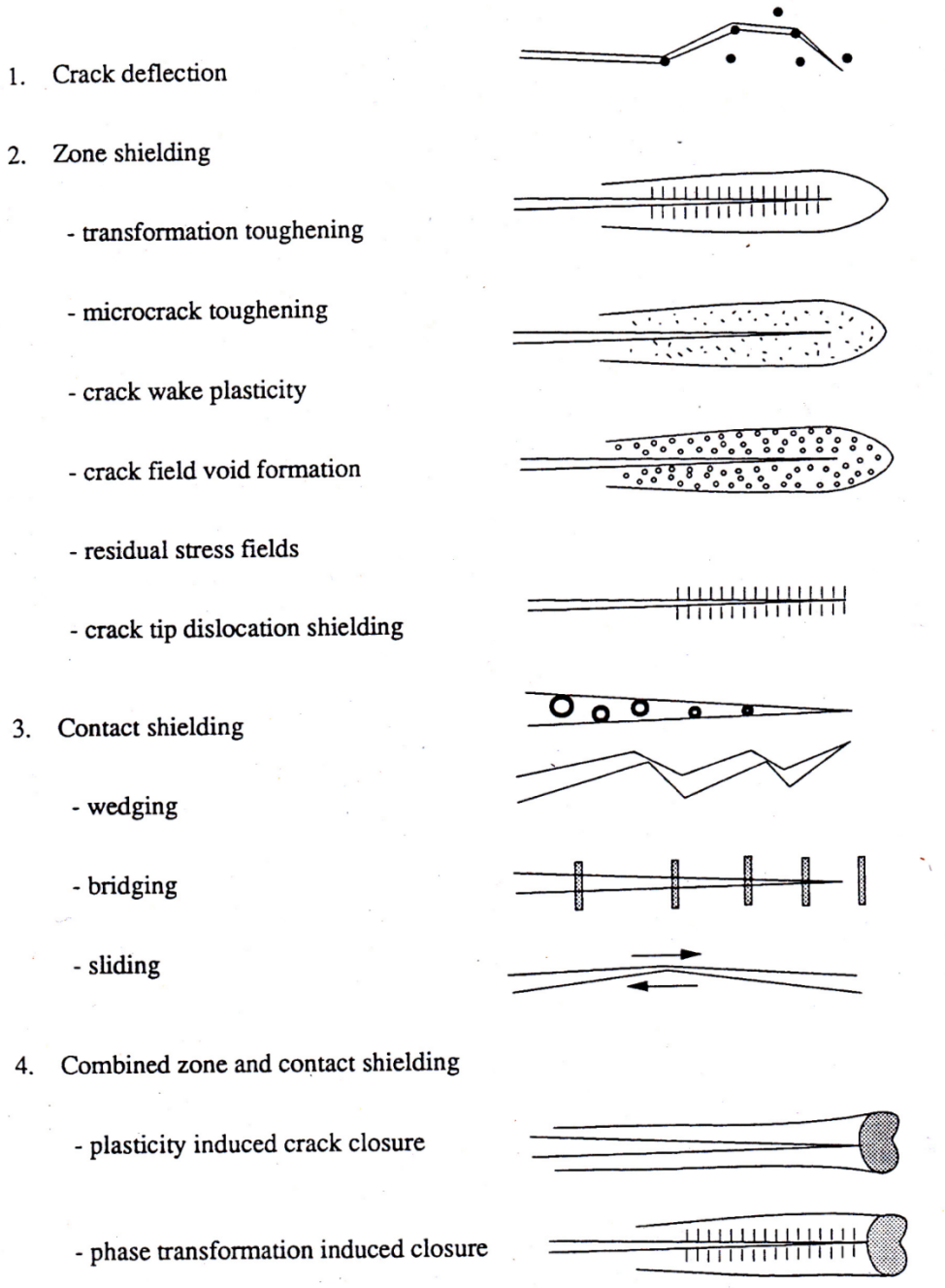

Figure 2.9 Micro-mechanisms of crack closure (crack tip shielding) [27].

Source – In-Situ short crack characterization of a nickel-based superalloy at ambient and elevated temperatures, Ph.D. Thesis by Robert Stephens (1991). Reprinted with permission from author (17th December, 2014).

Elber [43] observed that the correlation of crack growth rates with applied ΔK is complicated by the fact that the opposite faces of the crack, near the crack tip, do not separate at zero applied ΔK [44]. Rather, the crack tip area remains closed up to some level of ΔK_{cl} (stress intensity range at closure). In his original paper, Elber ascribed this closure to the wedging effect of the plastic zone at the surface of the specimen. Closure is thought to shield the crack tip such that the effective stress intensity, $K_{eff} = K_{max} - K_{cl}$, is less than that which is computed by using remotely applied loads. From Elber's perspective, closure is due to crack growth through the plastic zone wake which contains a residual compressive load, thus resulting in premature crack face contact. This phenomenon has since been referred to as plasticity-induced closure [45]. Another closure mechanism exists when the fracture surface is irregular and Mode II displacements are present. In this case, premature crack face contact occurs at some $\Delta K > 0$. This prevents the crack from completely closely, thereby reducing the magnitude of cyclic loading experienced at the crack tip. This mechanism is termed roughness induced closure [46]. Roughness induced closure is expected to only occur when the size of the surface asperities is comparable to the CTOD. This condition is present in near threshold tests or at low R-ratios [44]. Oxide induced crack closure is another form of closure that arises from aggressive environments which lead to the formation of an oxide layer of thickness comparable to the crack opening displacements [44].

Irrespective of the mechanism, closure results in a decrease in the driving force for crack growth [44]. Cyclic loading between an upper limit P_{max} (maximum load) and a minimum P_{min} (minimum load) produces a cyclic stress intensity range described by ΔK. It is the magnitude of ΔK, as well as the R-ratio, which dictate the rate of crack growth. If the crack is held closed or wedged open, the effective cyclic load transmitted to the crack tip is reduced, which results in a lower driving force for crack advance [44].

2.7 Effect of Load Ratio on Fatigue Crack Growth

Generally, as the load ratio increases, the rate of crack growth increases and the threshold value decreases up to $R<R_{cr}$ (where R is load ratio and R_{cr} is the critical load ratio) and remains constant thereafter [29]. Additionally, it is commonly observed that the increase in crack growth rates at higher load ratios is diminished in the Paris regime when compared to the threshold regime. The increase in crack growth rates with increase in load ratio has been explained by the fatigue crack closure concept. At $R>R_{cr}$, it is assumed that the K_{min} in the stress cycle is greater than K_{cl} and therefore no effect of load ratio is observed [29].

2.8 Effect of Frequency on Fatigue Crack Growth

Generally, it is accepted that the effect of frequency on FCG is non-existent at room temperature. However, for materials that have significant strain rate sensitivity, a variation in frequency could significantly affect the rate of crack propagation even at room temperature [47, 48]. This is because an increase in frequency can cause an acceleration of the rate of strain at the crack tip [49]. The increased strain rate involves the accumulation of higher density of dislocations, which upon interlocking with each other leads to an increase in the yield strength of the material. This results in the strengthening of the matrix near the crack and retards further propagation of the crack tip [49]. Hence, higher frequency loading means lower the cracking rate.

On the other hand, at high temperatures, the effect of frequency on the rate of fatigue crack propagation can be attributed to the mechanism of oxidation assisted FCG [50, 51]. It is suggested that at lower frequencies, there is a significant reduction in the velocity at which the fatigue crack

tip propagates. This creates a favourable condition for the ample diffusion of oxygen to the crack tip. Oxidation occurs, which leads to the embrittlement of the crack tip. The brittle nature of the crack tip favours more crack growth. Consequently, the fatigue crack propagation rate is increased. Thus, in essence, high testing frequencies would not provide favourable conditions for oxygen to diffuse to the crack tip in time to cause embrittlement since the crack is advancing at a relatively higher velocity. However, at lower testing frequencies, the crack is advancing at a relatively lower rate which favours the ample diffusion of oxygen to the crack tip. Therefore, more embrittlement of the crack tip occurs at the lower frequency and the crack advances more.

2.9 Effect of Microstructure on Fatigue Crack Growth

The influence of the microstructure on the FCG of superalloys can be discussed in terms of the effect of precipitate distribution and that of grain size [29].

2.9.1 Precipitate Distribution

Fine precipitates with low coherency strains can be readily sheared by dislocations which lead to the formation of relatively fewer number of intense slip bands caused by slip band softening [29]. Through transmission scanning microscopy (TEM) analysis, it has been observed that larger precipitates result in slip dispersal and hardening as a result of Orowan looping. Consequently, small coherent precipitates provide the best resistance to FCG due to an increase in the reversibility of cyclic slip. Antolovich and Jayaraman [52] performed a study on Waspaloy in which ɣ′ sizes of approximately 10 and 100 nm were produced at each of the three different grain sizes. It was observed that the effect of decreasing ɣ′ size on fatigue crack growth rates was more pronounced in the coarse grained material than in the fine grained material. The effect of ɣ′ size and distribution

decreased at higher temperatures, but even at 650˚C, it was shown that small precipitates and high volume fractions gave the best resistance to FCG where the crack path was transgranular, although ɣ′ size had no effect when the crack path became intergranular [53].

2.9.2 Grain Size

It has been shown that even at a constant ɣ′ size, the crack growth rates decrease and the fatigue threshold increases as the grain size is increased [52, 54, 55]. This has been ascribed to both intrinsic and extrinsic factors although the effect of the latter has been considered to be larger [29]. Intrinsically, larger grain sizes increase the inhomogeneity of deformation [44]. Inhomogeneous deformation, in which dislocation motion is restricted to well defined slip planes, gives rise to less dislocation interaction. Subsequently, the amount of slip reversibility is increased. Thus for large grains, reversible slip damage is more easily accommodated and the FCP rate is reduced [44]. The effect from extrinsic factors is related to crack closure. Larger grain sizes increase the fracture surface roughness, thus resulting in more roughness induced closure. The corresponding rougher surfaces results in a higher crack path tortuosity which means a longer effective crack path to obtain similar projected growth rates [29, 44]. Additionally, a higher crack path tortuosity results in an increase in crack deflection, thus leading to decreased ΔK_I components [56].

2.10 Effect of Temperature on Fatigue Crack Growth

At nominal temperatures, a decrease in temperature will lead to a decrease in ductility and hence, decrease overall fatigue life [40]. Fracture toughness decreases with decreasing temperature, and

therefore disastrous failure of a specimen can occur at a lower ΔK. The decreased plasticity also influences the rate of fatigue crack propagation, since decreasing the temperature will reduce the plastic zone size as long as the ductile mechanism for growth is still active. A reduction in plastic zone size will make it difficult for cracks to advance and hence, the threshold value will increase [40].

Characteristically, at room temperature, superalloys experience highly crystallographic faceted crack growth in the near threshold regime, when the size of the plastic zone is smaller than the grain size [29]. At low temperatures, the deformation in disk alloys is typically planar and slip heterogeneity seems to be particularly important in determining both their near-threshold behaviour and the appearance of the fracture surface [32]. The heterogeneity of deformation is affected by factors like precipitate size, misfit and distribution, grain size, Δ*K*, and temperature. In the Paris regime, fatigue striations have been observed in a number of superalloys, and the contributions from crack closure are reduced due to larger crack openings and a decrease in the roughness of the fracture surface. James and Mills [55] related the striation spacing in Inconel 718 to the square of the stress intensity factor range, thus suggesting that the crack growth rate in this regime is related to the cyclic crack opening displacement ΔCTOD. The actual effect of temperature on the fatigue crack propagation behaviour of nickel-base superalloys is understood by comparing the room temperature results with those at higher temperatures [29].

While effects at nominal temperatures are relatively straight forward, the effect of elevated temperatures on FCG is quite complicated [40]. At high temperatures, time-dependent processes, like creep and oxidation, will contribute to crack growth. Additionally, at elevated temperatures, several material properties such as elastic modulus and yield stress decrease. Furthermore, the heterogeneity associated with deformation decreases as a result of thermally activated processes

such as climb and cross slips that become active. This decrease in the heterogeneity of deformation changes the fracture surface from highly angular to flatter. The general trend for superalloys is one of falling thresholds with increasing temperature in the range of 20˚C to 650˚C [32]. This has been attributed to a variety of reasons, such as deformations that become homogeneous, decrease in roughness induced crack closure from flatter surfaces, and a decrease in the modulus and yield strength which increases the cyclic CTOD. There have been, however, within restricted ranges of temperature, observations of nearly constant threshold values (or even increase in the fatigue threshold) with temperature. In different studies, this has been attributed to dynamic strain ageing [57] and oxide induced crack closure [58] which results from oxide debris that wedge the crack open.

General observations over a wide range of temperatures (-270˚C to 850˚C) show that the growth rates in the Paris regime increase with temperature [55, 59]. In the absence of an aggressive environment, this increase in growth rate with temperature is again rationalized by decreasing modulus and yield strength, and an increase in the homogeneity of slip [29].

2.11 Welding Processes

Although the knowledge of metal joining processes had been in existence for thousands of years, forge welding performed by blacksmiths was the only welding process that was predominant [60]. However, at the close of the 19th century, when there was the capacity to produce a substantial amount of electrical current, a variety of completely new welding principles emerged. Amongst them are resistance, arc and gas welding [59].

A chronological description of the evolution of the welding processes is shown in Figure 2.10. Generally, welding can be categorised into three distinct groups. These are brazing, solid-state joining and fusion welding. In this work, the primary interest is in the area of the fusion welding process; hence, the fusion welding process will be expatiated on subsequently.

By definition, fusion welding can be described as a metal joining process in which, in the absence of pressure, a weld is created between materials that are in a molten state [61]. Fusion welding could be performed with or without a filler metal which melts at a temperature that is similar to that of the parent material. There are various types of welding processes that fall under the broad category of fusion welding; namely gas metal arc welding (GMAW), submerged arc welding (SAW), shielded metal arc welding (SMAW), gas tungsten arc welding(GTAW), resistance welding (RW), electron beam welding (EBW) and laser welding (LW). The versatility of the SMAW process gives it an advantage over other fusion welding processes. However, it has its drawbacks; namely: it is a manual process, there is the need to remove flux, and SMAW cannot be extensively used on thin sections. On the other hand, the GMAW process which employs the use of a consumable electrode, can be automated and inert-gas shielded. As a result, this welding process has the capacity to generate high production rates. RW can also be automated, however, there is the specific need for a lap-type joint and the pieces to be welded suffer a certain level of deformation. In contrast, GTAW can be performed either manually or automated with or without the use of a filler metal. This makes it highly versatile in comparison to the other welding processes [61].

EBW is a high energy density welding process which provides the capacity to make deep penetrations by using low heat input accompanied with little distortion.

Image removed due to copyright restrictions.

Figure 2.10 Chronological development of welding processes and their application [9].

Source – A Study on Laser Weldability Improvement of Newly Developed Haynes 282 Superalloy, Ph.D. Thesis by Lawrence Opeyemi Osoba (2012), Page Number 24, The University of Manitoba.

The major advantage of the EBW process is that welds which are free from contamination can be made by using this process. However, the drawback of this process is the restriction with regards to the size of the parts that can be welded due to the fact that the process is conducted by using a vacuum chamber [61].

Joining processes like welding are essential in the fabrication of gas turbine engine components since it is not practical to manufacture such components by exclusively using casting, forging or machining methods [61]. Fusion welding has been extensively used for fabricating nickel-based aero and land based turbine components [61], and high energy beam welding processes such as EBW and LBW particularly have the advantages of deeper weld penetration, higher welding speed, better weld quality with high solidification rates and low heat input [9]. Due to these advantages, materials that are welded through the use of these high energy beam welding processes have little distortion to the metallurgical and mechanical properties of the materials [9].

2.11.1 Laser Beam Welding

The acronym LASER stands for light amplification by stimulated emission of radiation [62], and LBW is a process that melts and joins metals by heating them with a laser beam. The laser beam can be produced by a solid state, gas or fiber laser. The beam provides a concentrated heat source which can be focused and directed by optical means to achieve high power densities, hence, allowing for narrow, deep welds and high welding rates [62].

2.11.1.1 Laser Beam Process

When a laser beam is irradiated on the surface of a material, the absorbed energy causes the heating, melting, and/or evaporation of the material depending on the absorbed laser power density [63]. In general, the laser welding process creates a pool of molten material (weld pool) at the overlapping workpiece surfaces. The laser welding process has two approaches [63]. In the first approach, sometimes referred to as conduction welding, the laser processing conditions are such that the surface of the weld pool remains unbroken. In this approach, the energy transfer into the depth of the material takes place by conduction (Figure 2.11(a)). The second and the most important approach, referred to as deep penetration welding, corresponds to laser processing conditions which create a "keyhole" in the weld pool. Generally, the transition from the conduction mode to deep penetration welding is associated with an increase in laser power intensity or irradiation time such that surface vaporization at the molten weld pool begins. The resulting evaporation-induced recoil pressure forms a small depression in the weld pool which subsequently develops into a keyhole by the upward displacement of molten material sideways along the keyhole walls (Figure 2.11(b)).

The subsequent ionization of the vapour leads to the formation of the plasma plume. The laser energy that enters the keyhole wall is determined by attenuation due to absorption of laser energy in the plasma plume [63]. Within the keyhole, laser energy is repeatedly reflected (multiple reflection) with efficient Fresnel absorption of energy at the keyhole walls. Thus, the keyhole plays an important role in transferring and distributing the laser energy deep into the material. The surface vaporization continues at the keyhole wall during laser welding to maintain the cavity. The vaporized materials act against the surface tension to keep the keyhole open.

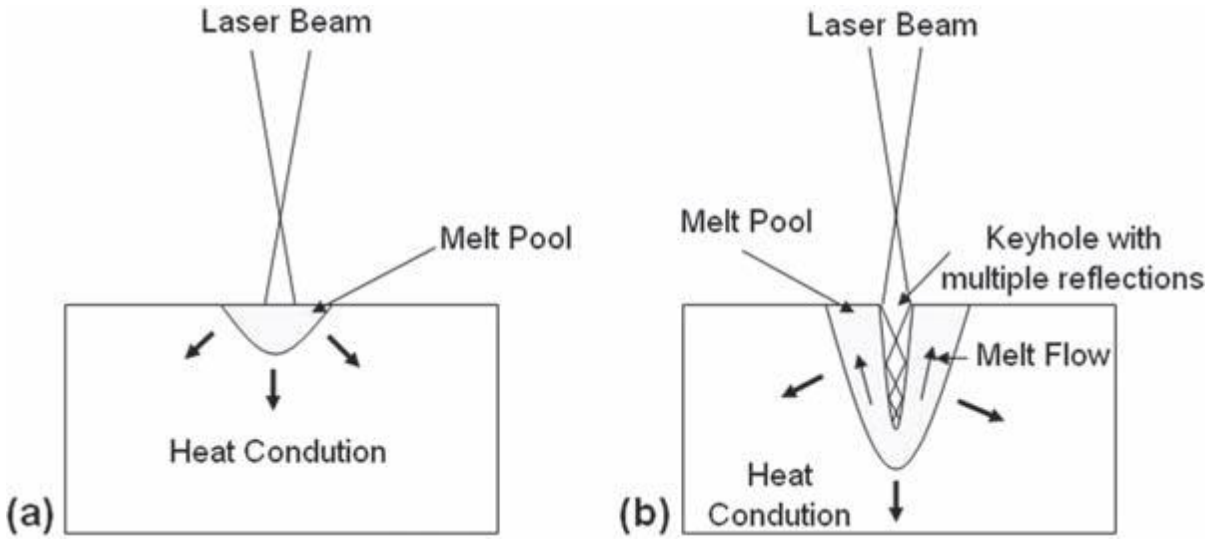

Figure 2.11 Schematic of the cross sections of (a) conduction and (b) deep penetration laser welding showing various effects [63].

Source – Laser Fabrication and Machining of Materials by B.N Dahotre and P.S. Harimkar (2008). Reprinted with permission from Springer Science + Business Media (12th December, 2014).

The melt accelerated upwards continuously flows out of the cavity. Figure 2.12 presents the schematic geometry of deep penetration laser welding. Various mechanisms of energy absorption during the laser welding process are presented in Figure 2.13. Under dynamic conditions, such as a moving laser beam, the welding speed is determined by the stability of the keyhole. Stable welding conditions correspond to the speed at which the keyhole speed achieves steady state.

The symmetry of the keyhole is also influenced by the welding speed. At low welding speed, the keyhole may be approximated by rotational symmetry, whereas at high welding speed, the keyhole profile significantly differs at the front and back walls [63].

2.12 Welding Metallurgy

Three distinct sections are formed when a material is welded; namely, the fusion zone (FZ), heat affected zone (HAZ), and the base metal which surrounds the HAZ [9]. If a filler is used in the welding process, this results in a FZ which has a combination of a composite and unmixed zone (Figure 2.14). Of the three regions formed during welding, the FZ is the region that attains a peak temperature that is significantly higher than the liquidus temperature. As a result, total melting and re-solidification of the base metal takes place in the FZ. When a filler is used during welding, a part of the base is dissolved by the weld pool. The rate at which the weld pool solidifies, as the heat source moves along the workpiece, ranges from 10-10^3 K/s for conventional welding to 10^3 – 10^6 K/s for high energy beam welding processes. A weldment to a certain degree, can be regarded as a continuous casting. On the other hand though, that description is not entirely accurate, since welds typically have a high rate of solidification which is significantly different from the near equilibrium cooling rate that take place during casting [9].

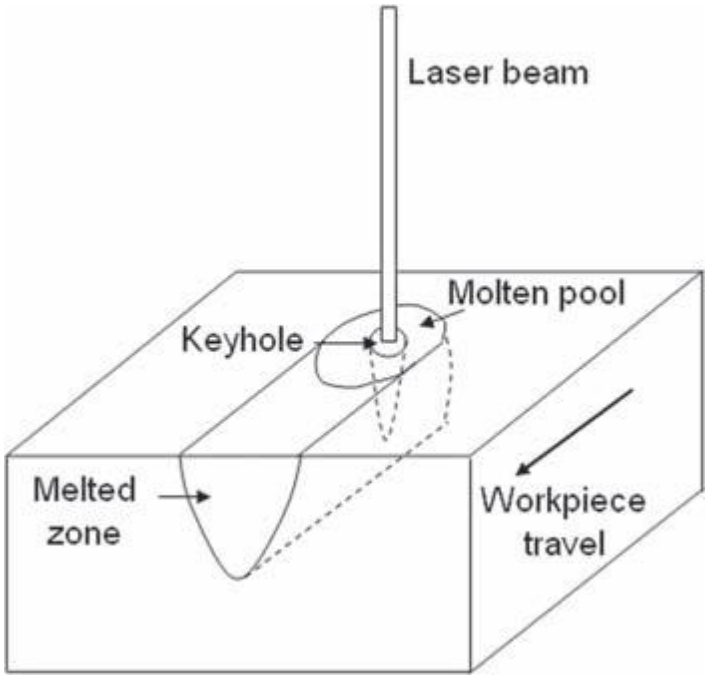

Figure 2.12 Schematic of the deep penetration welding process [63].

Source – Laser Fabrication and Machining of Materials by B.N Dahotre and P.S. Harimkar (2008).

Reprinted with permission from Springer Science + Business Media (12th December, 2014).

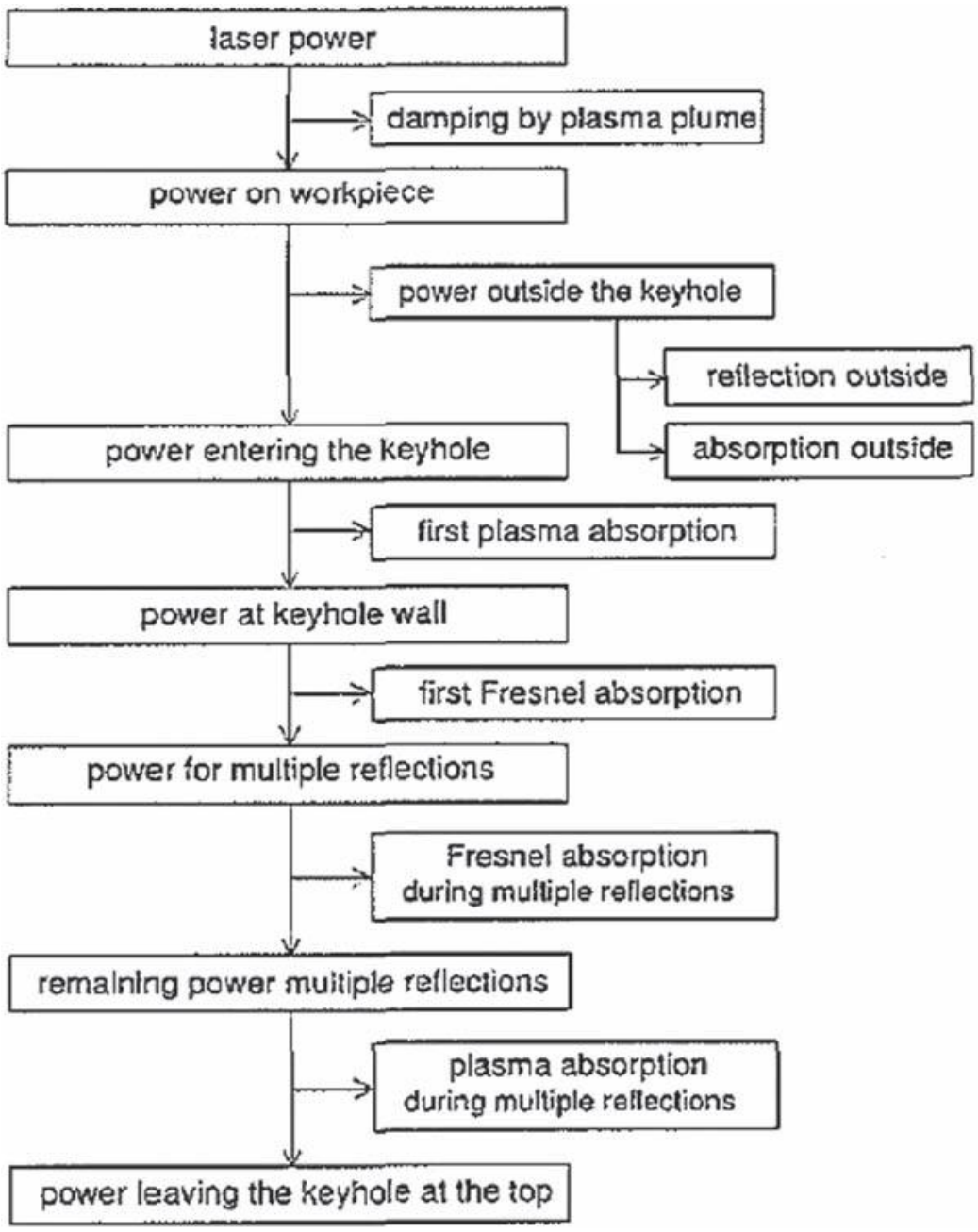

Figure 2.13 Flowchart of various absorption mechanisms during deep penetration laser welding [63].

Source – Laser Fabrication and Machining of Materials by B.N Dahotre and P.S. Harimkar (2008). Reprinted with permission from Springer Science + Business Media (12th December, 2014).

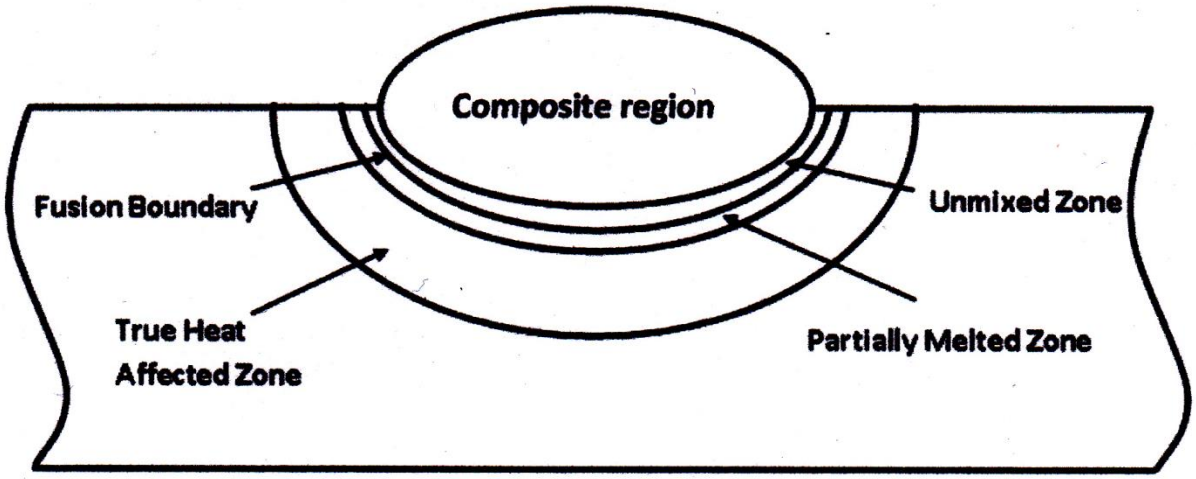

Figure 2.14 Different zones within a weld with filler.

In cases where welding is autogeneous, the base metal serves as a substrate where the nucleation and growth of solid phases in the FZ take place through a heterogeneous nucleation process. This phenomenon is known as epitaxial solidification. During the epitaxial solidification process, there is freezing of the solid embryo of the weld metal inside a mould formed in the base metal. Due to similarity in the composition of the molten and base metals, there is growth along a desired direction during the transfer of the heat of the fusion to the base metal. The various surface energy prevailing influences the contact angle β between the metal substrate and the solid phases that are formed. Mathematically, the relationship between β and the surface energies are as shown in equation (2.16):

$$\text{Cos}\,\beta = (\gamma_{ml} - \gamma_{sm}) / \gamma_{sl} \quad \text{.....(2.16)}$$

where γ_{ml}, γ_{sm}, and γ_{sl} are the interface energies for the metal/liquid, solid/metal and solid/liquid interfaces, respectively. Furthermore, Figure 2.15 diagramatically illustrates this relationship. It is not far from accurate to assume that $\gamma_{sm} = 0$ and $\gamma_{ml} = \gamma_{sl}$, since under autogenous welding conditions, the composition of the molten metal is similar to that of the parent metal and growth begins epitaxially as the heat of fusion is transferred to the base metal [61]. Hence, in essence, Cos $\beta = 1$ as $\beta = 0$ which leads to spontaneous solidification, in which undercooling of the melt is not necessary.

After the solidification process, any nucleus that remains grows, and as the nucleus grows, the conditions that exist in the surroundings that are very close to the solid/liquid interface have a significant effect on the nature of the FZ microstructure. Consequently, it is possible to generate a range of different weld microstructural morphologies. However, generally, microstructural morphologies can be grouped into three types; namely, cellular, planar and dendritic.

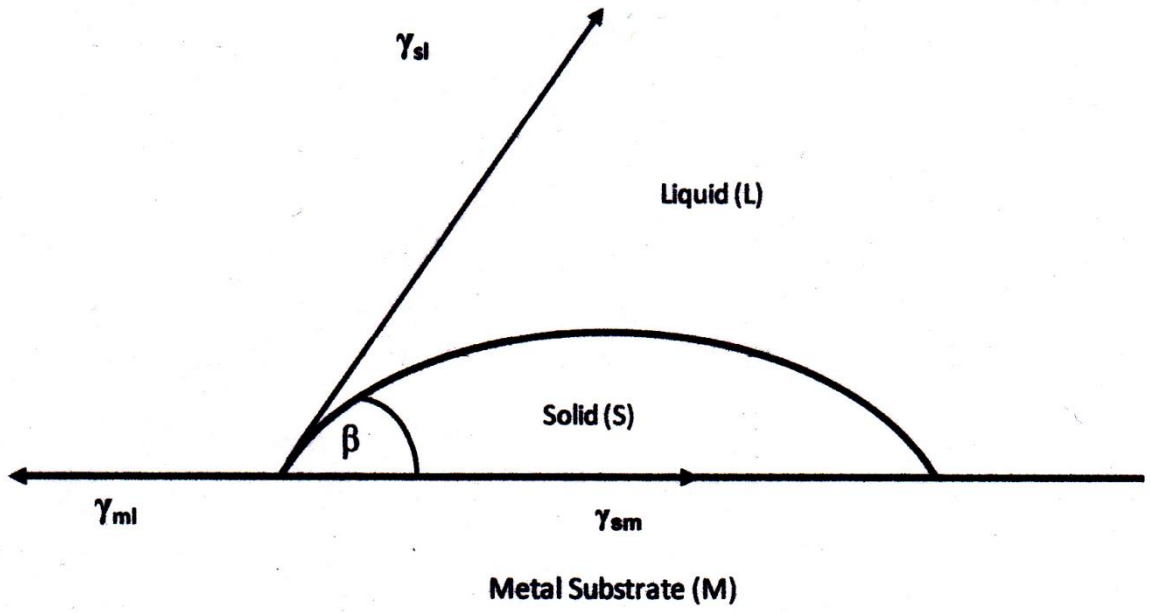

Figure 2.15 Surface forces present during heterogeneous nucleation of solid particle droplet on solid substrate.

In a planar solid/liquid interface, growth is regulated by the conditions that characterize the flow of heat and the path of the growth is at an angle of 90° to the solidification front, in essence, it is along the maximum thermal gradient (Figure 2.16(a)).

Characteristically, cellular growth is composed of numerous cells that relatively grow uniformly parallel to one another. In cellular growth, just as in the case of planar growth, the direction of the cell growth is determined by heat flow conditions (Figure 2.16(b)). On the other hand, unlike planar or cellular growth, dendritic growth is regulated by crystal growth. This is because the grains that have a preferred crystallographic axis which is closely aligned with the direction of heat flow are sustained. However, grains that are not favourably aligned are eliminated (Figure 2.16(c)).

Dendritic growth can be categorized into two main kinds; namely columnar and equiaxed. Columnar dendritic growth occurs when a packet of parallel dendrites which are along the same direction come together to create a well-formed substructure. However, equiaxed dendritic growth (Figure 2.16(d)) is characterized by the growth of dendrites, which do not have the same orientations, in a liquid that has been adequately cooled below the liquidus temperature. This is necessary to facilitate the occurrence of spontaneous nucleation. Every single dendrite in equiaxed dendritic growth is made up of separate grains in the final solidified structure, which are not necessarily parallel to each other.

It is possible to have a situation where both columnar and equiaxed grains form in the weld zone. However, the grains in the weld zone are either exclusively columnar or columnar close to the fusion line and may switch to an equiaxed structure near the centre depending on the temperature

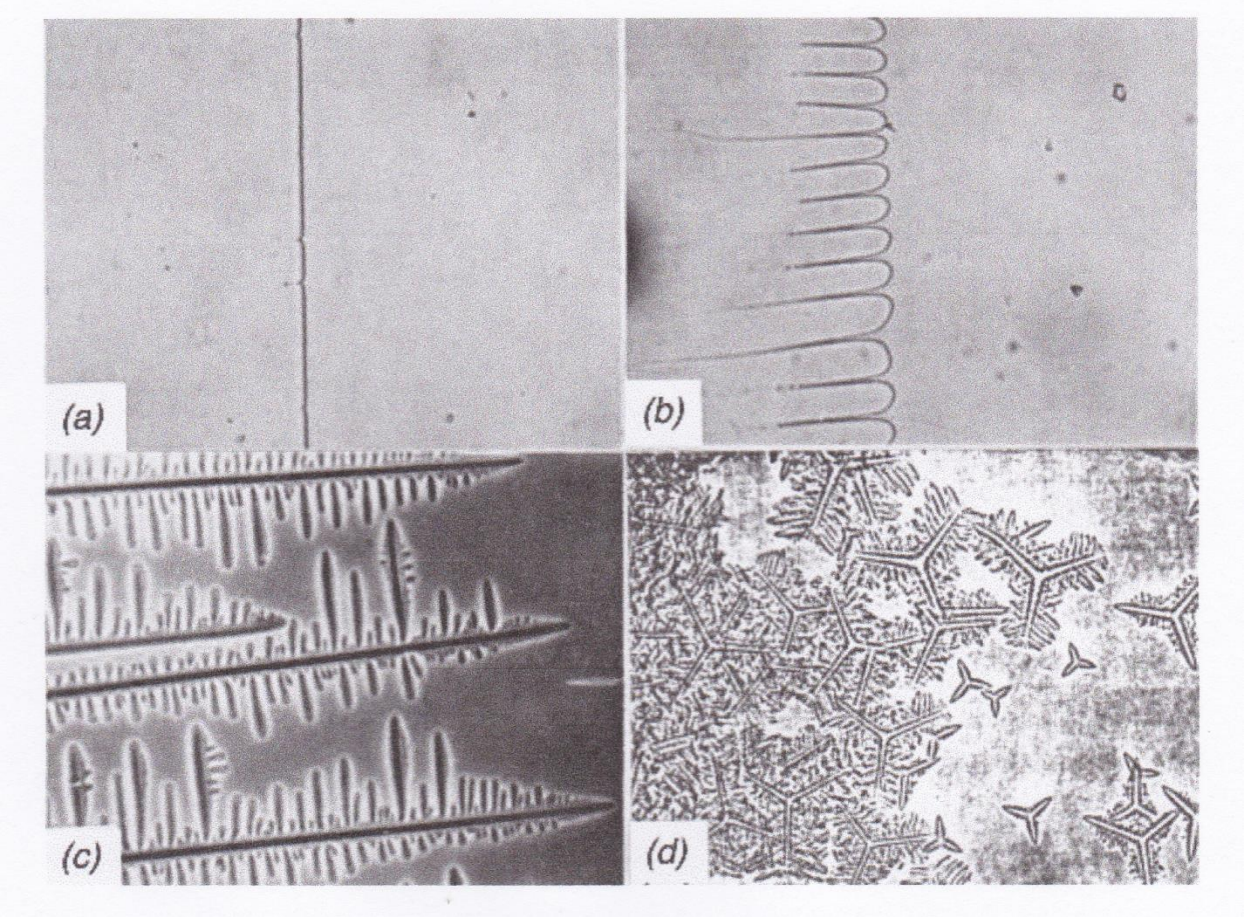

Figure 2.16 Basic fusion zone solidification mode: (a) planar, (b) cellular, (c) dendritic, (d) equiaxed dendritic [64].

Source – Welding Metallurgy, 2nd Edition by Sindo Kuo (2003). Reprinted with permission from Permissions Department, John Wiley & Sons, Inc (12th December, 2014).

gradient and growth rate or solidification rate. It is known that grains that are at angle of 90° to the centerline of the weld exhibit inferior tensile properties. On the other hand, equiaxed grains have the advantage of facilitating superior mechanical properties (ductility, fracture toughness, and tensile strength). Furthermore, equiaxed grains have better resistance to hot cracking [65].

The partially melted zone (PMZ) is the contiguous region that is immediately outside the portion of the weld metal where partial melting occurs during welding (Figure 2.14). The combination of the PMZ and the true HAZ (the region of the weld metal where exclusive solid state microstructural changes are experienced) makes up the totality of the HAZ area. In the HAZ region, the highest temperature characteristically attained falls between the liquidus and effective solidus of the base metal during welding. On the other hand, due to localized segregation, the effective solidus is constantly under the equilibrium solidus.

2.12.1 Elemental Solute Partioning during Welding

The weld microstructure and the weldability of superalloys in general, are significantly affected by the redistribution of solute or partitioning of alloying elements into a solid or liquid phase, relative to the nominal concentration during melt solidification. This phenomenon on a fine scale is classified as microsegregation. However, on a relatively larger scale, it is referred to as macrosegregation. Elemental solute enrichment during weld solidification is associated with hot cracking [66] because it widens the freezing temperature range, which causes solute segregation and non-planar solidification.

Various models have been used to explain solute partitioning and the resultant segregations that exist in solidified microstructures. However, these models are generally based on many assumptions [67-72], which include:

I. that the solidification rate is rapid enough that there is no change in solid composition once it is formed,
II. that diffusion in the liquid results in a compositional gradient adjacent to the solid-liquid interface,
III. that mechanical mixing is possible in the liquid but not in the boundary layer adjacent to the solidifying interface where the diffusion produced compositional gradient exists, and
IV. at the solid/liquid interface, the composition of the solidifying metal and the adjacent liquid are the equilibrium composition prescribed by the phase diagram.

To explain the phenomenon, Figure 2.17 is used to illustrate the solute segregation for an alloy of composition C_o. T_1 represents the temperature at which solidification starts, and its magnitude is just below the liquidus temperature (T_m), wherein a solid of composition $C_s = kC_o$ is formed. k is the equilibrium partition coefficient, defined as the ratio of the solid to liquid composition at the solid/liquid interface during solidification. When $k<1$, the solid (C_s) contains a concentration of the solute element that is smaller than that of the bulk liquid, and the excess solute is injected into the liquid, thus increasing the amount of solute in front of the solid/liquid interface.

When the liquid/solid interface is under equilibrium conditions, the extra solute is mixed throughout the liquid, which slightly raises the liquid solute content. When the alloy is further cooled from T_1 to T_2, equilibrium conditions at the interface dictate that the solid has a composition Cs_2, which injects more solute into the liquid and this will continue until the solid/liquid interface reaches T_3, where the solid formed has the composition C_o and the adjacent liquid has the

Image removed due to copyright restrictions.

Figure 2.17 Phase diagram showing the compositions of the solid and liquid at four temperatures [66].

Source – A Study on Laser Weldability Improvement of Newly Developed Haynes 282 Superalloy, Ph.D. Thesis by Lawrence Opeyemi Osoba (2012), Page Number 39, The University of Manitoba.

composition $C_{L3} = C_o/k$. At this point, a steady state is attained and the amount of solute injected is the amount required to raise the composition of the liquid at the solid/liquid interface to a composition C_o/k, thus maintaining the shape of the composition gradient in the liquid just next to the solid/liquid interface. For an isomorphous system, where only a single type of crystal structure exists over all the composition range, the final solid is the pure solute. However, for a eutectic system, the liquidus and solidus meet at the eutectic composition and the final solid is eutectic. Under non-equilibrium conditions, such as during rapid solidification which is common during welding processes, the solid and the liquid at the solid/liquid interface are not at equilibrium and the excess solute in the liquid is not completely mixed because of the limited diffusion that takes place, which invariably results in a compositional gradient that extends into the liquid from the solid/liquid interface. Various models exist that allow for non-equilibrium partition coefficient, 'k', and its variation with solidification velocity [73]. In these models, the partition coefficient is allowed to vary between the equilibrium value associated with the phase diagram at low growth velocities and a value of 1 at extremely high growth rates. When $k' = 1$, the solid that forms has the same composition as that of the liquid and this is termed as partitionless solidification. The occurrence of non-equilibrium partitioning leads to a situation where at high solidification rates, less solute redistribution occurs in a solidified structure which forms a more uniform composition. In this extreme case where less solute partitioning occurs, the appearance of normally occurring second phases may be avoided. These effects can be expected during rapid solidification of high energy density processes such as LBW and EBW.

Furthermore, rapid solidification may lead to the creation of a variety of non-equilibrium phases. However, these phases may exist in other compositions as equilibrium phases, with their range of stability simply extended. As a matter of fact, they may as well be new phases not usually observed

in the appropriate phase diagram of the alloy. Of more significance is the fact that high cooling rates may have an indirect effect on the phases that form in the welded microstructure, even if solidification behaviour is not significantly affected.

In some alloy systems, the as-solidified phases experience solid-state transformation during cooling because they are not stable at low temperatures. In the event that solid state cooling is fast enough, solid-state transformation may be restrained or changed in the case of diffusion controlled reactions. On the other hand, there can be a change in the nature of the transformation if there is insufficient time for diffusion to occur. Segregation during weld pool solidification can also lead to the occurrence of weld defects and/or variations in properties throughout the FZ.

2.12.2 Welding Defects

The term 'welding defects' encompasses a range of deleterious features that can result from welding a material. These include: discontinuities, flaws, interruptions and/or ruptures that could either be surface or internal features that become part of the welded material [64, 74]. These features can negatively influence the performance and integrity of weldments. The source for these unwanted features could be mishaps that are associated with the process, design or metallurgy. Some common imperfections that can form in weldments are illustrated in Figures 2-18a-e. Imperfections that are associated with process or procedure related problems include porosity, lack of fusion, undercut, shrinkage voids, crater cracking, slag inclusion and lack of penetration. On other hand, high-low conditions are an example of a design related defect that results from poor alignment of workpieces during welding or the use of workpieces that do not have the same thickness. With regards to imperfections that are metallurgically related, cracks and microfissuring

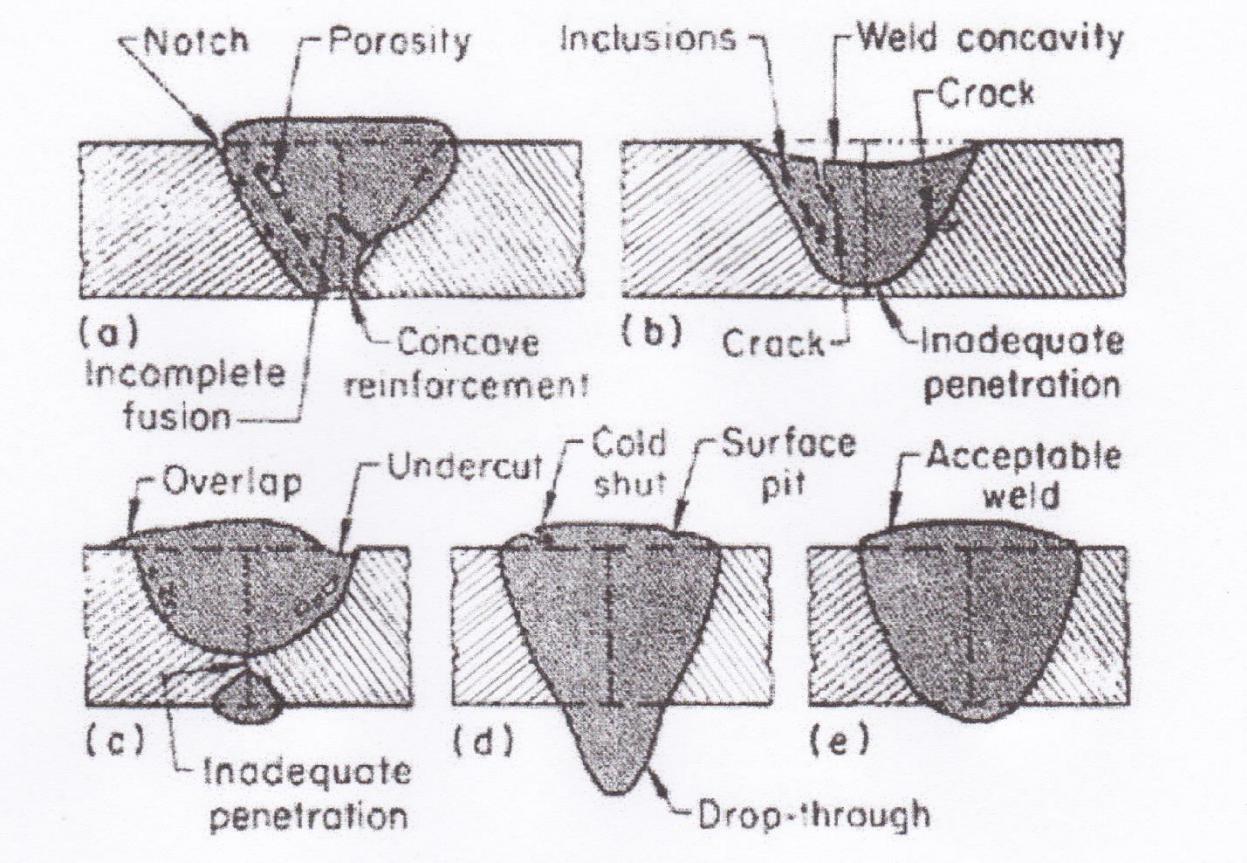

Figure 2.18 Typical weld defects [75].

Source – A Technical Guide (ASM International) by E.F. Bradley (1988). Reprinted with permission from ASM International (17th December, 2014).

(microscopic in size) are examples. These defects are as a result of the generation of high stress/strain during the welding process and also dependent on the properties of the material.

Generally, cracks that form during welding can grouped into two major types; namely, cracks that form specifically due to the welding process, and those that arise when the material is put into service. Hot cracking is a term that is used to particularly describe cracks that form in the HAZ and FZ during solidification from the weld thermal cycle or when a weldment is re-heated. Some examples of cracking are:

1. solidification cracking – occurs mainly in the FZ
2. liquation cracking – occurs in the HAZ
3. post weld heat treatment cracking – occurs in the FZ and HAZ
4. lamellar tearing – occurs in the HAZ close to FZ
5. cold cracking – occurs in the HAZ

2.12.3 Solidification Cracking

Solidification cracking typically occurs in the FZ and the cracks are usually intergranular [64]. Characteristically, solidification cracking shows the dendritic morphology as the weld metal solidifies. These cracks occur when partially solidified weld materials are unable to contain contraction stresses that are generated during weld cooling and solidification [76]. The loss in ductility is primarily due to mechanical (stresses and strains) and metallurgical factors (presence of low melting point constituents that are created when segregation occurs during liquid to solid phase transformation) [77]. In essence, it is not possible to prevent the mechanical factors that cause the loss of ductility since they arise from the solidification shrinkage of weld liquid and/or

thermal expansion and contraction of FZ and HAZ. The situation is worsened when solidification shrinkage occurs simultaneously with rapid precipitation of second phase particles that have significant disregistry with the matrix.

On the other hand, the metallurgical factors responsible for solidification cracking arise from the partitioning of elements during the initial stages of solidification, the amount/magnitude of which is dependent on the partitioning coefficient *k*. By definition, the partitioning coefficient '*k*' is the ratio of solid concentration to the liquid in equilibrium with it [64]. Smaller values of *k* means higher tendency for an alloying element to segregate into the solidifying liquid. Hence, elements such as S, O, B, P, C, Ti, N and H in complex austenitic matrixes of high temperature alloys with *k* values less than unity are susceptible to segregating into solidifying liquid where they create low melting phases and eutectics with the metal to produce wetting films at grain boundaries. The combination of a persistent wetting film, at grain boundaries, and a weld that is partially solidified leads to a reduction in the surface to surface contact strength at the grain boundaries, consequently leading to poor ductility of the metal. Once the amount of contraction stresses becomes higher than the rupture strength of the grain boundaries or cohesive strength of the grain, cracks will form.

2.12.4 Liquation Cracking

Liquation cracking usually occurs in the HAZ (which comprises both the PMZ and the true HAZ), and is often accompanied by a liquid phase at the intergranular fracture surface [64]. Liquation cracking is a major issue that constrains on the applications of a wide range of nickel-based superalloys, both cast and wrought types. Furthermore, unlike solidification cracking which can be controlled to some extent, liquation cracking is more destructive and not easy to restrain. This

is because the factors responsible for its occurrence in a material are usually associated with the optimized chemistry and microstructure of the material. The presence of tensile welding stress and a microstructure susceptible to crack, for instance, liquated grain boundaries, facilitate the occurrence of liquation cracking. Liquation cracking leads to a situation where a solid-solid interfacial bond of the boundaries is substituted with a weaker solid-liquid bond. As a result, the magnitude of tensile welding stresses that can be sustained by the grain boundaries before decohesion is significantly lessened. It is known that HAZ grain boundary liquation can result from either non-equilibrium phase transformation below an alloy bulk solidus or super-solidus melting above the equilibrium solidus of the alloy [78-79]. Nevertheless, of the two, non-equilibrium subsolidus melting is worse because it limits the effective melting temperature range and increases the size of the region that is susceptible to cracking [80-81].

2.13 Fatigue Behaviour of Welded Components

The use of welding for fabrication of components can lead to the introduction of features such as residual stresses, imperfections, and stress concentrations in the welded material [82]. Typically, failures in engineering structures occur at component connections. By definition, the connections in a component are the sections of the component structure where elements are connected to rectify changes in geometry and/or accommodate requirements that are either fabrication or service related. For example, fatigue cracking in buildings, offshore structures, bridges, and pressure vessels most often than not arise at the welded or bolted connections and attachments such as the cover plate fillet weld terminations, stiffeners, backing bars, and seam and girth weld toes [82].

The stresses that are applied onto structures and components during service could be within an acceptable design range; however, it does not preclude the occurrence of failure. This is because welded and bolted connections can increase the localized stresses to a magnitude high enough to initiate and propagate cracks [82]. Usually, fatigue cracks originate from discontinuities within the weld or base metal. These discontinuities can be volumetric (e.g., porosity, slag inclusions) or planar (e.g., lack of fusion, undercut) in nature and in either case, sufficiently increase local stresses to reduce weld joint fatigue strength. Additionally, the geometry of the weld itself can induce stress concentrations where the magnitudes exceed those associated with the aforementioned weld discontinuities. For instance, one of the most fatigue-sensitive weld details is a fillet weld termination oriented perpendicular to the applied cyclic stress field. In this instance, fatigue cracking initiates from the toe of the fillet weld and propagates through the adjacent base metal. As a matter of fact, the majority of weld related fatigue failures initiate at the surface, generally at the weld toe. As a result, the overall fatigue strength of a welded joint will be dictated by the combined severity of the weld discontinuity and geometry-induced stress concentration. On the other hand, residual stress, distortion, heat treatment, environment, as well as others, are other parameters that are also known to influence the behaviour of welded components [82].

CHAPTER 3

EXPERIMENTAL PROCEDURES

This chapter presents the details of the experimental procedures and instruments used. The experimental procedure for performing fatigue tests on unwelded samples is discussed first, followed by the experimental procedure for performing fatigue tests on welded samples. This is consistent with the chronological order followed in performing the required experiments.

3.1 Materials

The wrought Haynes 282 alloy used in this study was supplied by Haynes International Inc. in the form of bright-annealed plates with a mill finish, with dimensions of 610 mm x 120 mm x 11 mm. The nominal chemical composition (weight %) of the alloy is 1.5Al, 2.1Ti, 10Co, 20Cr, 8.5Mo, 1.5Fe, 0.3Mn, 0.15Si, 0.06C, 0.005B, and the balance nickel.

To investigate the effect of LBW on the fatigue properties of Haynes 282, fatigue tests were carried out on both unwelded and welded Haynes 282 specimens.

3.2 Experimental procedure for fatigue tests on unwelded samples

The as-received material which had a thickness of approximately 11 mm was sectioned into 3 mm thick rectangular plates by using an electro-discharge machining (EDM) equipment. Subsequently, the fatigue samples were carefully machined to the final dimensions. After machining, the fatigue samples were subjected to a standard heat treatment which consisted of a solution heat treatment of 1130°C/2 h/water-quench followed by ageing at 1010°C/2 h/air-cool and 788°C/8 h/air-cool. A Marshal tube furnace connected to a digital programmer was used to conduct the heat treatment.

3.2.1 Low Cycle Fatigue Test

The strain-controlled LCF test specimens were machined to final dimensions of 10.5 mm in gauge length, 5 mm in gauge width and a thickness of 3 mm. Strain-controlled LCF push-pull type of fatigue test was conducted by using an Instron servo hydraulic fatigue testing system. The LCF tests was carried out at a zero mean strain and at room temperature using a constant strain rate of 1×10^{-2} s^{-1}. Triangular loading waveform was applied during the testing and the total strain amplitude varied from 0.5% to 1.0%.

3.2.2 Fatigue Crack Growth Test

Compact tension test specimens with dimensions of 31.5 mm x 25 mm x 3 mm were used to determine FCG rates at temperatures of 25°C and 600°C. After the full heat treatment, the notch tips, from which the fatigue crack was initiated, were added using an EDM equipment. The FCG fatigue specimens were then ground and polished to remove oxides and simplify the visual monitoring of the crack growth. Thereafter, precracking was done in accordance with ASTM E647-99 to produce sharp cracks that eliminate notch machining effects. An Instron servo hydraulic fatigue testing system was used for this purpose. Upon achieving an acceptable precrack length, FCG testing was conducted on the fatigue testing system which was interfaced with a computer for the test control and data acquisition. A sinusoidal loading waveform at frequencies of 0.05 and 15 Hz and two stress ratios of 0.1 and 0.7 were used. All tests were performed in laboratory air. Crack lengths were measured using a direct current potential drop (DCPD) technique. Load shedding technique, using an automated decreasing stress intensity range (ΔK) procedure, in accordance with ASTM E647-99, was used to determine the near threshold FCG rates. The K-gradient, $C = (1/K)(\Delta K/da)$, was selected to be -0.1.

For the high temperature tests, a split furnace was used to heat the specimens. The furnace is constructed with a stainless steel shell with nickel plated end flanges. The insulation is a low "K" factor vacuum cast ceramic fiber to provide minimum heat loss, high temperature capability and rigid structure. The end caps are removable and may be adjusted or modified as required. The full length hinge ensured good alignment and sealing as well as maximum access to the interior.

3.2.3 Microscopic Observation

The microstructure of Haynes 282 in its standard heat treatment condition was first examined using a ZEISS Axiovert 25 inverted reflected light optical microscope interfaced with CLEMEX Vision 3.0 image analysis software. The microscope was also used to examine the FCG paths, developed in a specimen, after testing. A more detailed microstructural study of Haynes 282 was carried out using a JEOL 5900 scanning electron microscope (SEM) equipped with an Oxford Instrument ultra-thin window energy dispersive spectrometer (EDS). The SEM was also used to observe the fracture surfaces of tested FCG specimens. JEOL 2000FX transmission electron microscope (TEM) was also used to carry out more detailed microstructural studies.

3.3 Selection of appropriate pre-weld heat treatment for Haynes 282

Welding test coupons measuring 65 mm x 15 mm x 3 mm were machined using the EDM equipment. They were then subjected to different pre-weld thermal treatments as shown in Table 3.1.

Prior to welding, the heat treated test coupons were surface ground and polished to remove surface oxides.

Table 3.1 Pre-weld heat treatments

Temperature (°C)	Duration (hrs)	Mode of Cooling
1030	2	Water-quench
1030	2	Furnace-cool
1060	2	Water-quench
1060	2	Furnace-cool
1090	2	Water-quench
1090	2	Furnace-cool
1100	2	Furnace-cool
1120	2	Water-quench
1120	2	Furnace-cool
1150	2	Water-quench
1150	2	Furnace-cool

3.3.1 Laser Beam Welding

The pre-weld heat treated test coupons were welded by bead-on-plate fiber LBW at Standard Aero Ltd., Winnipeg. The LBW parameters used are as shown in Table 3.2.

After welding, the welded coupons were cut transversely to the welding direction into ten sections at intervals of 3mm using the EDM equipment. The specimens were then mounted in bakelite, ground and polished using standard metallographic techniques for microstructural study. The polished specimens were subsequently chemically etched with modified kallings reagent – 40 ml distilled water + 480 ml HCl + 48 g $CuCl_2$. Afterwards, the etched specimens were observed in the SEM and the cracks found were measured.

3.4 Experimental procedure for fatigue tests on welded samples

For welding, test coupons measuring 132 mm x 31.5 mm x 3 mm were machined. The coupons were then subjected to a pre-weld thermal treatment which consists of a solution heat treatment of 1100 °C/2 h/furnace-cool. Prior to welding, the heat treated test coupons were surface ground and polished to remove surface oxides.

3.4.1 Laser Beam Welding

Pre-weld heat treated test coupons were welded by bead-on-plate fiber laser beam welding at Standard Aero Ltd., Winnipeg.

Table 3.2 Laser beam welding parameters

Type of Laser	Type of Laser Beam	Weld Type	Power (W)	Speed (m/min)	Focus (mm)	Welding Gas Flow Rate using Helium (litre/min)	Trailing Gas Flow Rate using Argon (litre/min)
Fiber	Continuous Wave	Bead on Plate	3000	2	-2	20	20

3.4.2 Post Weld Heat Treatment

After welding, the fatigue samples were carefully machined to final dimensions of 31.5 mm × 25 mm × 3 mm (Figure 3.1 shows the locations of the welds relative to specimen geometry). After machining, the fatigue samples were subjected to different post weld heat treatments as shown in Table 3.3.

3.4.3 Fatigue Crack Growth Test

After the post weld heat treatments, the notch tips from which the fatigue crack was initiated were added. The FCG fatigue samples were then grounded and polished. Thereafter, precracking was done, in accordance with ASTM E647-99, to produce sharpened cracks that eliminate notch machining effects. Upon achieving an acceptable precrack length, an optical microscope was used to measure the length. Fatigue testing was conducted on the Instron Servo hydraulic fatigue testing system which was interfaced with a computer for the test control and data acquisition. A sinusoidal loading waveform at frequencies of 0.05 and 15 Hz, and two stress ratios of 0.1 and 0.7 were applied. All tests were performed in laboratory air at a temperature of 600 °C. Crack lengths were measured by using a DCPD technique. Load shedding technique, using an automated decreasing stress intensity range (ΔK) procedure, in accordance with ASTM E647-99, was used to determine the near threshold FCG rates. The K-gradient, $C = (1/K)(\Delta K/da)$, was selected to be −0.1.

A split furnace was used to heat the samples. The furnace is constructed with a stainless steel shell with nickel plated end flanges.

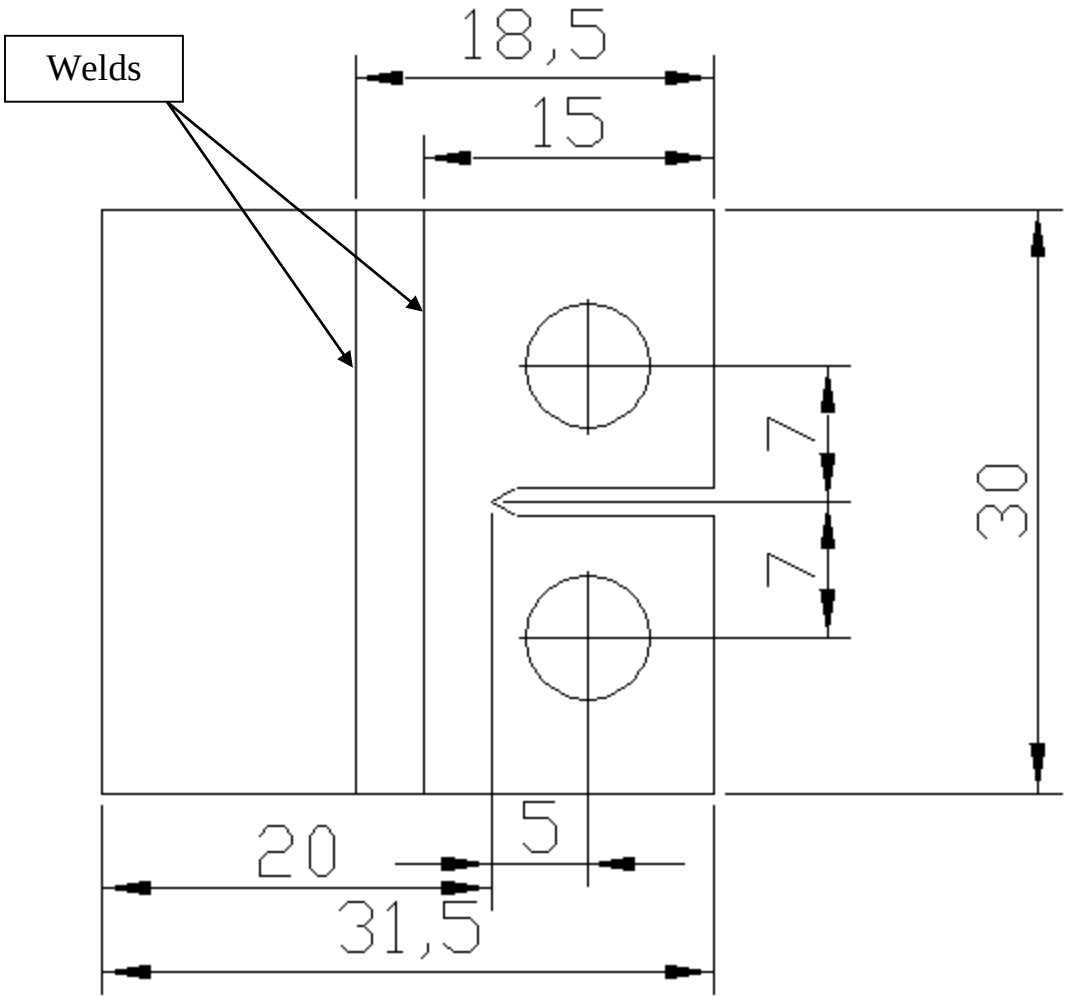

ALL DIMENSIONS ARE IN MILLIMETERS

Figure 3.1 Geometry of FCG test specimen.

Table 3.3 Post weld heat treatments

	Solution Heat Treatment	First Stage of Ageing	Second Stage of Ageing
Heat Treatment A	1130°C/2 h/water-cool	1010°C/2 h/air-cool	788°C/8 h/air-cool
Heat Treatment B	1150°C/2 h/water-cool	1010°C/2 h/air-cool	788°C/8 h/air-cool
Heat Treatment C	1130°C/2 h/water-cool	1010°C/2 h/air-cool	788°C/8 h/furnace-cool

3.4.4 Microscopic examination

Optical microscopy, by using a ZEISS Axiovert 25 inverted-reflected light microscope, equipped with CLEMEX Vision 3.0 image analysis software, was used to examine the FCG paths after testing. Additionally, a JEOL 5900 scanning electron microscope (SEM) equipped with an Oxford Instrument, ultra-thin window energy dispersive spectrometer (EDS), was used to observe the fracture surfaces of the tested FCG samples. JEOL 2000FX transmission electron microscope (TEM) was also used to carry out more detailed microstructural studies.

CHAPTER 4

RESULTS AND DISCUSSION

4.1 Microstructure of as-received Haynes 282 alloy

As observed in a previous work [9] the microstructure of as-received Haynes 282 alloy is made up of a gamma (ɣ) solid solution matrix with an average grain size of ≈140 μm and MC carbides (M being mostly Ti and Mo) which are randomly dispersed as intergranular and intragranular particles within the ɣ matrix. The size of the carbide particles range from about 2 to 15 μm. Typically, MC-type carbides are generated through the crystallization of the liquid melt as the cast ingot solidifies [83]. It was reported that the MC-type carbides are metastable and have the propensity to dissolve or dissociate during high temperature thermal treatment [22, 83]. The main strengthening phase of the alloy, the ɣ phase, was not observed using the SEM.

4.2 Microstructure of Standard Heat Treated Haynes 282

Figure 4.1 shows optical and SEM micrographs of Haynes 282 in the standard heat treatment condition prior to fatigue testing. The average grain size of Haynes 282 in this condition, as determined by the linear intercept method by using optical micrographs, is approximately 250 μm. The microstructure consists mainly of MC carbides which are distributed in the alloy matrix.

Since the ɣ′ phase could not be detected using SEM, TEM was used to further analyze the microstructure of the heat treated alloy. Figure 4.2(a) shows a dark field TEM micrograph of ɣ′ precipitates in heat treated Haynes 282 and its accompanying super lattice diffraction pattern is shown in Figure 4.2(b).

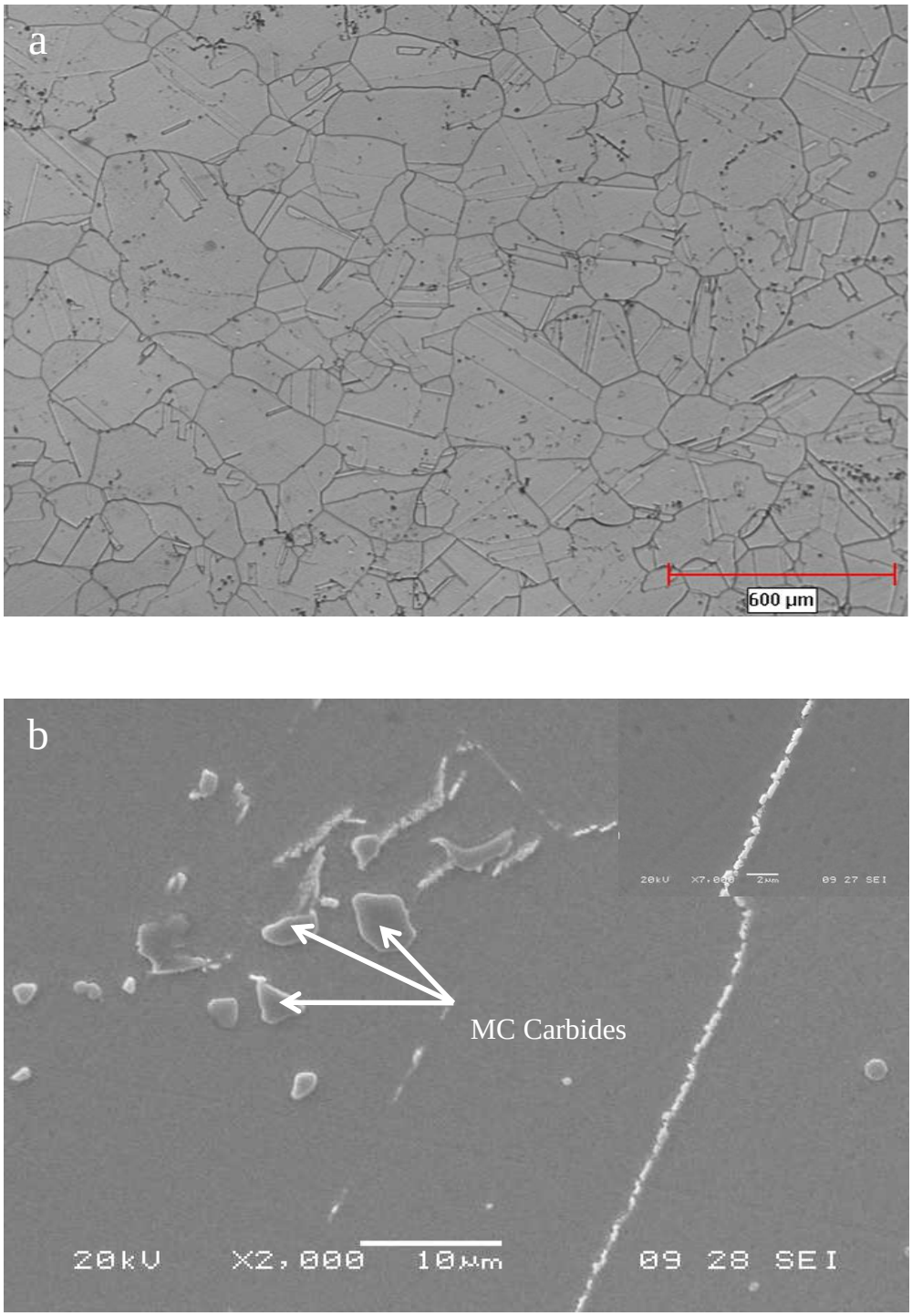

Figure 4.1 (a) Optical and (b) SEM micrographs of Haynes 282 in the standard heat treated condition.

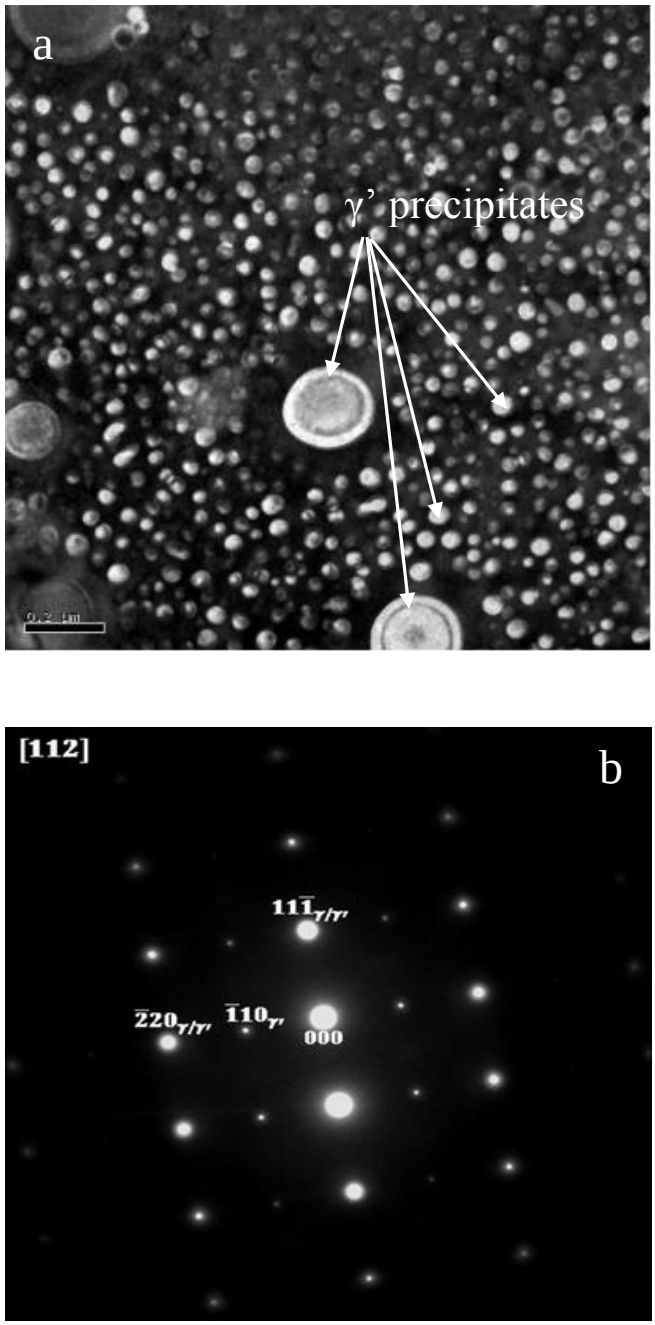

Figure 4.2 (a) TEM dark field image of Haynes 282 showing ɣ′ precipitates and (b) TEM selected area diffraction pattern [112] zone axis showing superlattice reflections of ɣ′ precipitates.

4.3 Low Cycle Fatigue

4.3.1 Stress Response During Cyclic Deformation

The variation of stress response with cyclic straining is an important feature of the LCF process [84]. The cyclic stress response curves illustrate the variation of cyclic stress amplitude with the number of loading cycles, during a total strain amplitude controlled LCF test. They illustrate the path through which the material arrives at its final flow stress level [84].

Figure 4-3 shows the variation of cyclic stress amplitude with number of cycles at different strain amplitudes. It is observed that at all the strain amplitudes used in this work, the alloy cyclically hardened within the first few cycles of straining after which a gradual cyclic softening followed till the end of life of the specimens. This trend was observed in the cyclic stress response of other precipitation strengthened superalloys [85-87]. The likely causes of the cyclic hardening was reported to be due to formation of cottrell-lomer locks, accumulation of forest dislocations, and increase in the density of slip bands at the beginning of cycling [87].

However, the occurrence of cyclic hardening in a superalloy at room temperature cannot be attributed to either the accumulation of forest dislocations or the formation of cottrell-lomer locks without significant occurrence of cross slip [87]. This is because these two mechanisms involve interaction of dislocations on multiple slip systems through the cross slip process. For an FCC alloy such as Haynes 282, it is unlikely that cross slip will occur at room temperature due to the confinement of dislocations motion to the {111} planes [88]. Thus, for such an alloy, an increase in the density of slip bands at the beginning of the cycling is most likely responsible for the cyclic hardening. An increase in the density of slip bands was reported to be responsible for the cyclic

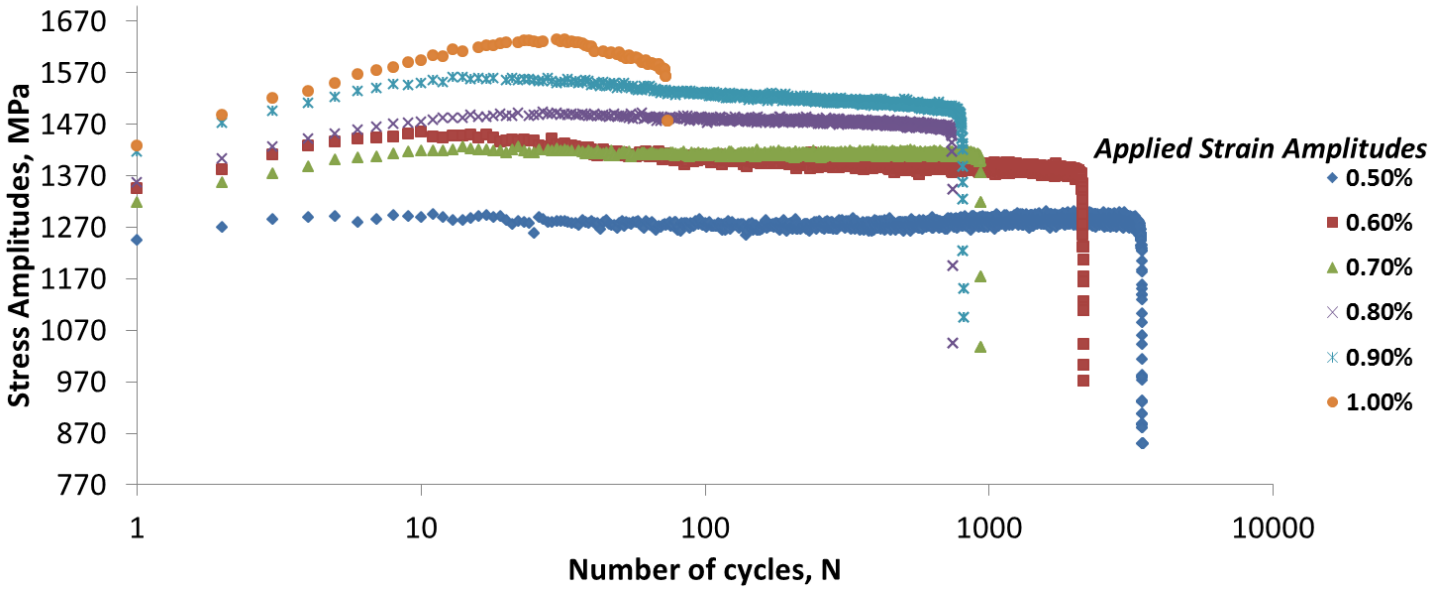

Figure 4.3 Cyclic stress amplitude versus the number of cycles at different strain amplitudes.

hardening observed in a similar ɣ′ precipitation strengthened nickel-base superalloy, Nimonic 80A [89].

As is characteristic of precipitation strengthened alloys, Haynes 282 exhibited softening in the later stages of the deformation after it cyclically hardened to a peak stress. It was suggested that the cessation of the initial hardening in a precipitation strengthened alloy could be attributed to the formation of an equilibrium number of slip bands that corresponds to the applied strain [87]. Other possible explanations for the softening behavior include: (i) precipitate dissolution [90], (ii) disordering of precipitates [91], (iii) precipitation shearing [92], (iv) formation of stable phases [93], and (v) growth of precipitates [94].

The last two mechanisms occur only at high temperatures [95], while the first three can occur at both room and high temperatures [87].

In this work, cyclic softening was not due to precipitate dissolution because ɣ′ precipitates were still present after testing as shown in Figure 4.4. It was also not due to disordering of precipitates since, as observed in Figure 4.5, the TEM selected area diffraction pattern at [112] zone axis shows superlattice reflections of ɣ′ precipitates. This indicates the presence of ordered ɣ′ precipitates after testing. As such, the most probable cause of cyclic softening was precipitate shearing. Figure 4.6 shows sheared ɣ′ precipitates. Moreover, considering the extent of the strain involved in the test, it is most likely that the softening observed during the cyclic loading was due to precipitate shearing. It was reported that precipitate shearing was responsible for cyclic softening in Waspaloy [86, 96], a nickel-based superalloy that has microstructural features similar to those of Haynes 282.

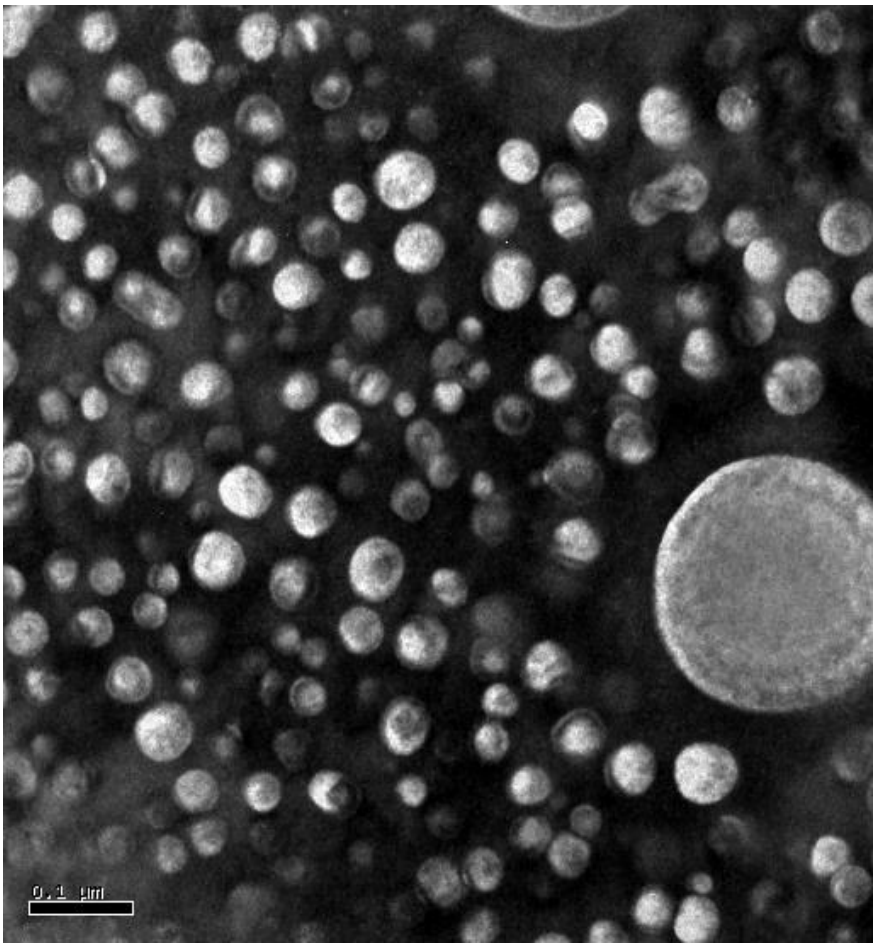

Figure 4.4 Presence of gamma prime precipitates after LCF testing.

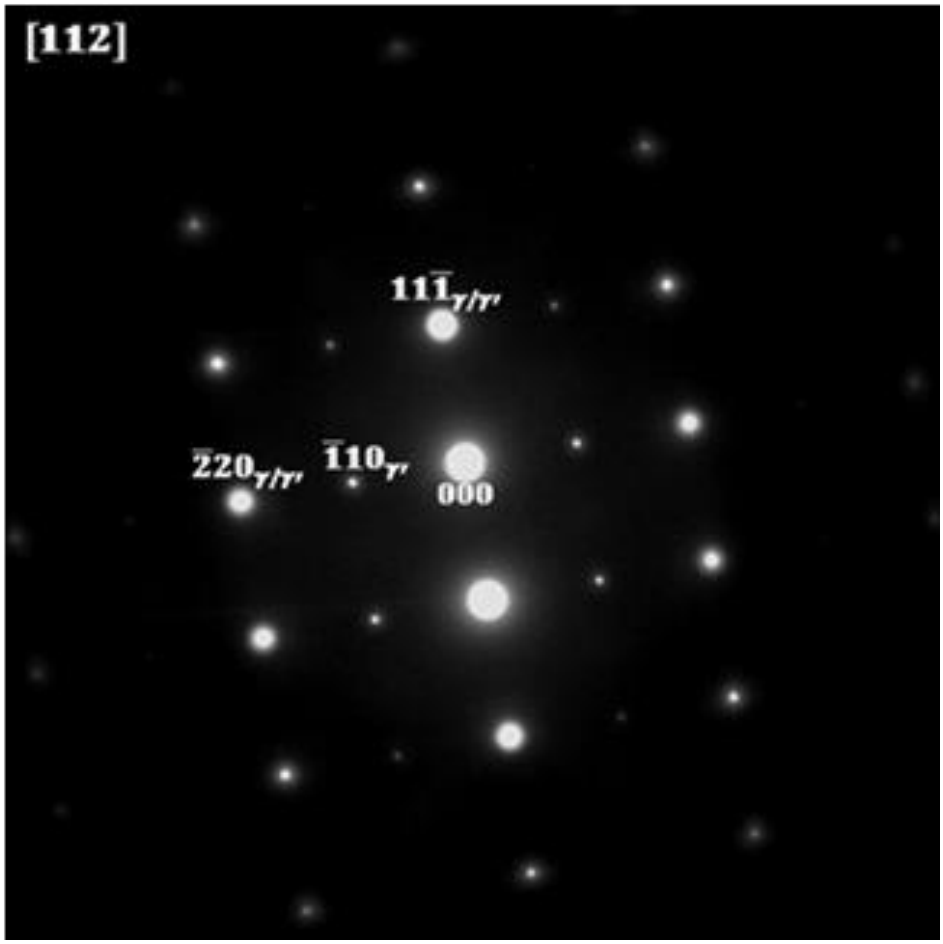

Figure 4.5 TEM selected area diffraction pattern at [112] zone axis showing superlattice reflections of ɣ′ precipitates.

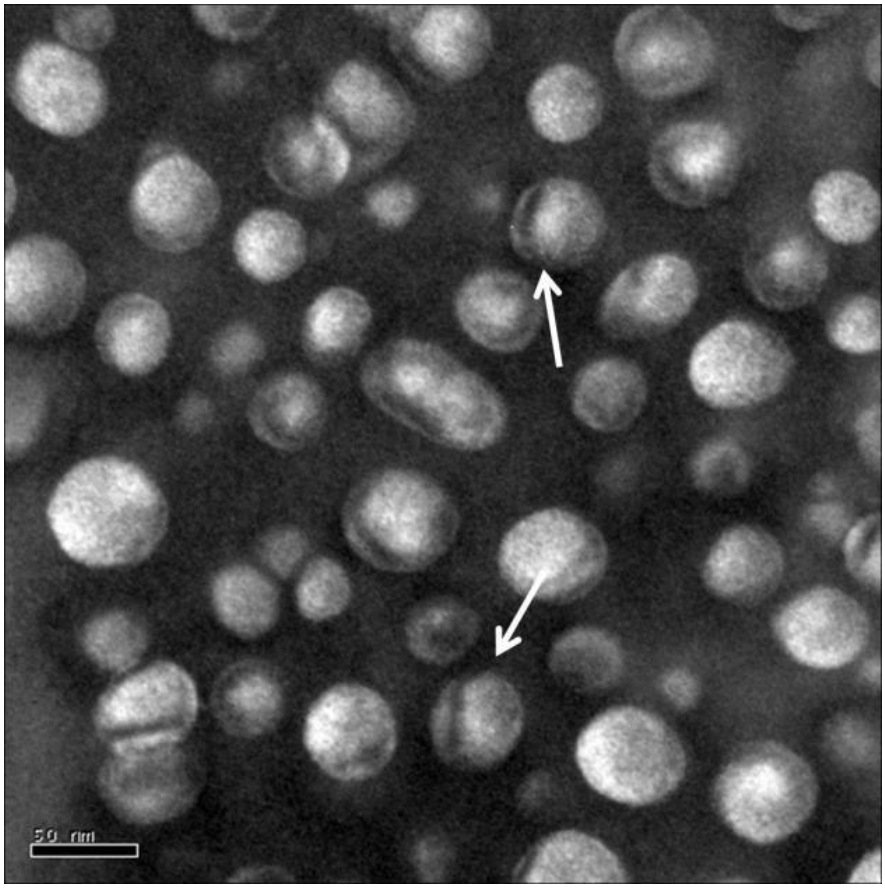

Figure 4.6 TEM ɣ′ precipitates can be seen to be sheared in this transmission electron micrograph.

4.3.2 Low Cycle Fatigue Properties

Figure 4.7 shows the fatigue life curve for the cyclic plastic strain amplitude obtained for heat treated Haynes 282. There exists a dual slope behavior which is consistent with the Coffin-Manson relationship. The bilinearity in slope is of practical significance because an extrapolation based on any one segment would lead to overestimation of fatigue lives [85]. Similar dual slope behavior in the Coffin-Manson relationship was observed in other precipitation strengthened alloys [85, 87]. Several explanations [96, 97] have been offered for this. However, change in the deformation mode of a material is believed to be responsible for this phenomenon.

The other relationship that relates cyclic fatigue life to cyclic strain amplitude is the Basquin equation**.** Figure 4.8 shows the fatigue life curve for cyclic elastic strain amplitude obtained in this work. This curve, together with Figures 4.7 and 4.9, is critical in the determination of the LCF parameters enumerated in Table 4.1. These parameters are required for the calculation of the fatigue life of the material.

A comparison of the cyclic deformation parameters with those in the literature data is rather challenging. This is because fatigue properties are considerably influenced, at least at room temperature, by many factors such as: surface preparation [98], microstructure [99] and defects [100]. Nevertheless, the data from this research is comparable with the values obtained for other alloys at room temperature; this is shown in Table 4.1. The new superalloy, Haynes 282, exhibited relatively high values of cyclic strain hardening exponent (n'), cyclic strength (k'), fatigue strength (σ_f'), and fatigue ductility coefficients (ε_f'), which are all indicative of strong resistance to cyclic deformation.

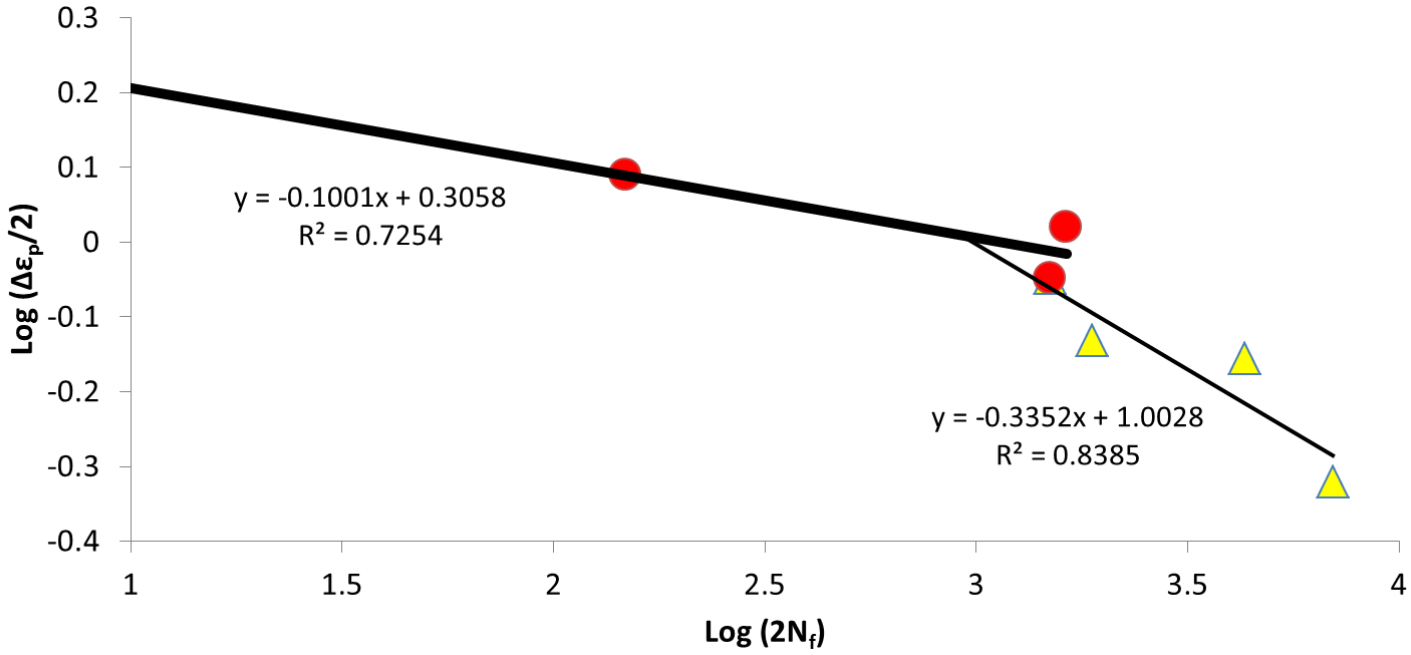

Figure 4.7 Coffin-Manson plot for Haynes 282 tested at 25°C.

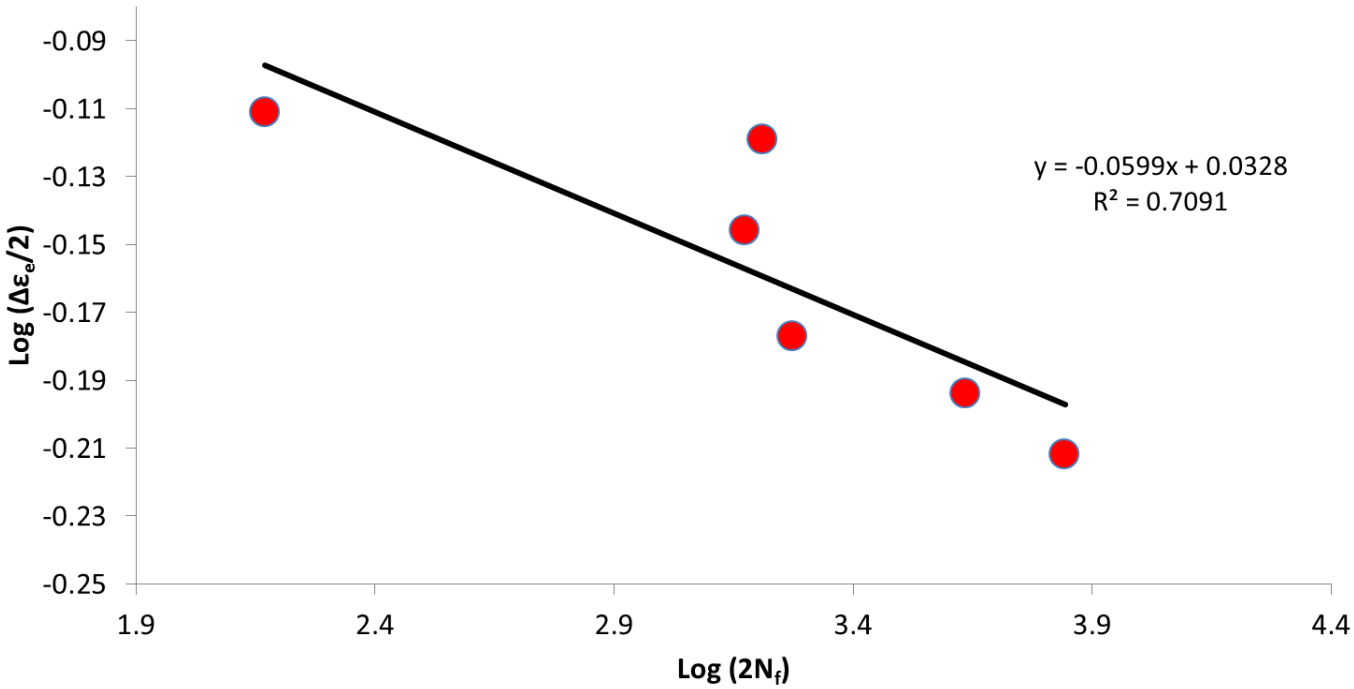

Figure 4.8 Basquin plot for Haynes 282 at 25°C.

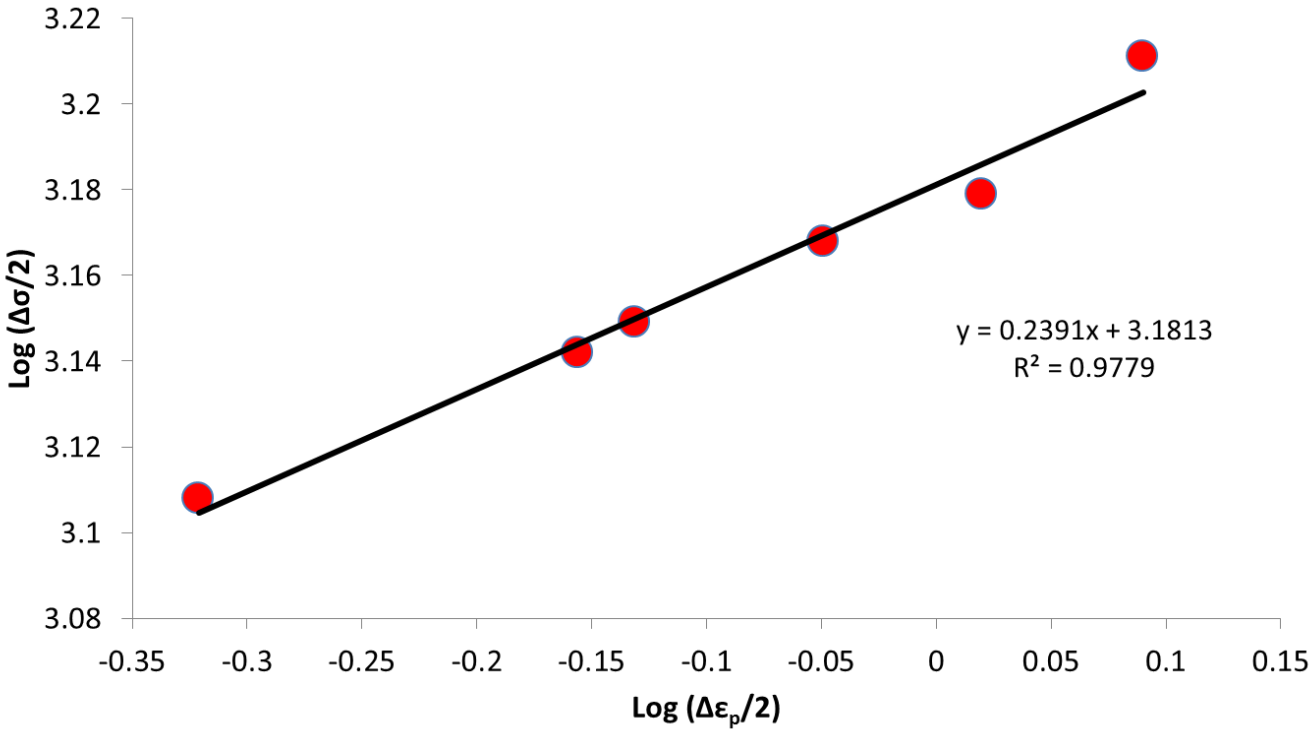

Figure 4.9 Cyclic stress-strain curve of Haynes 282 tested at 25°C.

Table 4.1 Low cycle fatigue properties of various alloys at room temperature compared with those of Haynes 282.

Alloy	Cyclic strain hardening exponent, n'	Cyclic strength coefficient, K', MPa	Fatigue strength coefficient, σ_f', GPa	Fatigue strength exponent, b	Fatigue ductility coefficient, ε_f', %	Fatigue ductility coefficient, ε_f', % (low plastic strain region	Fatigue ductility coefficient, ε_f', % (high plastic strain region)	Fatigue ductility exponent, c	Fatigue ductility exponent, c, (low plastic strain region)	Fatigue ductility exponent, c, (high plastic region)
Haynes 282	0.24	1518	232	-0.06	N/A	1006	202	N/A	-0.34	-0.1
Haynes HR -120	0.21	1174	1.4	-0.13	76.84	N/A	N/A	-0.54	N/A	N/A
720Li	{-}	{-}	{-}	{-}	N/A	48000	10.7	N/A	-1.52	-0.45
IN 718	{-}	{-}	{-}	{-}	N/A	476	5.2	N/A	-0.83	-0.31
IN 792-5A	{-}	{-}	1.6	-0.1	5.1	N/A	N/A	-0.75	N/A	N/A
TiAl	0.07	903	0.5	-0.02	0.1	N/A	N/A	-0.29	N/A	N/A
AZ31 Magnesium	0.34	1976	0.6	-0.15	1.78	N/A	N/A	-0.4	N/A	N/A

4.3.3 Cyclic Stress versus Strain Response

Figure 4.9 shows the cyclic stress-strain curve obtained in this work. The cyclic stress-strain curve was constructed by plotting the logarithm of stress amplitude ($\Delta\sigma/2$) as a function of the logarithm of plastic strain-amplitude ($\Delta\varepsilon_p/2$) both taken at half-life and was based on equation 4.2 [101]:

$$\frac{\Delta\sigma}{2} = K' \left[\Delta\varepsilon_p/2\right]^{n'} \quad \text{.....(4.2)}$$

where K' is the cyclic strength coefficient and the exponential term n' is the cyclic strain hardening exponent. The cyclic strain hardening exponent provides a measure of the response of a material to cyclic straining.

4.4 Fatigue Crack Growth

4.4.1 Effect of Stress Ratio

Figure 4.10 shows a plot of *da/dN* (crack growth rates) versus *ΔK* (stress intensity factor range) of Hayes 282 at 25°C, two frequencies (0.05 Hz and 15 Hz), and two stress ratios (0.1 and 0.7). As shown in Figure 4.10, an increase in the stress ratio from 0.1 to 0.7 increased the FCG rate at both testing frequencies (0.05 and 15 Hz). However, for both frequencies, over a relatively small stress intensity range (*ΔK*), the FCG rate at 0.1 is higher than that at 0.7. Ideally, due to less crack closure at a higher stress ratio, the FCG rate is expected to increase with an increase in stress ratio.

The extent of plastic deformation at the crack tip is a function of the applied stress ratio, and each growing fatigue crack is preceded by a plastic zone [28]. As moving dislocations impinge on grain boundaries, new dislocations are generated within adjacent grains [28].

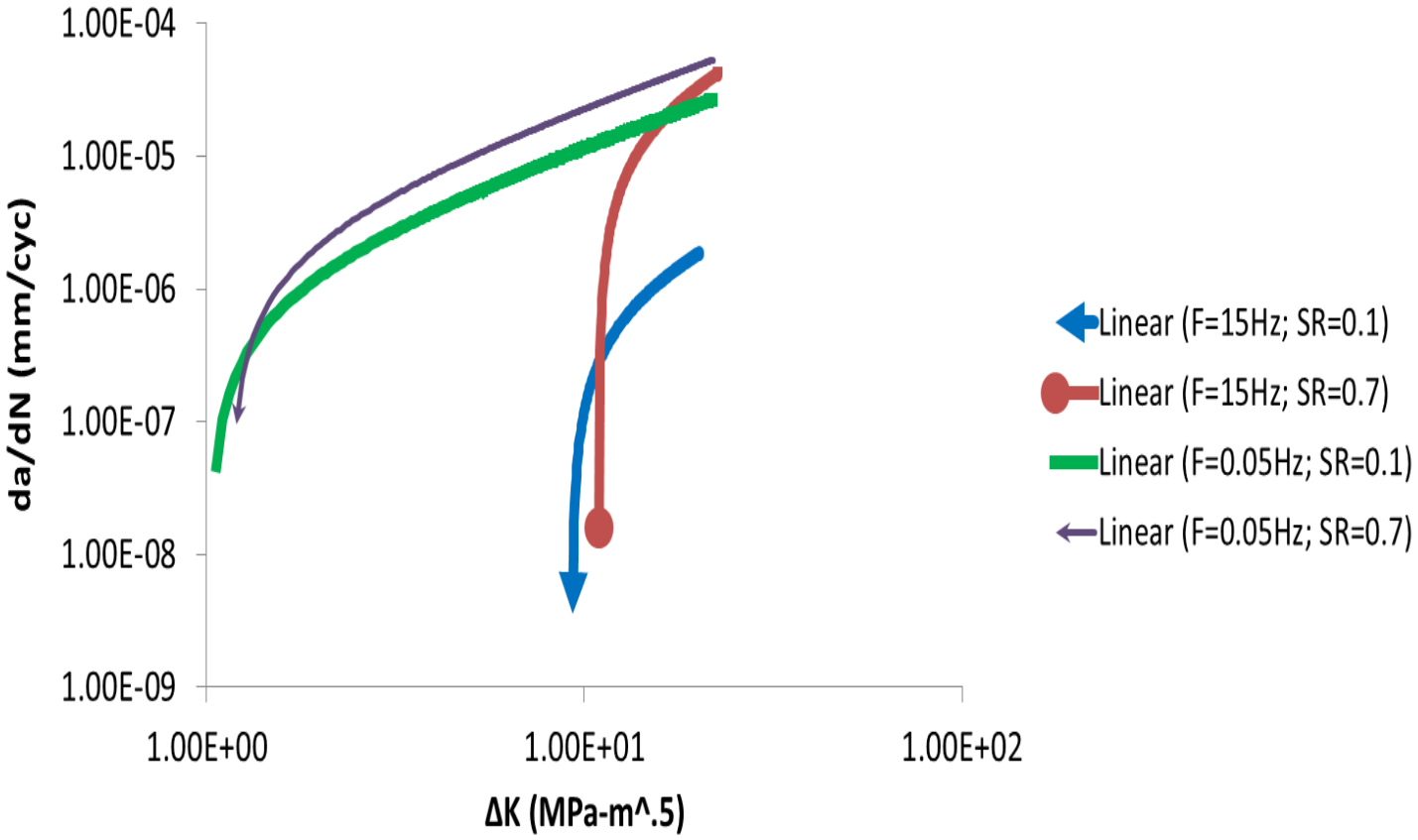

Figure 4.10 Crack growth rate versus stress intensity factor range of Haynes 282 at 25°C.

Since the extent of plastic deformation increases with an increase in the stress ratio at a given stress intensity, the plastic zone ahead of a growing crack will encompass more dislocations for the higher stress ratio of 0.7 compared to that of 0.1. The tangling of dislocations can give rise to the irreversibility of cyclic slip [29], and thus promote growth. Furthermore, an increase in dislocation density and subsequent dislocation tangling can accelerate damage accumulation within the plastic zone ahead of the advancing crack at the stress ratio of 0.7. Faster damage accumulation results in higher crack growth rates [28], which may be responsible for the increase in FCG rate with increase in stress ratio that is observed in the present work.

4.4.2 Effect of Frequency

As shown in Figure 4.10, a decrease in frequency from 15 to 0.05 Hz increased the rate of FCG at both test stress ratios (0.1 and 0.7). Since the room temperature tests performed in this work are not done in a corrosive medium, the observed effect of frequency may be attributed to the influence of the strain rate [49, 102].

An increase in frequency can cause an acceleration of the rate of strain at the crack tip. The increased strain rate involves the accumulation of higher density of dislocations, which upon interlocking with each other, leads to an increase in the yield strength of the material [49]. This results in the strengthening of the matrix near the crack and retards further propagation of the crack tip [49]. Hence, a higher frequency loading means lower cracking rate, as observed in the present work.

4.4.3 Effect of Temperature

Figures 4.11 to 4.14 are plots of *da/dN* (crack growth rates) vs. ΔK (stress intensity factor range) for Haynes 282 at two temperatures (25°C and 600°C), two frequencies (0.05 Hz and 15 Hz), and two stress ratios (0.1 and 0.7). It is observed that at a frequency of 15 Hz, the FCG rate consistently increased with increasing temperature at all stress intensities for both stress ratios. However, at a frequency of 0.05 Hz, over a relatively large stress intensity range (ΔK), the FCG rate decreased with temperature. Subsequently, the FCG rate increases with increasing temperature. The increase in FCG rate, with increasing temperature, has been reported to be due to: slip becoming more homogeneous, reduction in roughness induced crack closure, and a fall in the yield strength and modulus of elasticity of the material [32].

From the perspective of intrinsic toughening or material resistance, more homogeneous slip may lead to increased slip irreversibility [103, 104]. Consequently, there is more rapid crack advance along the slip bands, thus leading to lower intrinsic threshold values; since as suggested by Lukas, the threshold signifies the shift from reversible to irreversible dislocation processes within the slip bands [32].

Consistent with increasing slip homogeneity, an increase in temperature changed the fracture surface appearance from highly angular, at room temperature (Figure 4-15a), to flatter and smoother at 600˚C (Figure 4-15b) [32]. The flatter fracture surfaces means limited fracture surface mating can occur behind the crack tip. Therefore, there is a significant reduction in roughness induced crack closure, which results in an increase in the FCG rate at 600°C.

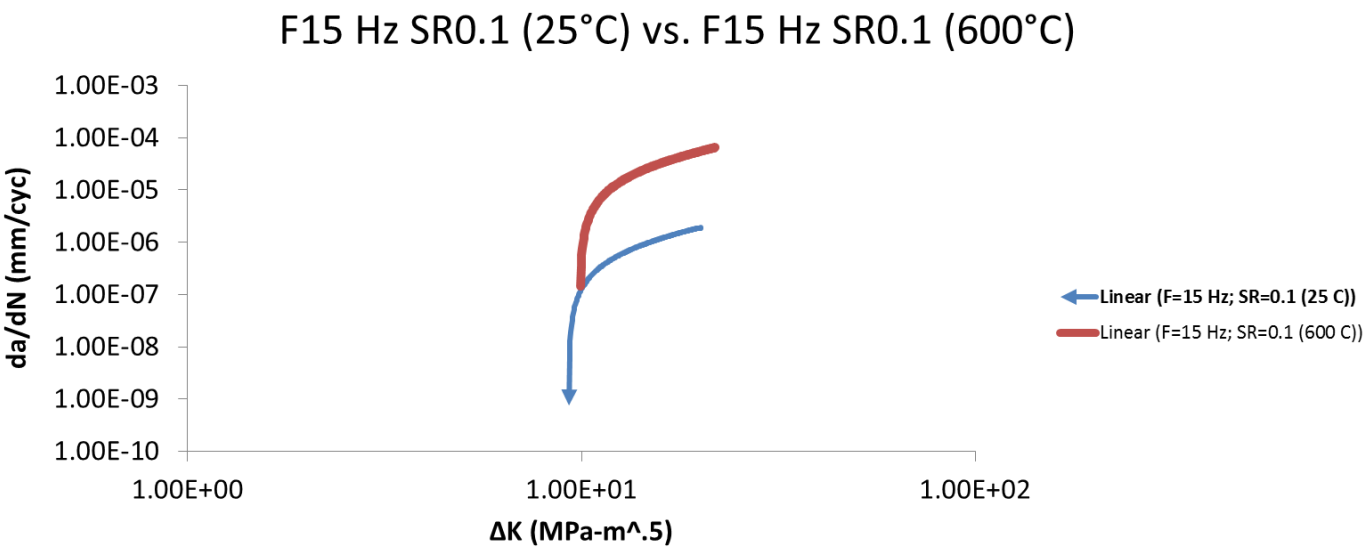

Figure 4.11 Effect of temperature on FCG rate of Haynes 282 at a frequency of 15 Hz and stress ratio of 0.1.

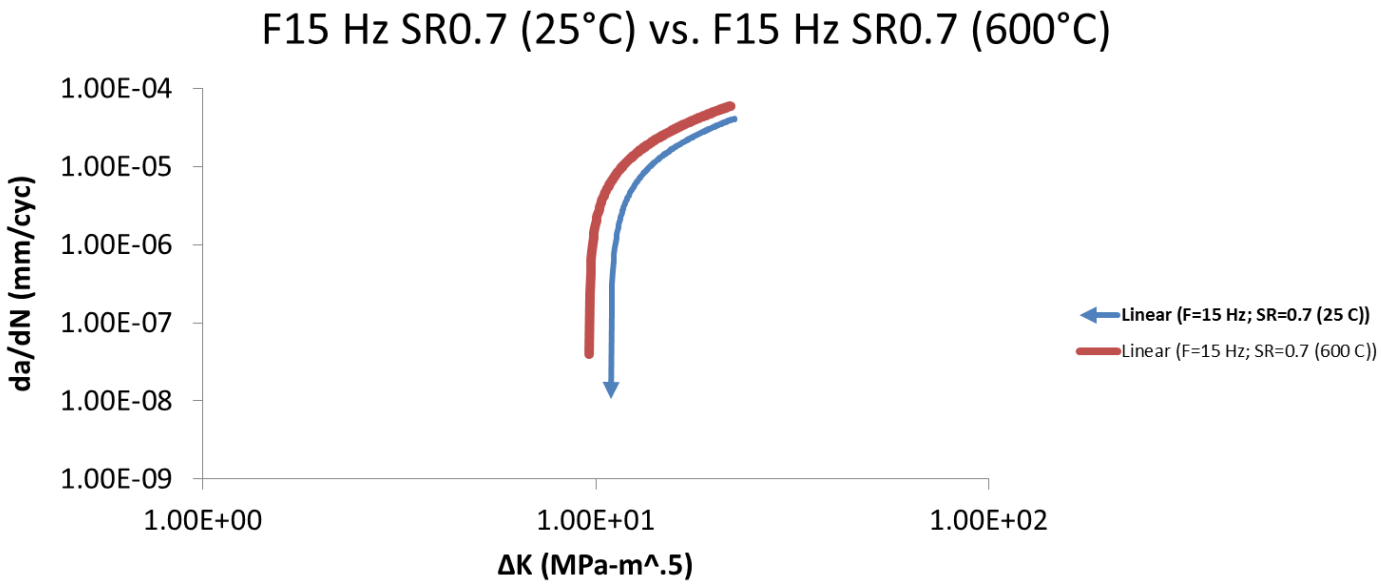

Figure 4.12 Effect of temperature on FCG rate of Haynes 282 at a frequency of 15 Hz and stress ratio of 0.7.

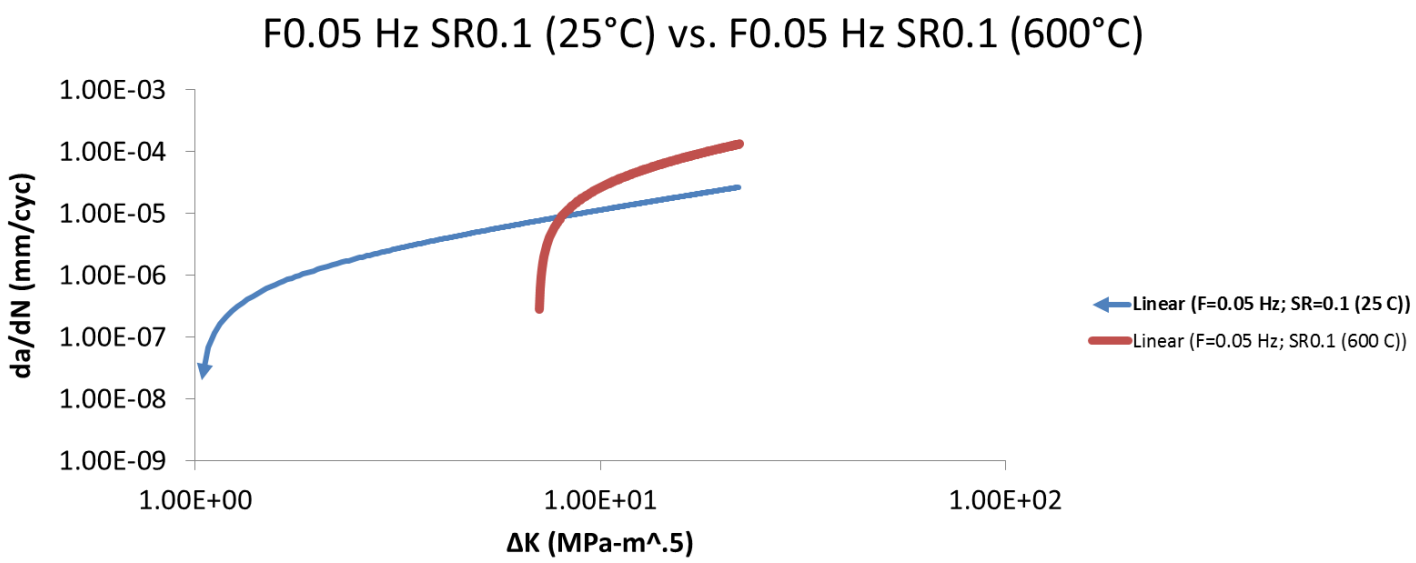

Figure 4.13 Effect of temperature on FCG rate of Haynes 282 at a frequency of 0.05 Hz and stress ratio of 0.1.

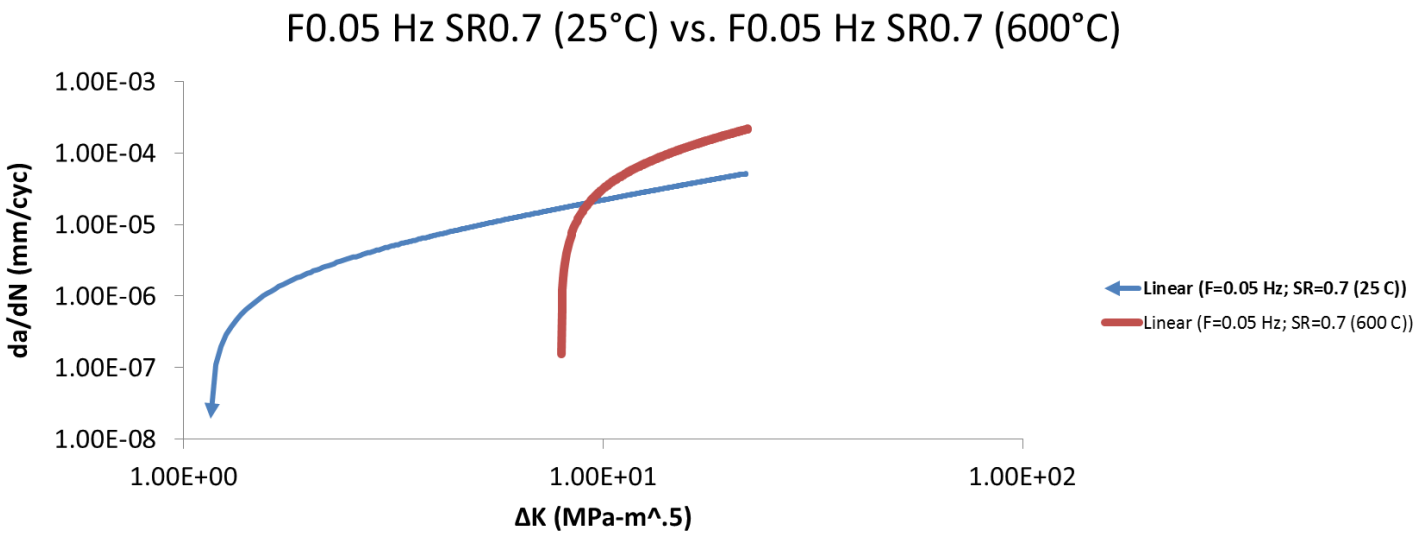

Figure 4.14 Effect of temperature on FCG rate of Haynes 282 at a frequency of 0.05 Hz and stress ratio of 0.7.

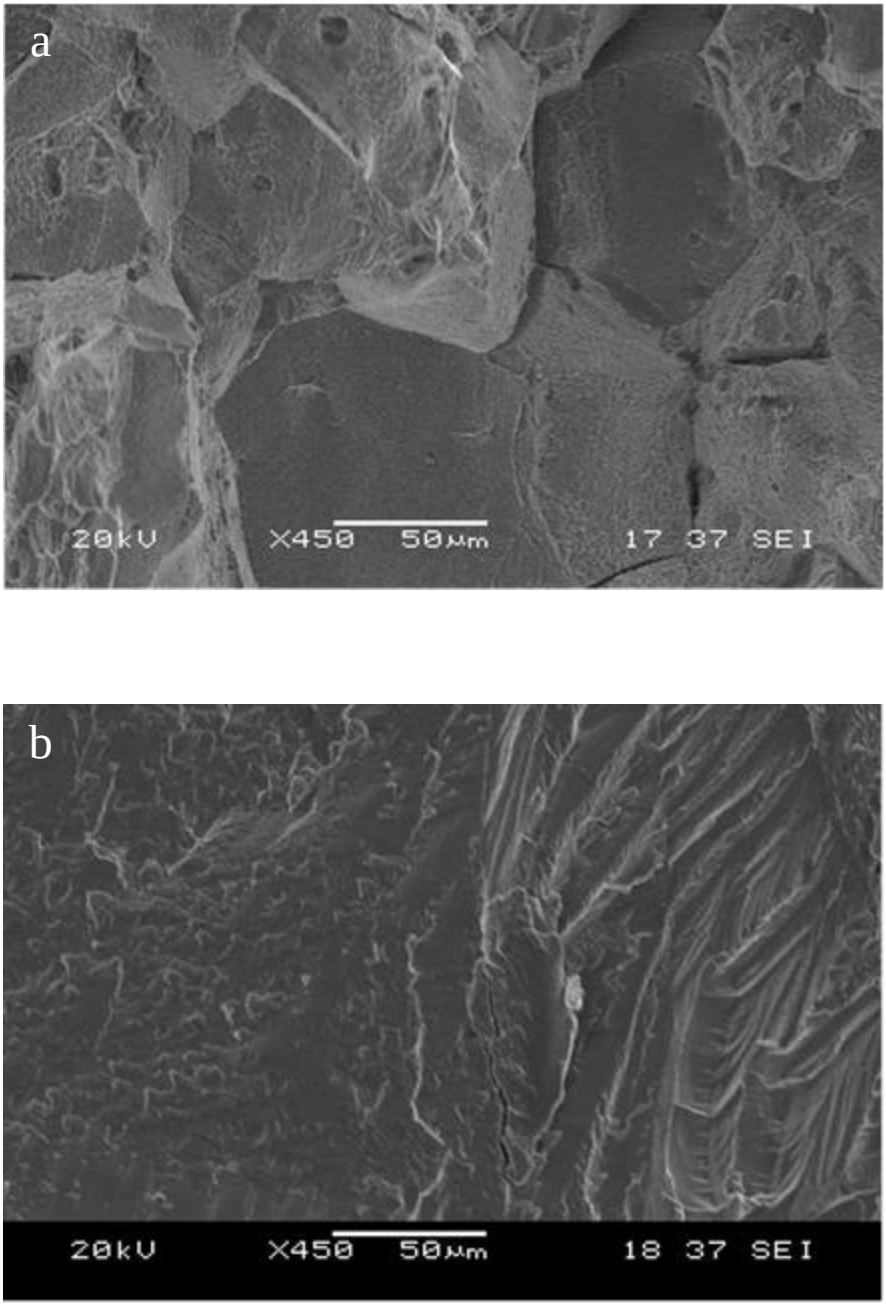

Figure 4.15 SEM micrographs showing the fracture surface of Haynes 282 at (a) 25 °C and (b) 600 °C.

Additionally, as expected with increasing slip homogeneity, the surface roughness of the material decreased as the temperature increased from 25ºC (Figure 4.15a) to 600ºC (Figure 4.15b) [32]. Furthermore, a comparison of Figures 4.16 and 4.17 shows that a minimized rough crack wake is associated with an increase in temperature. Thus, as the surface roughness decreased, the roughness of the crack wake also decreased. Hence, in comparison to 25°C, there is a less mating of the fracture surface behind the crack tip at 600°C. This leads to a reduction in roughness induced crack closure; hence, the FCG rate is increased at 600°C.

Moreover, since the fracture profiles show a more tortuous crack path, at 25°C (Figure 4.16), in comparison to 600°C (Figure 4.17), in essence, at 25°C, there is a longer actual crack path for the same projected crack length [32]. In addition, due to the more tortuous crack path, at room temperature, there is a greater deviation of the crack propagation path from the maximum tensile stress at 25°C [32]. Thus, the driving force of FCG, (ΔK), is reduced at room temperature. As a result, the FCG rate is increased at 600°C.

As mentioned earlier, a fall in the yield strength and modulus of elasticity of a material has been used by other researchers to explain the increase in the FCG rate with increasing temperature; this is because in the Paris regime, the fatigue behaviour can be dependent on the crack-tip strain range, or the range of crack opening displacement Δδ per cycle [32].

Since

$$\Delta\delta = Q\frac{\Delta K^2}{\sigma_{cy}E} \quad \text{.....(4.3)}$$

where Q is constant and σ_{cy} should be the cyclic yield stress (however, monotonic σ_y is often used as an approximation),

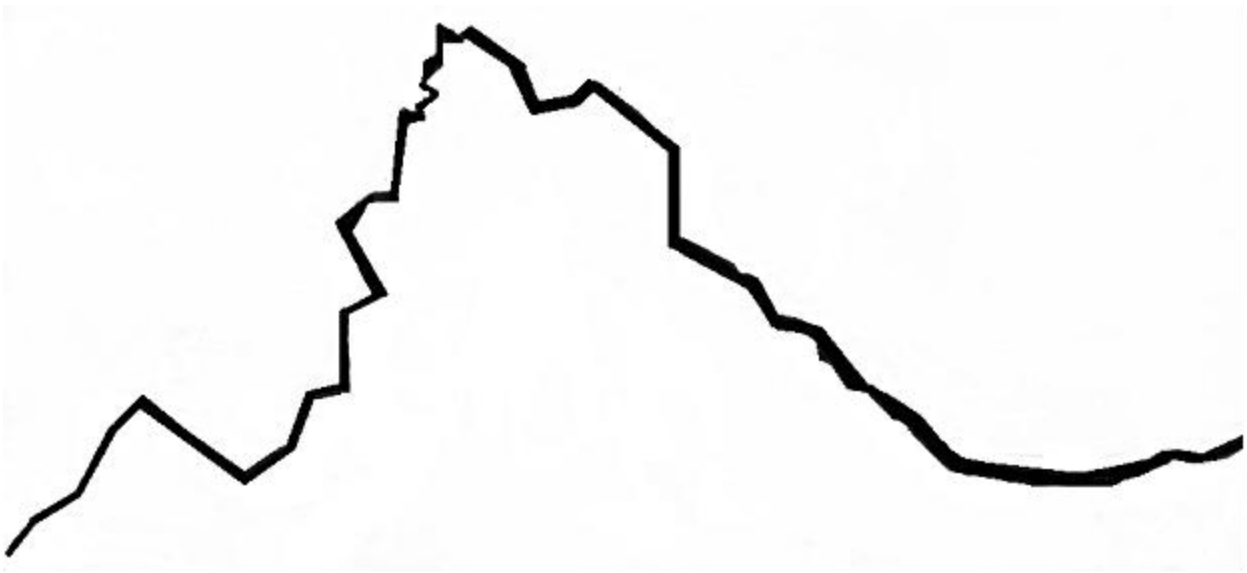

Figure 4.16 Fracture profile of Haynes 282 at 25 °C.

Figure 4.17 Fracture profile of Haynes 282 at 600 °C.

$$\frac{da}{dN} \propto Q\frac{\Delta K^2}{\sigma_{cy}E} \quad \text{.....(4.4)}$$

Therefore, a fall in the yield strength and/or modulus of elasticity of a material would result in an increase in the FCG rate. However, homogenization of slip and its effect on the fracture mode, and environmental interactions produce larger increases in the FCG rate than the $\Delta\delta$ approach would indicate [32]. Hence, it is useful to plot FCG rates against $\Delta K/(\sigma_y/E)^{1/2}$ to remove effects simply caused by changes in σ_y and *E* with temperature; that way it will provide an indication as to the degree of influence of other factors, such as changes in fracture mechanism and environmental interactions.

Figures 4.18 to 4.21 are plots of *da/dN* vs. $\Delta K/(\sigma_y/E)^{1/2}$ for Haynes 282 at two temperatures (25°C and 600°C), two frequencies (0.05 Hz and 15 Hz), and two stress ratios (0.1 and 0.7). In comparing Figures 4.11 with 4.18, 4.12 with 4.19, 4.13 with 4.20, and 4.14 with 4.21, it is observed that aside from Figures 4.12 and 4.19, there is a significant change in the FCG rate between 25˚C and 600˚C. Hence, this indicates that besides a drop in the yield strength and modulus of elasticity of the material, other factors are responsible for the increase in crack growth with increasing temperature.

As observed in this work, there are instances where the FCG rate decreases with an increase in temperature. This phenomenon has been reported to be due to oxide induced crack closure [58], and/or dynamic strain ageing [57]. With regards to oxide induced crack closure, it is probable that an increased volume oxides produced at a higher temperature of 600°C wedge the crack open. Hence, the effective stress intensity range is reduced, which leads to a decrease in the rate of FCG. Moreover, oxide induced crack closure and dynamic strain ageing are both time dependent

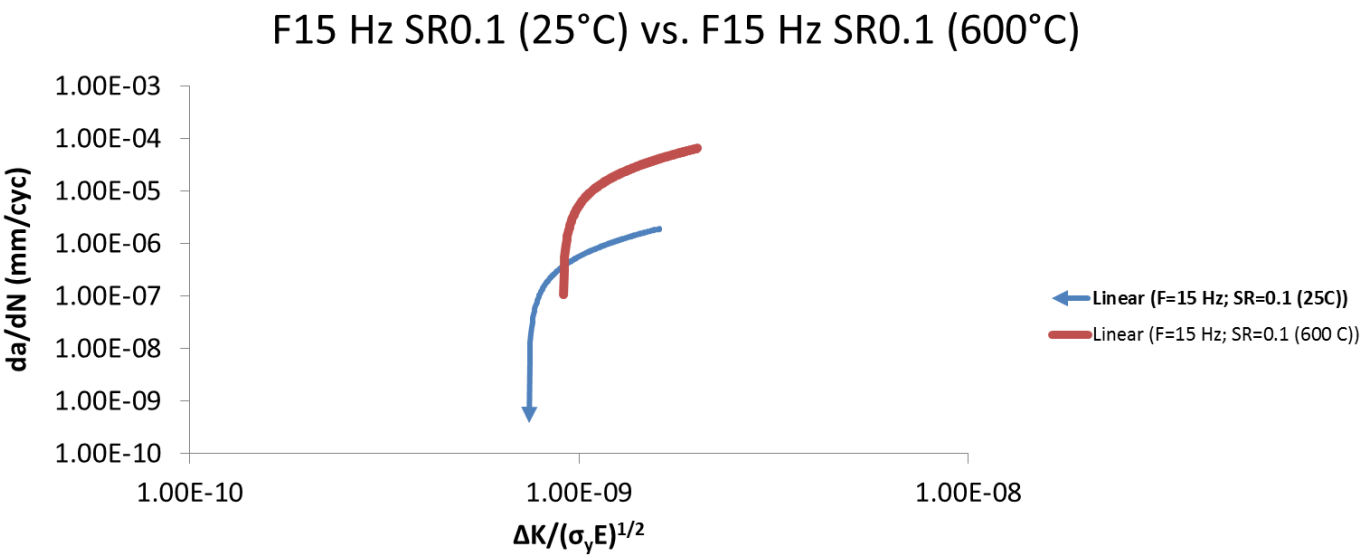

Figure 4.18 Effect of temperature on fatigue crack growth rate of Haynes 282 at a frequency of 15Hz and stress ratio of 0.1 (normalised stress intensity range).

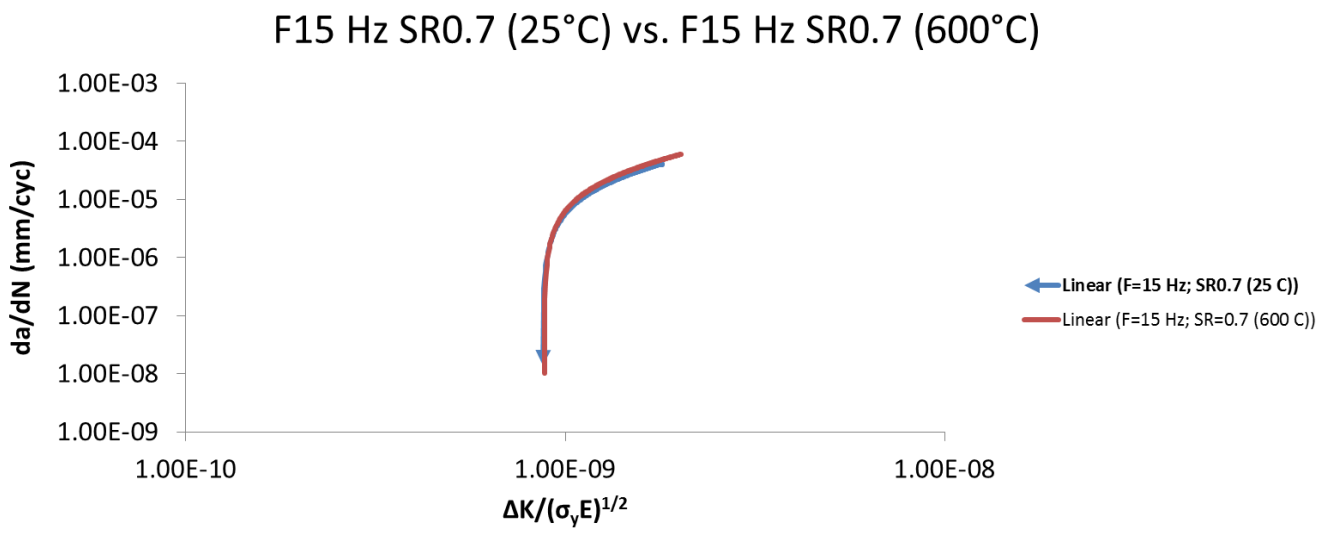

Figure 4.19 Effect of temperature on fatigue crack growth rate of Haynes 282 at a frequency of 15Hz and stress ratio of 0.7 (normalised stress intensity range).

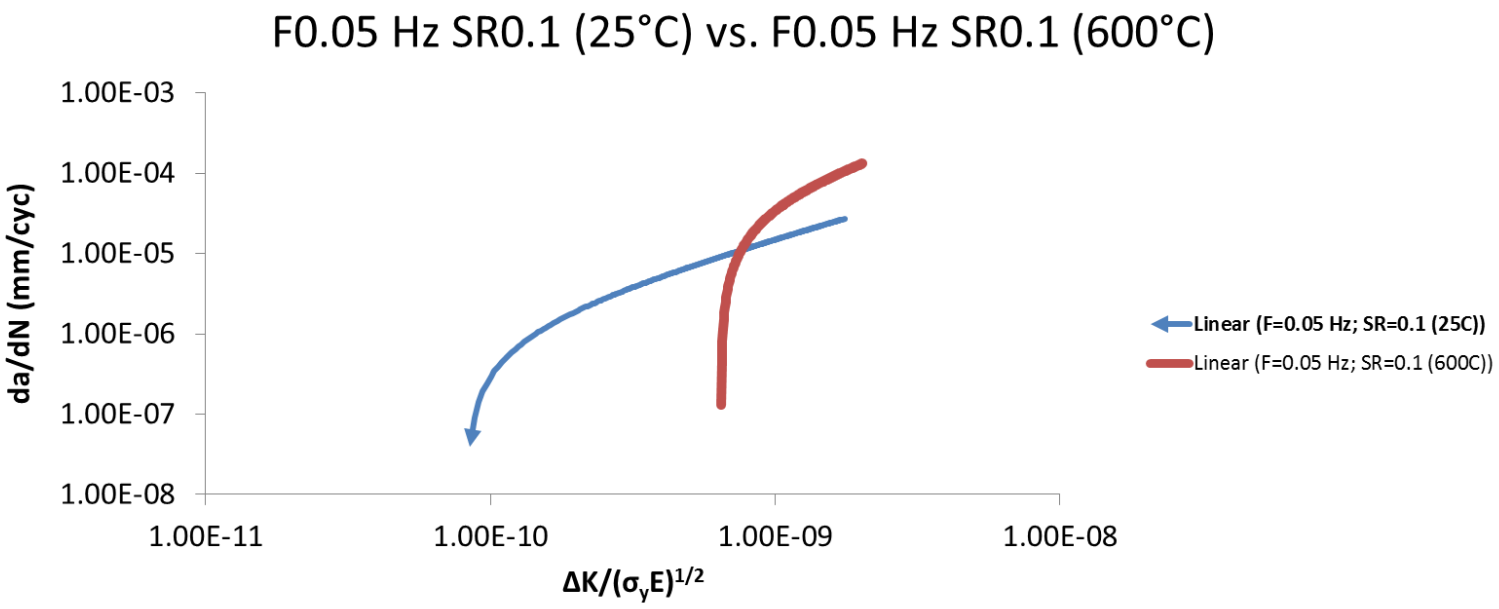

Figure 4.20 Effect of temperature on fatigue crack growth rate of Haynes 282 at a frequency of 0.05Hz and stress ratio of 0.1 (normalised stress intensity range).

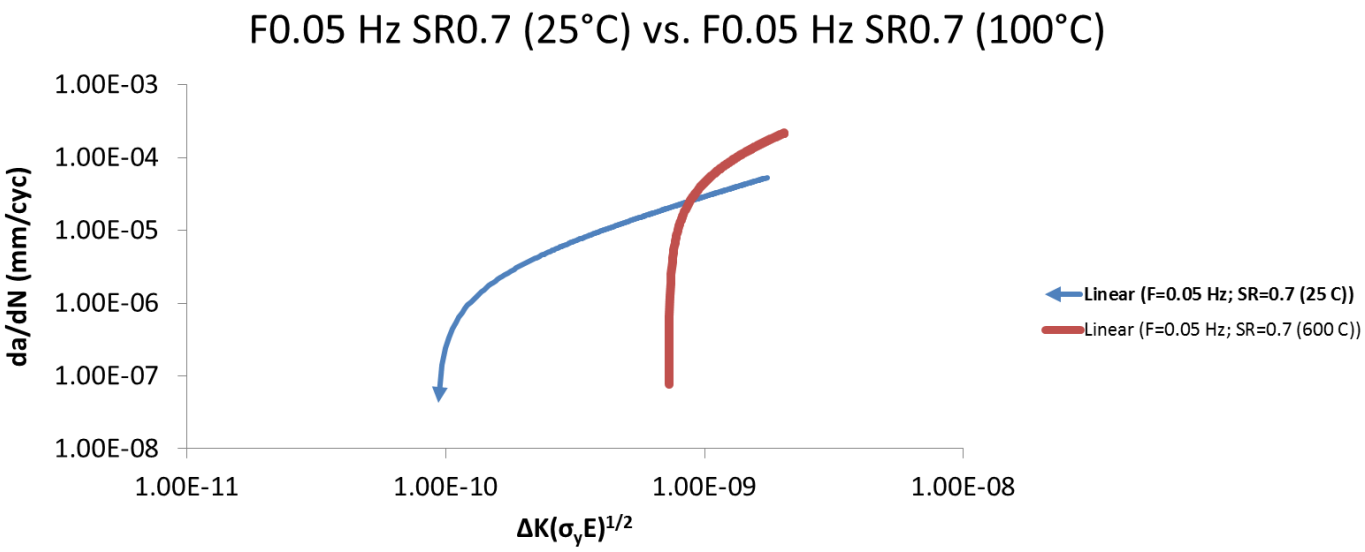

Figure 4.21 Effect of temperature on fatigue crack growth rate of Haynes 282 at a frequency of 0.05Hz and stress ratio of 0.7 (normalised stress intensity range).

phenomena and therefore likely to be most significant near the threshold [32], as shown in Figures 4.13 and 4.14, where the crack is growing very slowly. Furthermore, in comparison with 15 Hz, the crack tip velocity at 0.05 Hz is relatively slower. Hence, the effects of the time dependent phenomena (i.e. oxide induced crack closure and dynamic strain ageing) will be more pronounced at 0.05 Hz; as illustrated in a comparison of Figures 4.11 with 4.13, and 4.12 with 4.14.

4.5 Effect of Welding on Microstructure of Haynes 282

4.5.1 General Microstructure of Laser Weld Region

As observed in a previous work [9], cracks are formed in the laser beam weld region of Haynes 282. These cracks are confined to the HAZ region; there were no cracks in the FZ.

Detailed analyses of the FZ and HAZ are presented and discussed in the following sections.

4.5.2 Weld Fusion Zone Microstructure

As observed in a previous work [9], the FZ consists of a cellular dendritic microstructure formed by epitaxial growth from the fusion boundary. Furthermore, the FZ has been shown [9] to consist of ɣ dendrites and solidification products along the interdendritic regions with very large primary MC carbides that managed to thrive above liquidus temperature without melting. These carbides that were able to survive are small in number, and easily distinguishable from solidification microconstituents.

As observed in a previous work [9] the HAZ around laser beam welds that were made after pre-weld heat treatment are susceptible to intergranular cracking of varying degrees. A majority of the cracks occurred in the neck region of the keyhole shaped weld, in HAZs that are slightly away from the FZ. The fracture paths of these cracks have an irregular zigzag morphology and are closely associated with widened grain boundaries. These features are typical characteristics of intergranular liquation cracking [105-106]. The PMZ adjacent to the weld fusion line constitutes the HAZ of a weldment, and within this region, the degree of melting that takes place ranges from 0% to 100%. It has been observed from previous work on the weld HAZ in fully austenitic Fe and nickel-base superalloys, that the HAZ becomes highly susceptible to liquation cracking if it experiences a peak temperature below the solidus temperature [107]. Basically, HAZ cracks are the result of the formation and persistence of liquid films at the HAZ grain boundaries and the inability of the grain boundary liquid film to sustain thermal stresses and strains caused by the welding cycles.

4.5.3 Cause of Intergranular HAZ Liquation Cracking in Haynes Alloy 282

Generally, it is acknowledged that HAZ grain boundary liquation is caused by either non-equilibrium subsolidus melting or equilibrium super-solidus melting [77-78]. Even though supersolidus melting is expected to occur in all weldments due to heating above the equilibrium solidus temperature in certain regions, nevertheless, the subsolidus grain boundary is more insidious and detrimental. This is because it extends both the effective melting temperature range and the size of the crack susceptible region in the HAZ [80-81]. Furthermore, it is known that subsolidus melting influences the nature of melting at supersolidus temperatures by pre-

establishing local heterogeneities that are capable of altering the kinetics of reactions during subsequent heating [80].

Usually, the origin of liquid on HAZ grain boundaries below the bulk solidus of the alloy is explained by using two mechanisms; namely, grain boundary penetration and grain boundary segregation [9]. The former involves a phenomenon known as constitutional liquation of grain boundary second phase particles and the subsequent wetting of the grain boundaries with liquid produced from the liquation process, and/or the interaction of a migrating HAZ grain boundary with liquating particles within the matrix. When the liquid penetrates the grain boundary at the particle/matrix, it pins the boundary or slows down its rate of migration, thus, enabling uniform wetting by the liquid. On the other hand, the latter involves the segregation of surface-active elements and/or low melting point depressants (LMPDs), such as B, S and P during casting, thermo-mechanical processing and pre-weld heat treatment [9].

4.5.3.1 Constitutional Liquation Theory

Pepe and Salvage in 1967 first proposed and explained the theory of constitutional liquation. From experiments that were conducted, they observed and reported liquation of titanium sulphide particles in 18-Ni maraging steel [108]. The theory was illustrated by using a hypothetical binary alloy system as shown in Figure 4.22. An alloy of nominal composition *Co* that consists of an α solid solution matrix and high melting point intermetallic particles of AxBy dispersed as second phase particles within the matrix exhibits a different behaviour when initially heated at an infinitely slow rate, and then at an extremely fast rate from temperatures T_1 to T_4. Under equilibrium conditions that correspond to an infinitely slow heating rate, the solubility of *'B'* in an α-matrix increases until the temperature reaches T_2, where the last remaining AxBy particles dissolve, thus

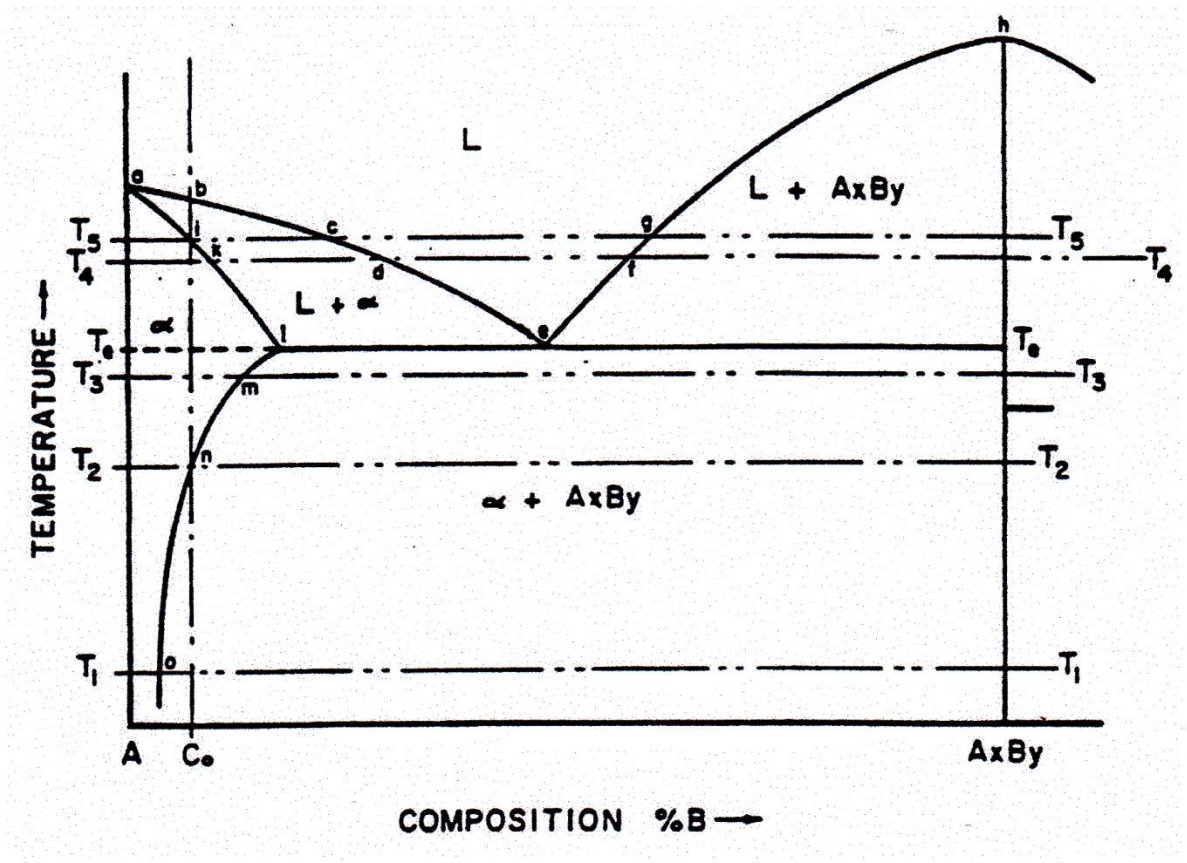

Figure 4.22 Schematic diagram of a portion of hypothetical phase diagram for an alloy system exhibiting constitutional liquation [105].

Source – Effect of Constitutional Liquation in 18-Ni maraging steel weldment by J.J Pepe and W.F. Savage (1967). Reprinted with permission from Welding Journal (15th December, 2014).

converting the alloy to a homogenous single phase solid solution of composition *Co*. Thereafter, continuous heating from T_2 (where complete dissolution of AxBy particles occurs) to a temperature just below T_5 or at T_4 results in no phase changes. At the equilibrium solidus temperature, T_5, the first infinitesimal amount of liquid of the composition that corresponds to point '*c*' is formed. In essence, under equilibrium heating conditions (extremely slow heating) second phase intermetallic particles with a composition within the solubility limit of the alloy can dissolve by diffusional processes before they have the opportunity to react with the α matrix. The behaviour of intermetallic particles AxBy under a non-equilibrium fast heating rate, such as that experienced during welding significantly differs from the above description.

For a precipitate phase to disappear and/or transform into a solid solution upon heating, it must first dissociate, then, followed by the subsequent accommodation of excess components of the precipitate phase, liberated as additional solute within the surrounding matrix. The rate at which the excess solute of a precipitate phase will vanish will be finite because dissolution and accommodation are temperature dependent processes. Furthermore, with an increase in the heating rate, a critical heating rate will be attained above which the dissolution of the precipitate phase will be incomplete during the interval required to raise the temperature to the equilibrium solidus. An assumed spherical particle is used to represent precipitate phase AxBy for illustration purposes and clarity of the dissolution process. Figure 4.23 schematically shows the changes in the concentration gradient within the surroundings of the particle during heating to temperatures of T_3, T_e, and T_4, respectively. The equilibrium structure of AxBy as a function of temperature is represented by the vertical line that emanates from the composition *Co* in Figure 4.22. In essence, any departure from this equilibrium structure due to rapid heating results in the redistribution of solute since the system would be striving to maintain equilibrium. During non-equilibrium heating

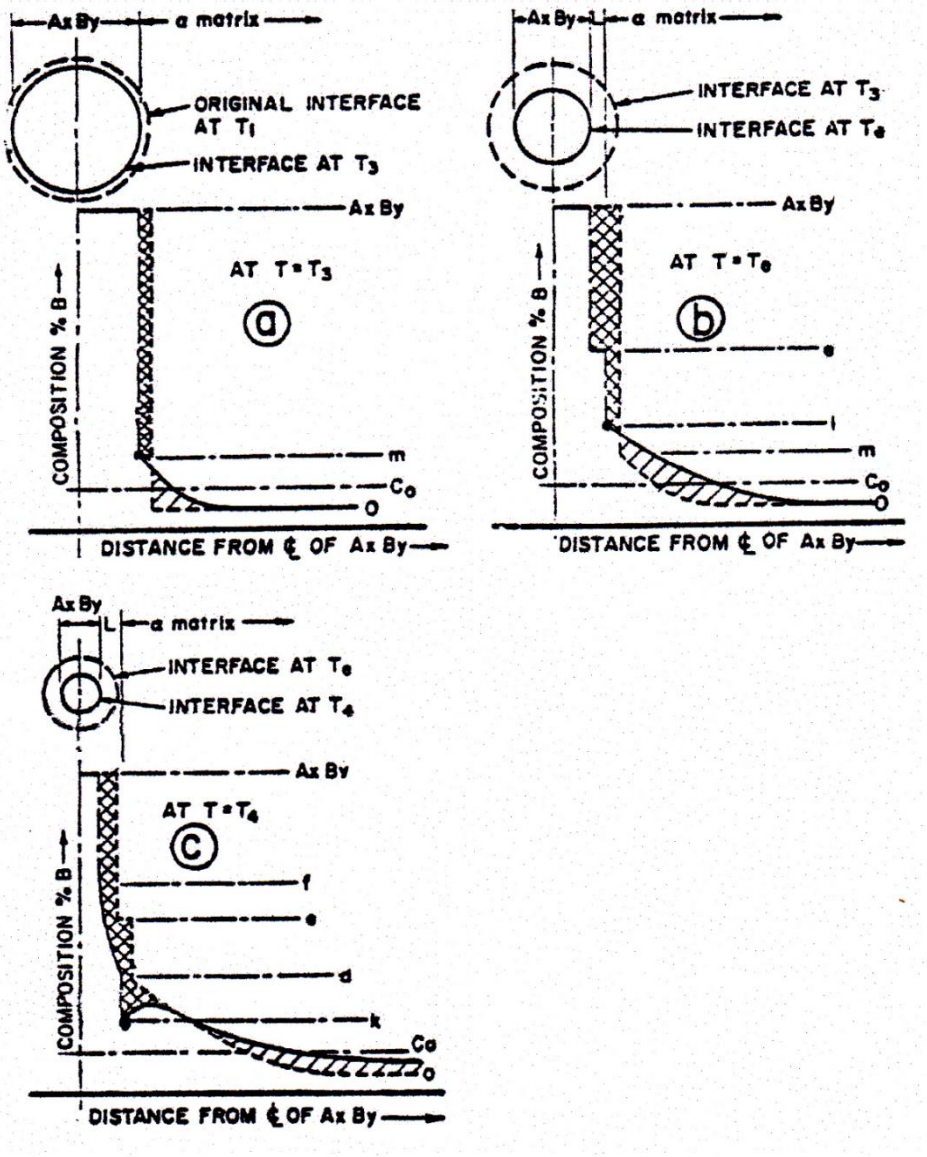

Figure 4.23 Schematic diagram of the concentration gradients at various temperatures during formation of constitutional liquation [105].

Source – Effect of Constitutional Liquation in 18-Ni maraging steel weldment by J.J Pepe and W.F. Savage (1967). Reprinted with permission from Welding Journal (15th December, 2014).

to T_3, the AxBy particles begin to dissolve since they are unstable with respect to the α matrix at this solute; atoms '*B*' released from the AxBy particles should diffuse into the adjacent α matrix. Nevertheless, as illustrated in Figure 4.22, the particles must be in contact with the α phase of composition '*m*' for the two phases to co-exist. Thus a concentration gradient is set up in the α matrix with a maximum of '*m*' at the AxBy interface and decreases towards the original matrix composition '*o*' further away into the α phase. In order that material balance will be sustained, the area of the double cross-hatched region in Figure 4.23a must be equal to the area of the single cross hatched-region. The concentration gradient slope produced in this way would depend on the following:

1. the heating rate – a faster heating rate produces steeper concentration gradients,
2. the diffusivity of the solute – faster diffusivity of solute atoms '*B*' means shallower concentration gradients, and
3. accommodation factor – the ease that solute atoms are accommodated within the α-matrix is related to the shallowness of the concentration gradient.

As shown in Figure 4.23b, as heating continues, the temperature increase from T_3 to T_e leads to further dissociation and decrease in the size of the AxBy particles, where the dashed and solid circles represent the location of the AxBy interface at T_3 and T_e, respectively. At the eutectic temperature, T_e, the composition that corresponds to point '*e*' permits the formation of a single phase liquid at the AxBy interface, hence, the undissolved portion of the AxBy particles is surrounded by a liquid of composition '*e*', which in turn, is surrounded by the α matrix. Figure 4.23b also shows the distribution of solute atom '*B*' in the three phases that coexist at *Te*. Upon further heating to T_4, additional time is allowed for the dissolution of the AxBy particles and the expected solute distribution is represented by a solid line in Figure 4.23c.

As heating transpires above *Te*, the equilibrium solubility of the α phase reduces along the solidus line 'akl'. Furthermore, as the temperature rises above T_e through to T_4, the concentrations of the solid solution and the liquid film in contact with one another correspond to '*k*' and '*d*', respectively (Figure 4-22). This readjustment in composition leads to the creation of an inverted region in the concentration gradient similar to that shown in Figure 4.23c. The excess solute in the α phase would cause the α/liquid interface to epitaxially move into the α matrix until the excess solute is consumed by a forming liquid of composition '*d*'. Therefore, each particle of AxBy which remains undissolved at T_4 is surrounded by a liquid film of variable composition that ranges from '*f*' at the AxBy interface to '*d*' at the matrix interface. Hence, it is possible to have localized melting under non-equilibrium heating rates at temperatures below the equilibrium solidus temperature T_5. This phenomenon, which is possible anywhere above *Te*, is referred to as 'constitutional liquation'. In essence, constitutional liquation can occur anytime an intermetallic compound and the surrounding matrix phase react to form a low melting liquid phase, provided that the heating rate is rapid enough to preclude complete dissolution of the compounds prior to reaching the minimum liquidus temperature.

Nevertheless, as shown in Figure 4.22, an exception is possible provided that the initial composition of the alloy is above the solubility limit point '*I*'. At this point, the occurrence of eutectic type melting at the AxBy/α interface would be independent of the heating rate as AxBy would be thermodynamically stable up to the eutectic temperature T_e upon which it can form a liquid of composition '*e*' [28]. Figures 4.24a to 4.24c show the changes in solute redistribution that occur in a material which exhibits constitutional liquation when rapidly heated to temperature T_4 and then isothermally held for varying lengths of time. During holding, solute atoms '*B*' would diffuse from the liquid into the α-matrix which causes a gradual decrease in the width of the liquid

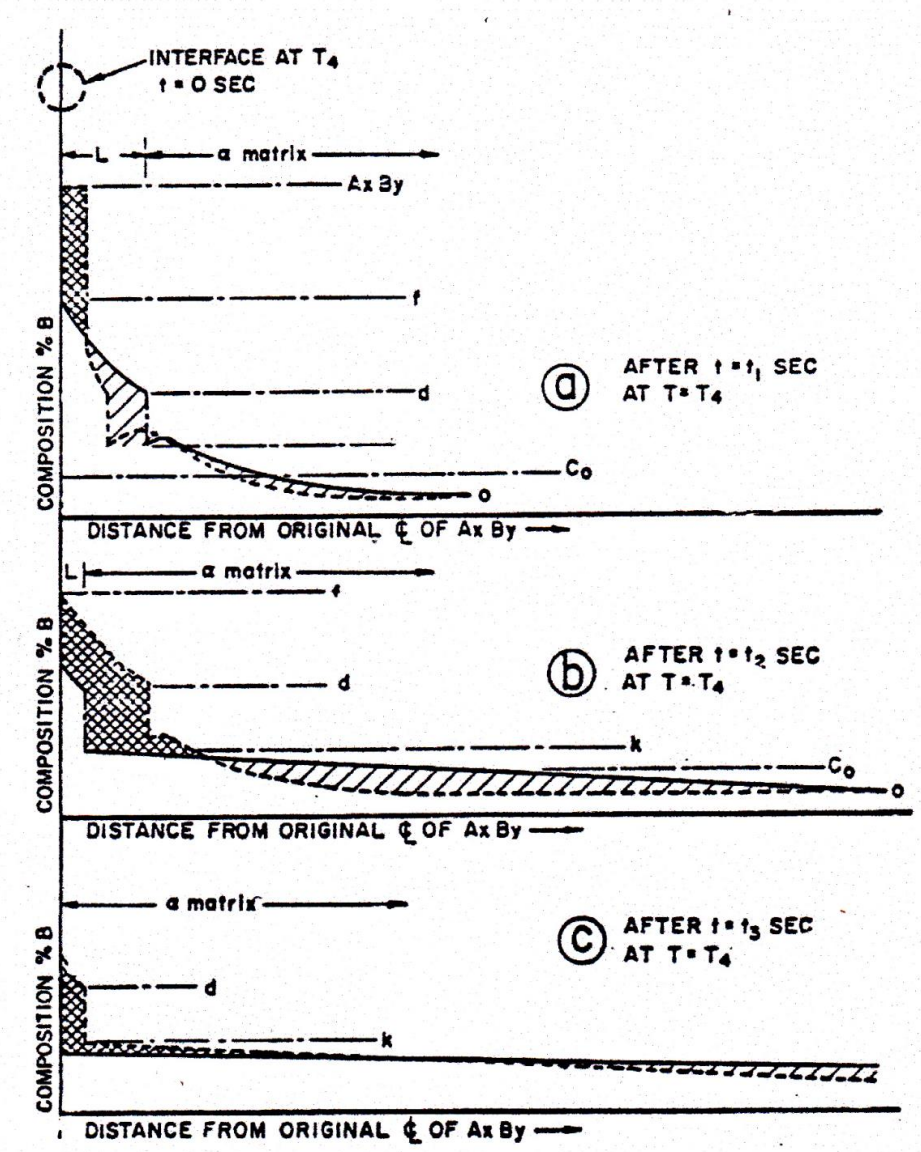

Figure 4.24 Schematic diagram of the effect of holding time on the stability of liquid film produced by constitutional liquation [105].

Source – Effect of Constitutional Liquation in 18-Ni maraging steel weldment by J.J Pepe and W.F. Savage (1967). Reprinted with permission from Welding Journal (15th December, 2014).

phase. Eventually, nearly complete homogenization would occur, thereby permitting the liquid to completely solidify. After the solidification of the liquid, the composition gradient of solute atoms '*B*' in the α-matrix reaches a maximum that corresponds to composition '*k*' (the maximum solubility of '*B*' atoms in the α phase at T_4) at the original centerline of AxBy and decreases towards the composition that corresponds to point '*O*' at the interior of the α-matrix. In essence, the liquid produced by constitutional liquation should experience a gradual modification in composition once the AxBy phase is completely dissolved and should ultimately disappear by solidification if subjected to a sufficiently long enough isothermal hold at any temperature below the equilibrium solidus. Another notable influence on the occurrence of constitutional liquation in alloys is the solid-state dissolution behaviour of their second phase precipitates. Due to the ease by which interstitial compounds, like Fe_3C, dissolve and the rapid diffusion of their solute atoms '*C*' make constitutional liquation less feasible. However, there is an exception where it involves an extremely rapid heating/cooling rate as verified (625°C/s for <2 μm Fe_3C) by Aronson [108]. In contrast, less readily dissolvable alloy carbides/intermetallic compounds with substitutional type solute are readily more susceptible to liquation except for conditions where the heating rate during welding is extremely slow.

4.5.3.2 Grain Boundary Segregation

The segregation of surface active elements, most of which are also melting point depressant elements, to the grain boundaries prior to welding is another mechanism that can result in liquation cracking along boundaries. The segregants reduce the liquating temperature of the boundaries relative to the surrounding matrix and results in preferential non-equilibrium subsolidus melting of the HAZ segregate region during the weld thermal cycle and subjects the boundary to liquation

cracking. In alloys where it is unlikely that constitutional liquation can occur, due to the absence of constituent particles/phases, the segregation mechanism has been employed in the explanation of the onset of grain boundary liquation [109].

The diffusion of solutes or impurity elements to loosely packed or disordered regions such as the grain boundary, serves as the metallurgical basis for preferential grain boundary segregation. Other loosely packed regions include: free surfaces, particle/matrix interfaces, stacking faults and phase boundaries. The solubility of a given element in a given matrix phase influences the propensity for segregation to grain boundaries. The extent to which segregation will occur can be quantified by using a grain boundary enrichment factor (β_b), defined as:

$$\beta_b = C_b/C_o \quad \text{.....(4.5)}$$

where C_b = the equilibrium concentration of the element at the boundary

C_o = the equilibrium concentration in the matrix

Higher values of β_b mean higher tendency of the solutes or impurity elements to segregate to the boundaries. The enrichment of grain boundaries by solutes/impurity atoms prior to welding is a diffusion-controlled process and can occur by either equilibrium [110-112] or non-equilibrium segregation [113-115]. Equilibrium grain boundary segregation takes place when a material or alloy is isothermally held at a sufficiently high temperature to allow for appreciable diffusion of the solute or impurity atoms from the bulk matrix to the grain boundary where it is absorbed to decrease the interfacial free energy and the segregated structure, thus forming a stable equilibrium condition. Here, the driving force for equilibrium segregation of solute elements in a material

stems from the need to better satisfy atomic bonding requirements in the disordered structure of the interface and reduce the high free energy of the interface to the barest minimum.

A decrease in the temperature of the isothermal treatment and an increase in the initial solute concentration in the matrix cause an increase in the magnitude of equilibrium segregation. As the temperature increases, the vibrational amplitude of the lattice atoms increases such that the driving force for solute atom migration from the grains to the interfaces is reduced, and also, the degree of equilibrium segregation. At lower annealing temperatures, the propensity for segregating atoms to diffuse to grain boundaries is high, but energetically difficult. As a result, the rate of segregation progressively decreases beyond the initial increase which accompanies the reduction in temperature. Hence, an optimum temperature exists at which the highest degree of equilibrium segregation occurs. One feature that is unique to equilibrium segregation is that the segregated solute atoms are generally restricted to a few atomic layers because of limitations of the structural perturbation of the grain boundaries that do not extend beyond a few atom distances. Typically, the total amount of segregation is usually in the order of a few monolayers. In addition, equilibrium segregation is a completely reversible process and hence, the chemical enrichment at the grain boundaries and other interfaces can be reproduced by re-establishing identical physiochemical conditions [111].

Westbrook and Aust, and their colleagues [113-115] first defined the phenomenon of non-equilibrium segregation when the concept of equilibrium segregation was not adequate in explaining an unusual grain boundary hardening phenomenon. A mechanism was suggested in which the effect was accounted for by the abnormal generation and/or motion of some type of defect in the vicinity of the grain boundary which also required the presence of solute atoms [116]. Later, a solute-clustering model was proposed based on preferential solute-vacancy interactions

and non-ideal thermodynamic behaviours of the binary system which is summarized as follows. In addition to the equilibrium vacancy concentration generated and distributed at the annealing temperature during thermal treatment, some vacancy-solute complexes can also form as a result of positive binding energy between the solute atom and vacancy [117]. As a result, migration/diffusion is energetically favored when the diffusion coefficient of the solute-vacancy complex exceeds that of the vacancies alone. Therefore, when materials are quenched from a high temperature annealing process, the equilibrium vacancy concentration, which is initially very high, falls and vacancy flows to interfaces such as grain boundaries where they can be readily annihilated.

The annihilation of vacancies at the grain boundaries generates a concentration gradient of complexes, which drives the complexes (those with positive solute-vacancy binding energy) to diffuse from within the grain to the grain boundary regions where the vacancies are annihilated and the solute atoms occupy grain boundary positions. Eventually, this would lead to the creation of an excessive concentration of solute atoms (segregant) at and within the vicinity of grain boundaries. The effective uphill diffusion of solute atoms, which produces a solute-rich boundary region, is thermodynamically driven by the reduction in free energy associated with the annihilation of excess vacancies at the boundary sink. Consequently, non-equilibrium segregation is generally considered from the concept of the formation of atom-vacancy complexes within the lattices of a polycrystalline material/alloy, and the presence of a gradient in the concentration of complexes between the grain interior and the grain boundaries. This type of segregation occurs during cooling from thermal treatment or annealing that follows plastic deformation [117]. Besides factors such as the starting temperature, bulk concentration of solutes, binding energy between the solute atoms and vacancies, the extent of segregation is highly sensitive to the cooling rate [117].

Due to the fact an increase in the peak annealing temperature increases the equilibrium concentration of vacancies as well as the tendency for segregation, insufficient time for the diffusion of solute-vacancy complexes into grain boundaries, which is a consequence of rapid cooling rates, will cause a drastic reduction in the extent of segregation.

On the contrary, if the cooling rate is very slow, and causes a gradient in the concentration of solute atoms between the grain boundary and the grain interior, the segregated solute atoms may diffuse back into the grain interiors, hence eliminating segregation [118]. In essence, intermediate cooling rates favor non-equilibrium segregations. For complex alloys, such as ternary system alloys, different solutes may interact at the grain boundaries and the synergetic effects can increase or reduce segregation. Guttmann [119] proposed that the free energy of segregation of one species may be increased by the second if the interaction between the two species are negative, that is, attractive. Depending on the peak temperature that is experienced by the materials and the diffusion time that is available, it is possible for grain boundary segregation to occur during welding [120]. To account for this, various mechanisms have been proposed, some of which include:

1. grain boundary sweeping of solute atoms during grain growth due to their lower energy relative to the matrix,
2. pipeline diffusion of solute atoms along grain boundaries that are continuous from the FZ to PMZ, which provides conduits for elemental segregation and enrichment of the HAZ grain boundaries, because diffusion along grain boundaries is of a higher order of magnitude than in the bulk matrix [121], and
3. Gibbsian segregation which rationalizes segregation to a static HAZ grain boundary, in that equilibrium diffusion is achieved by the diffusion of low energy solute atoms into the

segregated region of the matrix localized within a few atom diameters on either side of the high energy grain boundary [111].

Nevertheless, pre-weld thermal treatment is known to be the main source of the segregation of surface active and LMPD elements in welded components. A significant amount of work has been carried out by researchers on the role that grain boundary segregation mechanisms plays with regards to facilitating HAZ liquation cracking. Both equilibrium and non-equilibrium were found to increase the liquid wettability of grain boundaries. The presence of LMPD elements or impurity solute atoms in the grain boundary liquid reduces the solidification range of the liquid and contributes to HAZ microfissuring. Segregation of B [122-123], P, C [124] and S [125] in wrought and cast Inconel 718 has been extensively investigated. It was observed from the findings B segregation to the grain boundaries either by equilibrium and/or non-equilibrium modes influences the on-heating and on-cooling hot ductility values. S, like B, also increases the solidification temperature range by increasing the nil-ductility range on cooling. In another study, it was found out that the elemental segregation of B and the associated grain boundary liquation are dependent on both the grain size and the character of the grain boundary [126-127]. High angle grain boundaries have more segregation intensity and are most susceptible to liquation. Variations in the intensity of B segregation with grain size and increase in the initial B concentration have also been confirmed with susceptibility to HAZ liquation cracking in IN 718 Plus superalloy [128-129].

The grain boundary liquation features observed in the present work suggest that HAZ liquation involves significant subsolidus liquation. The occurrence of subsolidus liquation in Haynes 282 can be verified in a number of ways. One way is to use a Gleeble thermo-mechanical simulation system to physically simulate the HAZ microstructure. This was performed in a previous research [9], where Haynes 282 alloy specimens were rapidly heated by the Gleeble system to peak

temperatures below the equilibrium solidus temperature of the alloy (which is ~1244°C), from 1050°C to 1200°C, to evaluate the response of the alloy to rapid welding thermal cycles.

As observed in a previous work [9], the microstructural examination of the Gleeble specimens simulated at peak temperatures up to 1120°C showed that the second phase precipitates along the grain boundaries in the alloy remain largely unaffected by the Gleeble simulation thermal cycle. However, in specimens rapidly heated to 1150°C and 1170°C and held for 1 second, complete dissolution of the intergranular particles occurred and the widening of the grain boundary regions was observed. An increase of the holding time at the peak temperatures to 3 seconds resulted in reduction in the occurrence of widened grain boundaries. This behaviour is consistent with grain boundary liquation caused by the constitutional liquation of second phase particles [105].

It is known that a major consequence of intergranular liquation in nickel-base superalloys is poor hot ductility under tensile loading. Hence, to further confirm the occurrence of liquation on widened grain boundaries observed at 1150°C and 1170°C, the hot ductility of the alloy was evaluated by subjecting Gleeble specimens to tensile loading; first, after holding for 0.1 seconds at various peak temperatures. As observed in the previous work [9] the alloy initially exhibited high hot ductility, but the ductility dropped to a significantly low level at 1150°C and approached zero at around 1170°C. As stated earlier, widened grain boundaries have been observed at peak temperatures of 1150°C and 1170°C, at which the alloy exhibits poor ductility. On increasing the holding time from 0.1 to 3 seconds during the hot ductility test at 1170°C, an improvement in ductility from 3% to 26% was notably observed. The increase in ductility with holding time correlates with the observed reduction in the thickness of widened grain boundaries with increase in holding time, which can be attributed to the re-solidification of intergranular metastable liquid, since the liquid phase reduces hot ductility [105].

An alternative way of verifying grain boundary liquation is thorough a fractography study of the crack surfaces [130-132]. A SEM study of the fractured surface of Gleeble hot ductility specimens performed in a previous study [9], confirmed brittle intergranular failure in specimens tested at 1150°C and 1170°C with 0.1 second of holding time, which correlates with the loss of ductility observed at these temperatures. A higher magnification examination of the grain surfaces revealed regular roundish surface features all over the grain facets, which have been reported to be an indication of re-solidified intergranular liquid phase [130]. As observed in a previous work [9], the fractured surface of a hot ductility test specimen tested at 1120°C exhibited high ductility. The specimen exhibited a ductile transgranular failure mode in contrast to the brittle intergranular fracture observed in the specimens tested at 1150°C and 1170°C.

Hence, degradation of the ability of Haynes alloy 282 to accommodate welding stresses, due to the embrittling effect of intergranular liquation caused by liquation of second phase precipitates, is a major contributory factor to the susceptibility of the material to HAZ cracking during laser welding. Consistent with the reported liquation behaviour of the carbides in nickel-base superalloys [133], a careful analysis of the Gleeble simulated specimens did not show any evidence of constitutional liquation of MC carbides at the peak temperatures of 1150°C and 1170°C.

Also, Owczarski et al. [134] in their study of the weldability of nickel base superalloys asserted that $M_{23}C_6$ particles would undergo a solid-state reaction well below the solidus temperature and would not constitutionally liquate during welding. Therefore, the likelihood exists that the subsolidus intergranular liquation observed at 1150°C and 1170°C is mainly caused by the constitutional liquation reaction of the M_5B_3 borides. In order to verify this possibility, Haynes alloy 282 specimens subjected to heat treatment at 1100°C which dissolve the $M_{23}C_6$ carbides and leave the M_5B_3 borides as the main intergranular precipitates were rapidly heated by the Gleeble

system to various peak temperatures, in a previous study [9]. The Gleeble simulation results indicated that grain boundary liquation still occurs at 1150°C and 1170°C, irrespective of the exclusion of the $M_{23}C_6$ carbides, which indicates that the constitutional liquation of the M_5B_3 borides is responsible for the subsolidus non-equilibrium liquation reaction.

4.5.4 Factors that aid HAZ Liquation Cracking in Haynes 282

It is widely acknowledged that even if liquation has occurred, this does not necessarily create a microstructure susceptible to intergranular liquation cracking. The liquid phase, must of necessity wet, infiltrate and spread the along grain boundary region in a continuous or semi-continuous fashion, thus substituting the solid-solid interfacial energy along the grain boundary with a weaker solid-liquid interfacial energy [77]. Ineffective wetting of the grain boundary regions by the liquid film will lead to liquid existing in isolated pockets which allows for substantial solid-solid intergranular contact. To a first approximation, the distribution of the intergranular liquid can be treated in accordance with the relationship proposed by Smith [135]:

$$\gamma_{gb} = 2\gamma_{SL} \mathrm{Cos}\,\theta \qquad (4.6)$$

where θ is the wetting angle, γ_{gb} is the grain boundary energy and γ_{SL} is the solid-liquid interface energy. From Equation 4.6, it can be seen that for a given grain boundary energy, lower solid-liquid interface energy produces lower wetting angle and more ease for such a liquid to wet and spread along the grain boundary. The presence of B atoms in the intergranular liquid produced by the liquation of the M_5B_3 borides could substantially aid the wetting behaviour of the liquid through the influence of the surface active B atoms in lowering the solid-liquid interface energy along the grain boundary. In an alternate and/or complementary case, as apparent from Equation

4.6, higher grain boundary energy means greater tendency for the grain boundary to be wetted and penetrated by liquid phase for a given solid-liquid interfacial energy.

EBSD analyses, in a previous research [9], of the grain boundary character revealed that most of the grain boundaries in the as-received and heat treated Haynes alloy 282 are more of a 'random' nature with a higher order of "Σ" values. Special boundaries are inherently of lower energy than random high angle grain boundaries. The fact that most of the grain boundaries in the Haynes alloy 282 are of the high energy type could be another factor that facilitates intergranular wetting and penetration by the liquid film in the alloy. Guo et al. [126] and Kokawa et al. [136] confirmed that liquid penetration at the grain boundary is the greatest at high angle boundaries and relatively insignificant at low angle boundaries.

Additionally, the metastable liquid produced by the constitutional liquation of intergranular second phase particles always reacts with the adjacent solid grains through back diffusion of solute atoms across the solid-liquid interface. In such instances, the solid-liquid interfacial energy at non-equilibrium is extremely low [137], which would cause the liquid to effectively wet the grain boundary and exhibit extensive penetration. A theoretical model developed for describing the penetration of the liquid phase along a grain boundary has also shown that grain boundary penetration requires an undersaturated solid [138]. This is essentially the situation prevalent in the subsolidus HAZs during non-equilibrium rapid heating and cooling of the welding operation. During the rapid heating cycle, decomposition of intergranular M_5B_3 borides can lead to the release of B atoms along the grain boundary regions.

Besides aiding grain boundary wetting, the boron released from M_5B_3 borides are a potent melting point depressing element in nickel alloys. The enrichment of intergranular regions with B atoms

can decrease the starting temperature for grain boundary liquation during heating and also reduce the terminal solidification temperature during cooling. Previous studies [139, 140] have shown that on-cooling hot ductility behaviour is dependent on the hot ductility behaviour during heating. Hence, on-heating ductility behaviour can be a good indicator of expected ductility behaviour during cooling. Any factor that decreases the on-heating ductility will decrease the ductility during cooling. For instance, any factor that decreases the on-heating zero ductility temperature will reduce the ductility recovery temperature (DRT) during cooling. DRT during cooling is generally lower than the zero ductility temperature during heating [139, 140].

Hence, in the present work, the grain boundary liquation which decreased the zero ductility temperature during heating would in effect increase the brittle temperature range and delay the ductility recovery of the HAZ during cooling, both of which would promote susceptibility to liquation cracking. Therefore, the subsolidus liquation reaction of the intergranular M_5B_3 borides constitutes a major factor that reduces the resistance of the newly developed Haynes alloy 282 to weld HAZ cracking.

4.5.5 Effect of Pre-weld Heat Treatments on HAZ Cracking of Haynes Alloy 282

Previous studies on the weldability of precipitation strengthened nickel-based superalloys have shown that carefully designed pre-weld microstructural modification through thermal treatments can be useful in decreasing the problem of susceptibility to HAZ hot cracking [141-143]. For instance, Thompson et al. [143] reported that weldability is favourably affected by solution annealing and adversely by aging in the IN 718 alloy. It has also been reported that IN 718 and IN 718Plus specimens that were subjected to a high temperature solution heat treatment (1050°C – 1150°C) are most susceptible to HAZ hot cracking [128-129]. In Udimet 700 [80] and IN 738

alloy [144], appreciable improvement in resistance to weld cracking was achieved by an overaging treatment as compared to welding in standard solution heat treatment conditions. The improvement in the resistance to weld cracking by the overaging treatment was attributed to the minimized effect of stresses and strains that accompany rapid ɣ′ precipitation. Overaging by coarsening of the ɣ′ phase prior to welding decreases alloy hardness, which consequently increases its capability to relax part of the welding stresses and strains generated upon cooling. Overaging treatment of Haynes alloy 282 specimens before welding, however, resulted in more and extensive HAZ liquation cracking.

As discussed earlier in this thesis, the liquation of the M_5B_3 borides is found to be the major factor that causes HAZ cracking in the Haynes alloy 282. Hence, to minimize HAZ cracking, there is the need to select an appropriate pre-weld heat treatment that will eliminate or significantly reduce boride particles from the grain boundaries in Haynes 282. To achieve this objective, crack measurements of welded Haynes 282 in different pre-weld heat treatments conditions were performed. Two different modes of cooling (water quenching, and furnace cooling) were considered for the pre-weld heat treatments.

As shown in Figures 4.25 and 4.26, the results indicate that for both modes of cooling, HAZ cracking is reduced as the temperature is increased. In essence, the boride particles decrease as the temperature is increased. However, it can be observed that upon complete dissolution of the boride particles (at 1100°C for furnace cooling, and 1120°C for water cooling), a further increase in temperature leads to an increase in HAZ cracking. This is attributed to non-equilibrium segregation of the B atoms, released by the dissolution of the boride particles, to grain boundary regions during pre-weld heat treatments at 1100°C and above, the extent of which is expected to increase with temperature [9].

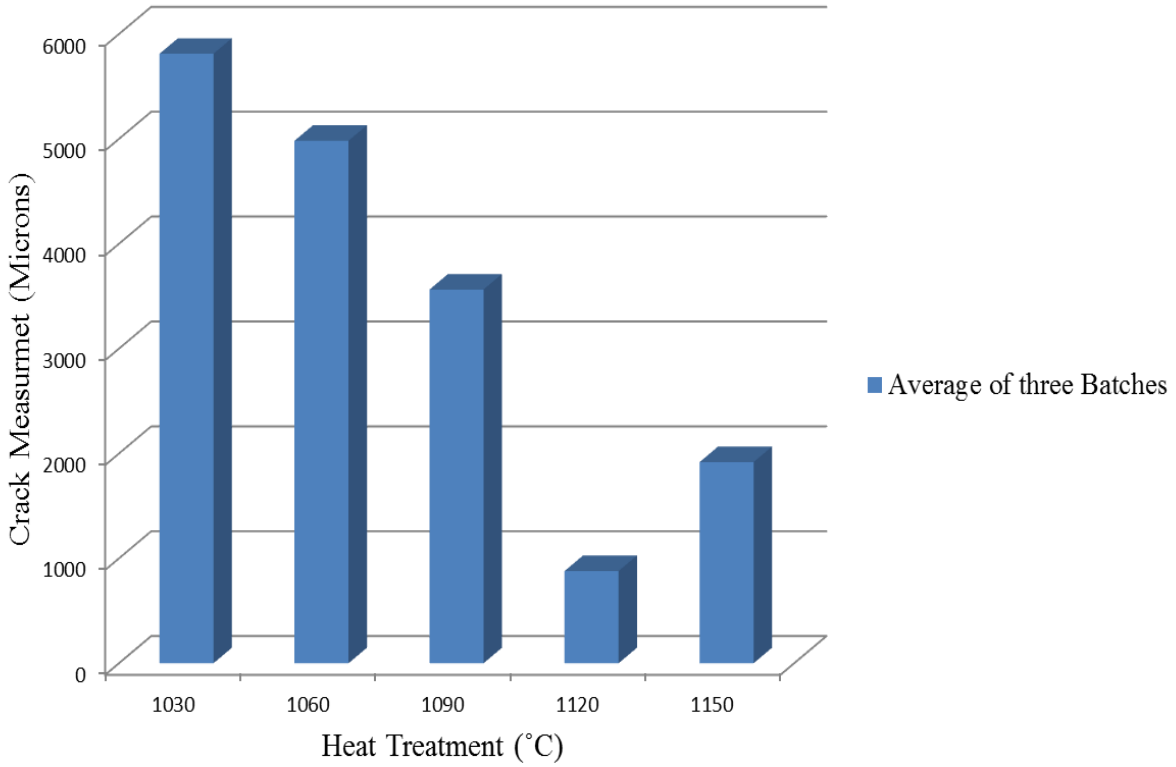

Figure 4.25 Crack measurement for water-quenched samples.

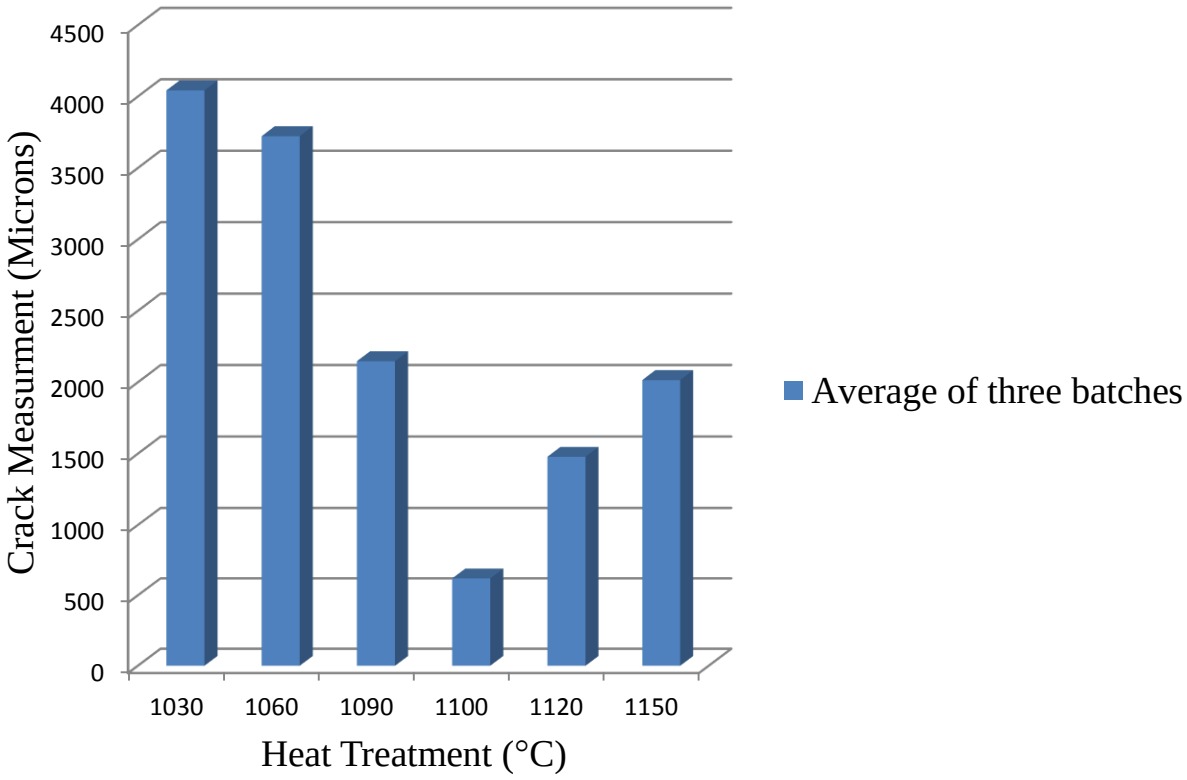

Figure 4.26 Crack measurement for furnace-cooled samples.

Based on the results of the crack measurements performed in this work, the optimum pre-weld heat treatment selected is 1100°C/2 hrs/furnace cooling. Although for both modes of cooling, an initial increase in temperature resulted in a decrease in the HAZ cracking, furnace cooling is preferred because it is industrially feasible.

4.6 Effect of Welding on Fatigue Crack Growth of Haynes 282

In practice, welded components that are put to service contain some tolerable level of cracking. Hence, it was paramount to find out whether the lowest level of cracking which was observed at 1100°C/ 2 h/furnace cooling is at a tolerable level. To obtain that information, FCG tests were performed on Haynes 282 before and after welding.

Figures 4.27 to 4.30 show plots of *da/dN* (crack growth rates) versus ΔK (stress intensity factor range) in Haynes 282 at 600°C, two frequencies (0.05 Hz and 15 Hz), and two stress ratios (0.1 and 0.7). Essentially, these plots show a comparison of the FCG rate of Haynes 282 before and after welding. Both the welded and unwelded samples were subjected to the same full heat treatment, Heat Treatment A, prior to fatigue testing. Table 3.3 shows the parameters of Heat Treatment A.

Typical of welded samples, there is some amount of scatter in the FCG plots. However, as can be observed, the FCG generally increases after welding. As shown in Figures 4.31 to 4.34, this trend is more discernible when a trendline (created by using MS EXCEL software) is applied to both data (before and after welding). Furthermore, this increase in the FCG rate of Haynes 282 after welding is numerically confirmed, in Table 4.2. Table 4.2 shows the Paris law constants (FCG exponent '*m*', and FCG coefficient '*C*') for Haynes 282 before and after welding, in the test conditions used in this work

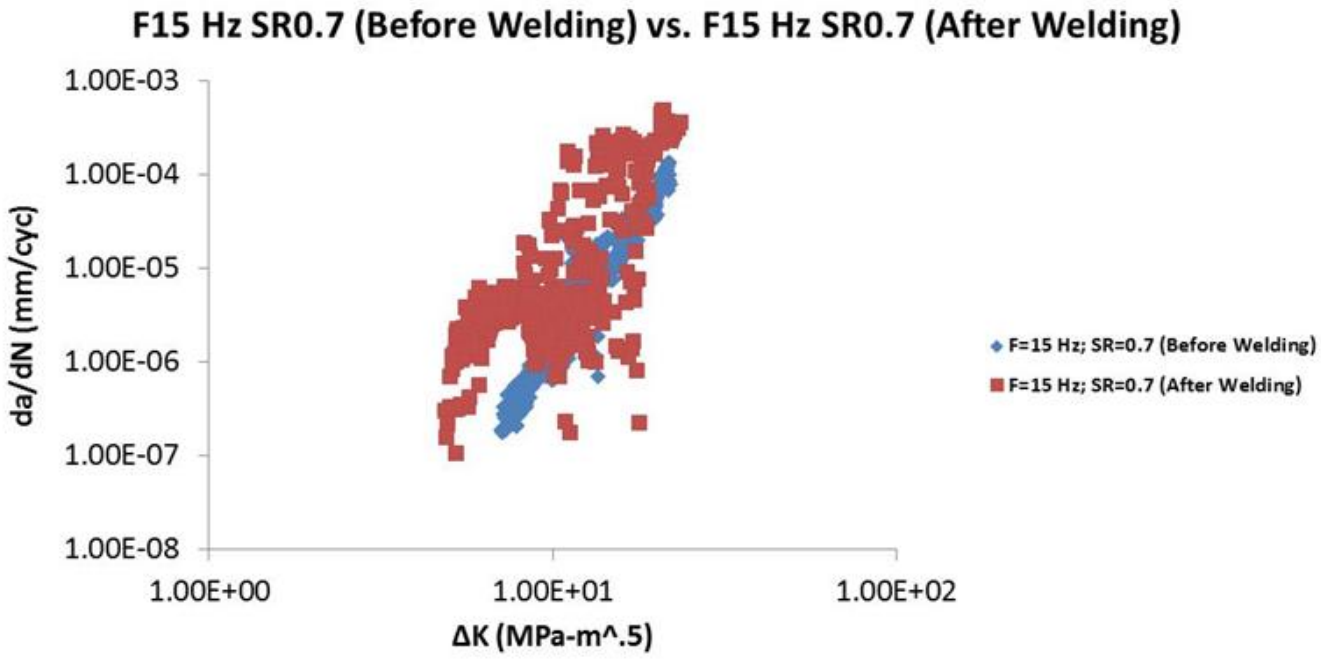

Figure 4.27 Effect of welding on FCG rate of Haynes 282 at a frequency of 15 Hz and stress ratio of 0.7 (Raw Data).

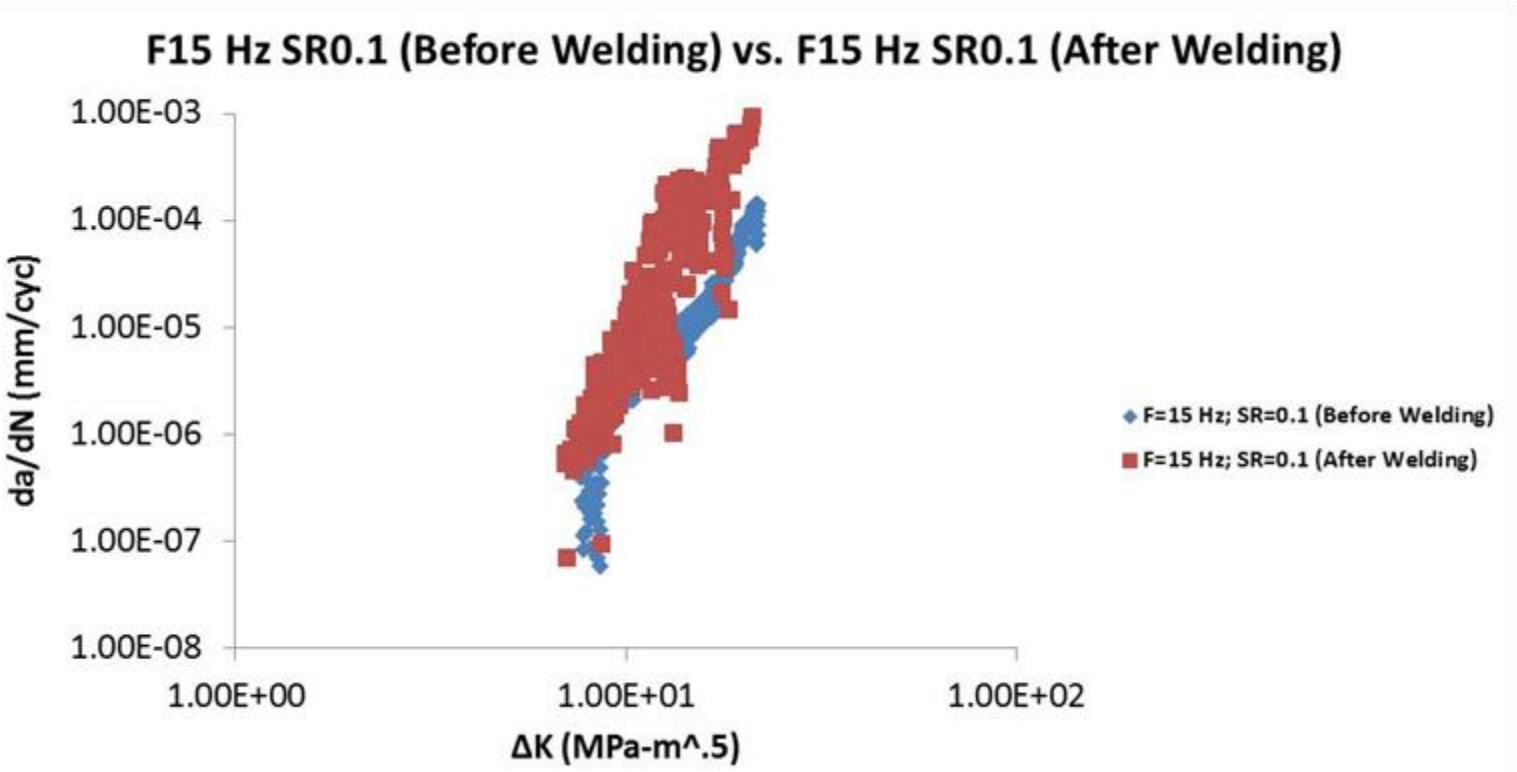

Figure 4.28 Effect of welding on FCG rate of Haynes 282 at a frequency of 15 Hz and stress ratio of 0.1 (Raw Data).

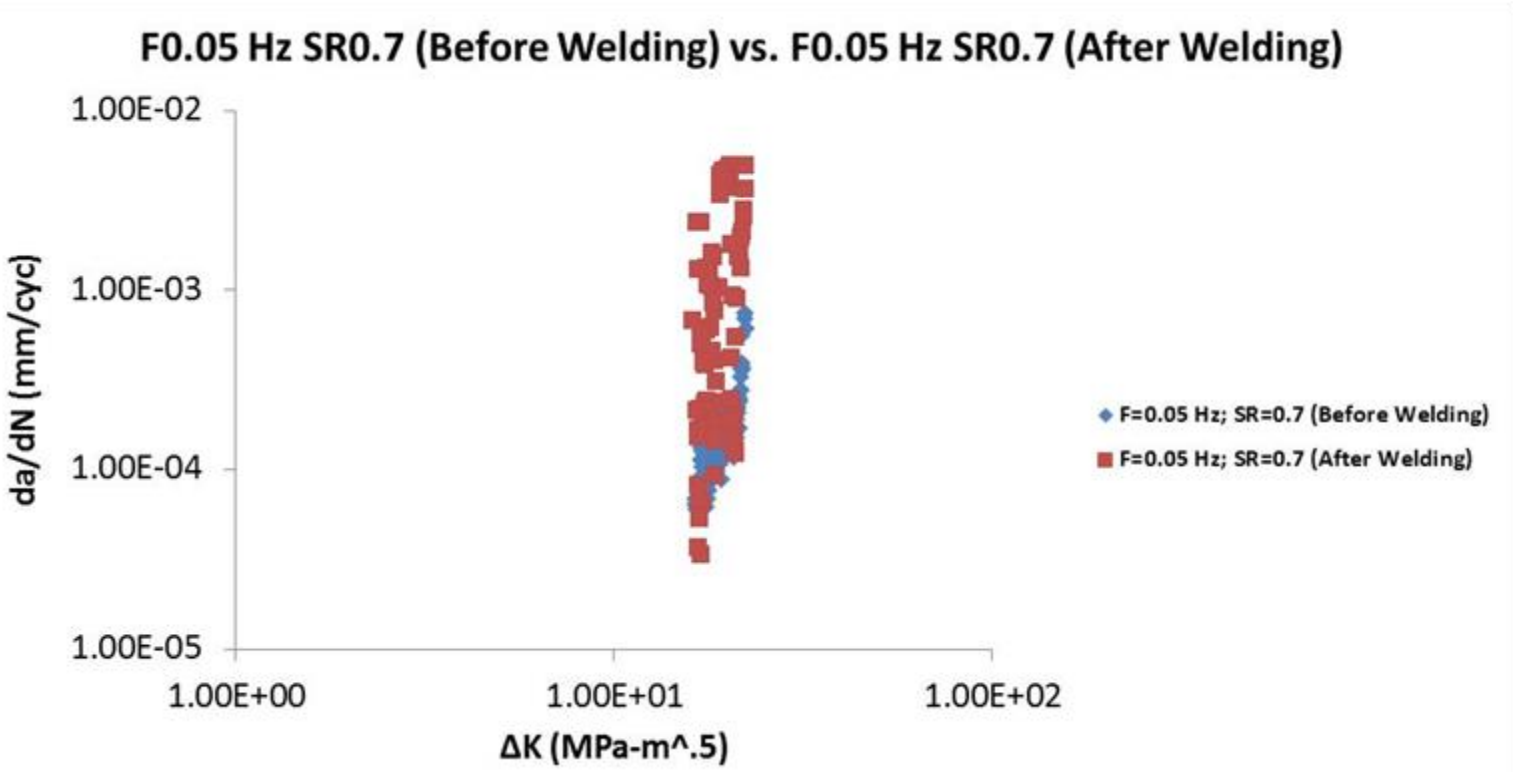

Figure 4.29 Effect of welding on FCG rate of Haynes 282 at a frequency of 0.05 Hz and stress ratio of 0.7 (Raw Data).

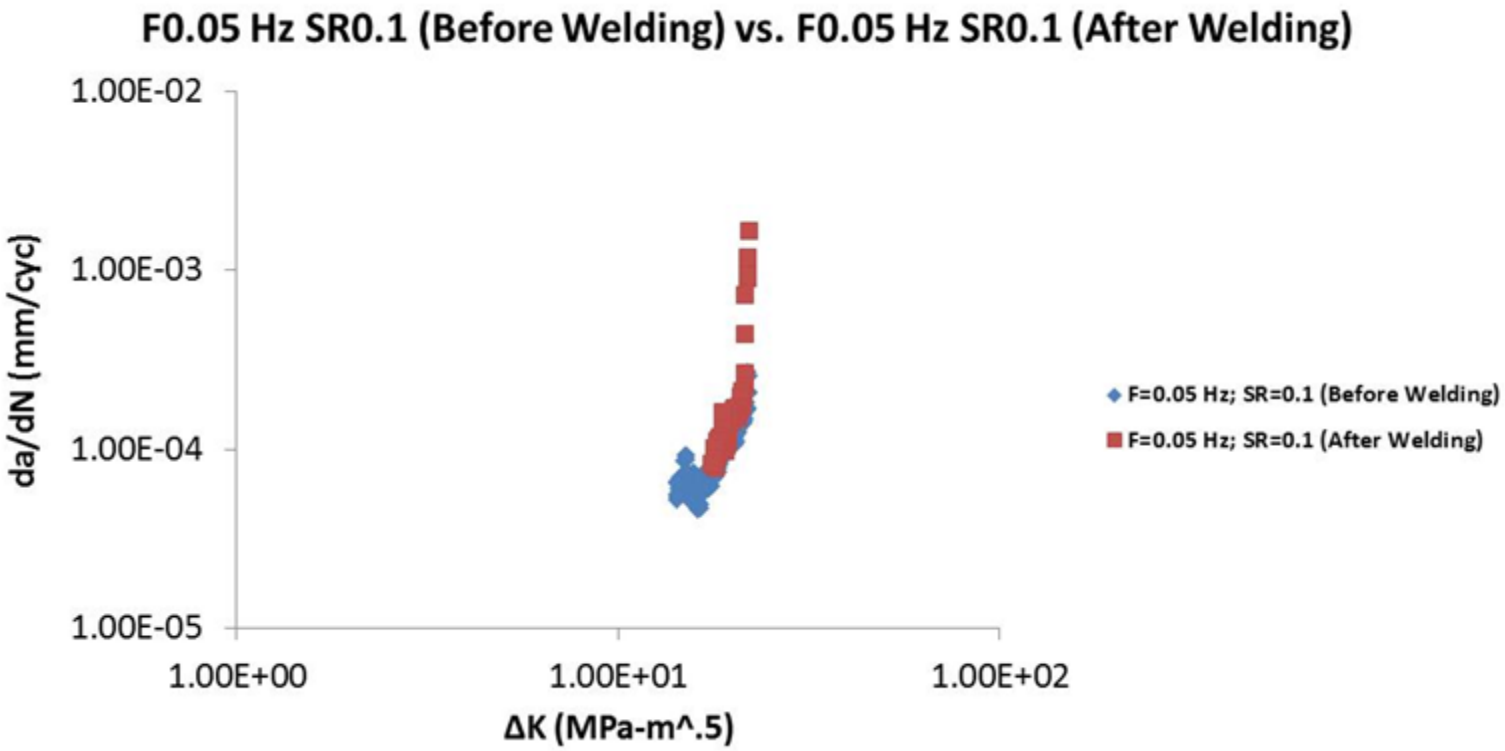

Figure 4.30 Effect of welding on FCG rate of Haynes 282 at a frequency of 0.05 Hz and stress ratio of 0.1 (Raw Data).

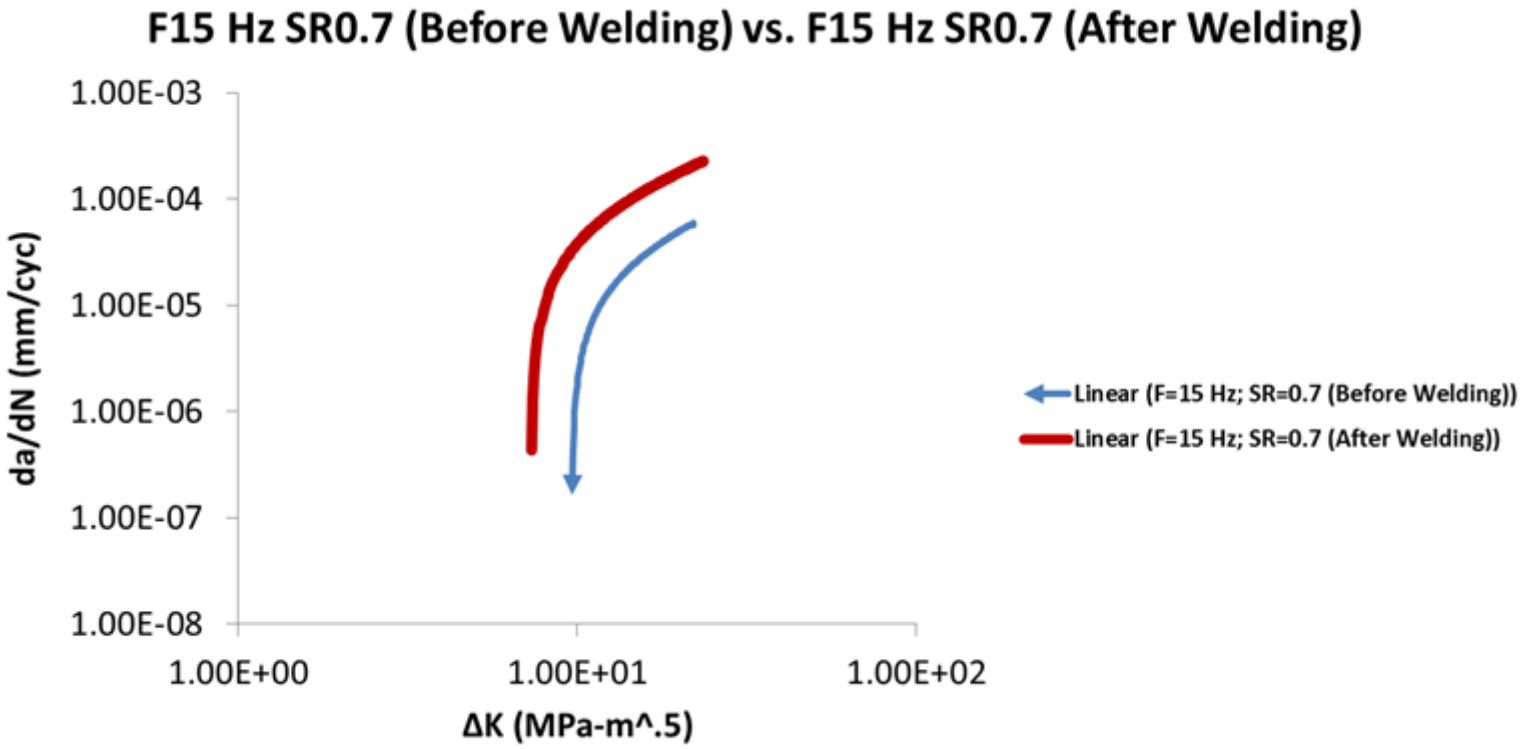

Figure 4.31 Effect of welding on FCG rate of Haynes 282 at a frequency of 15 Hz and stress ratio of 0.7 (Trendline Applied to Raw Data).

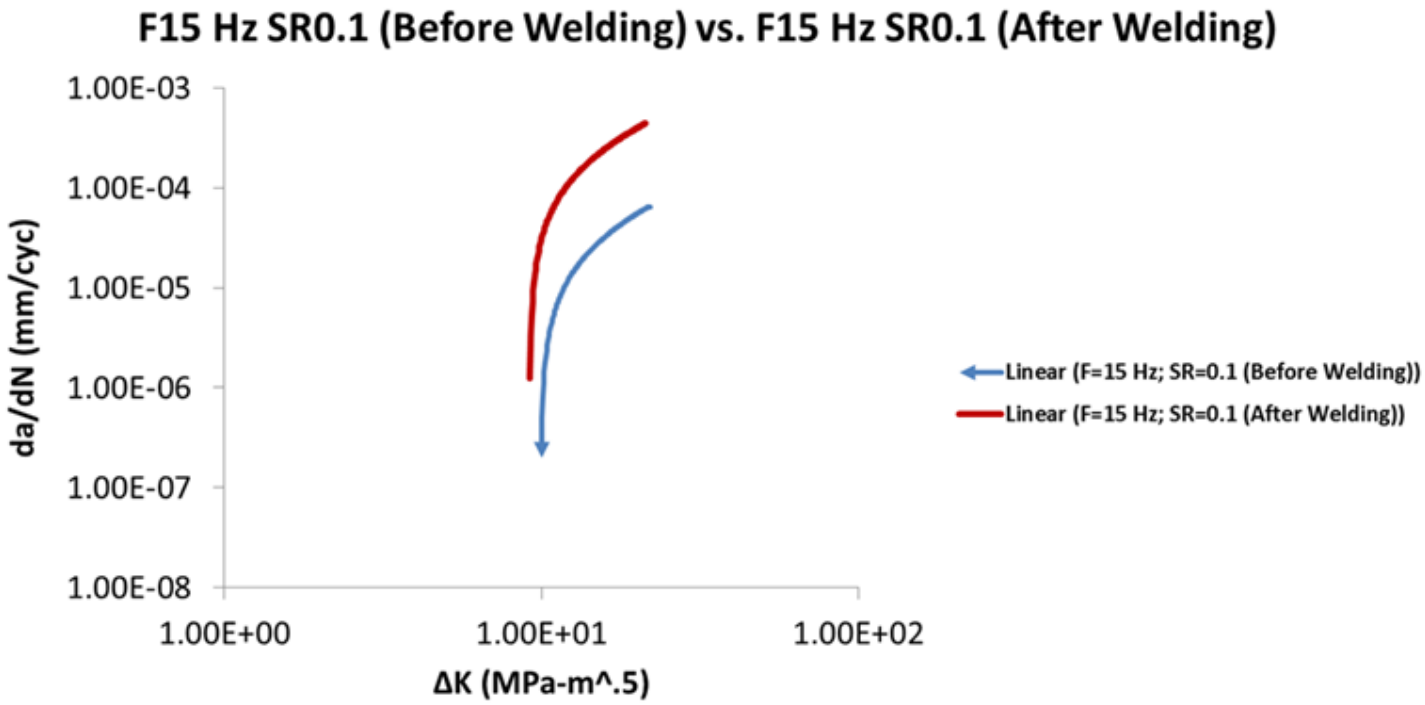

Figure 4.32 Effect of welding on FCG rate of Haynes 282 at a frequency of 15 Hz and stress ratio of 0.1 (Trendline Applied to Raw Data).

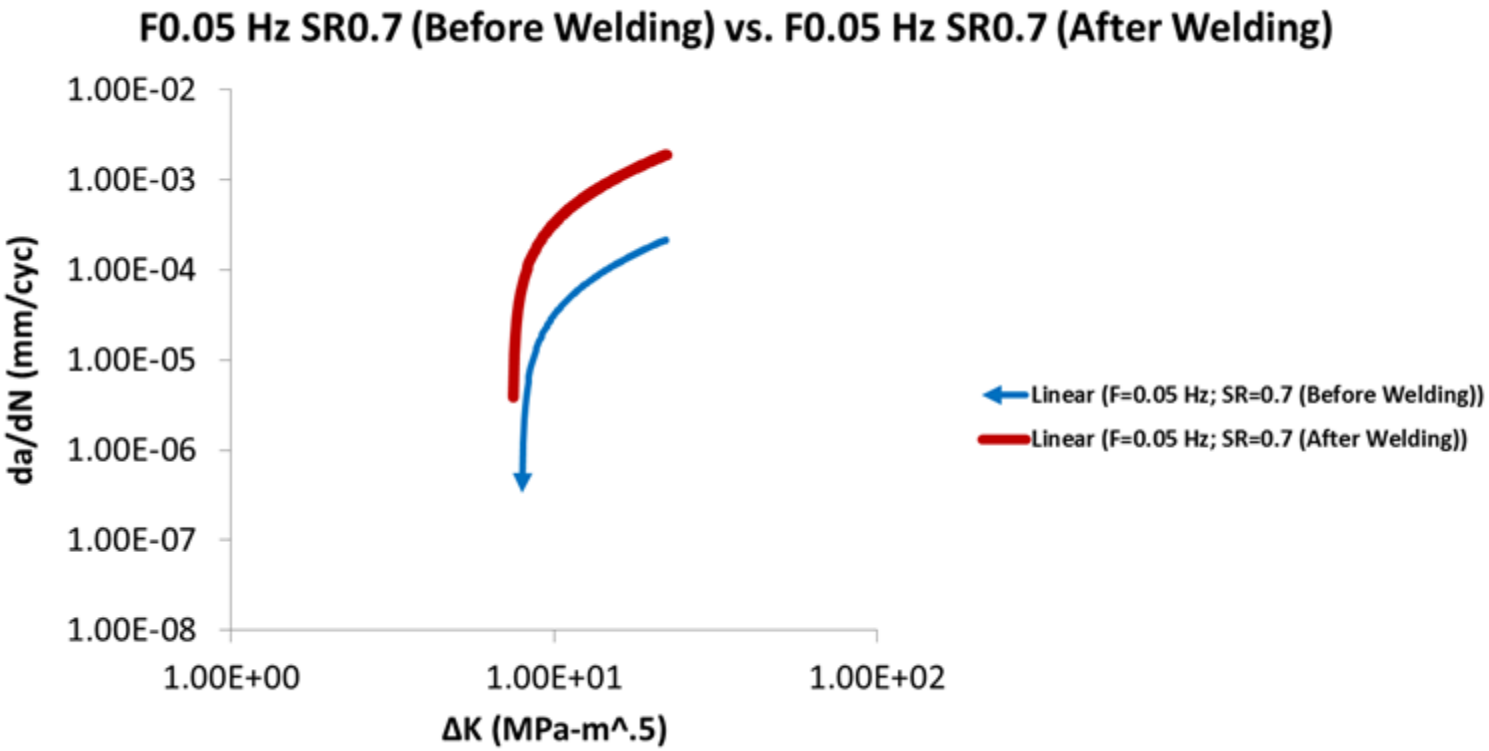

Figure 4.33 Effect of welding on FCG rate of Haynes 282 at a frequency of 0.05 Hz and stress ratio of 0.7 (Trendline Applied to Raw Data).

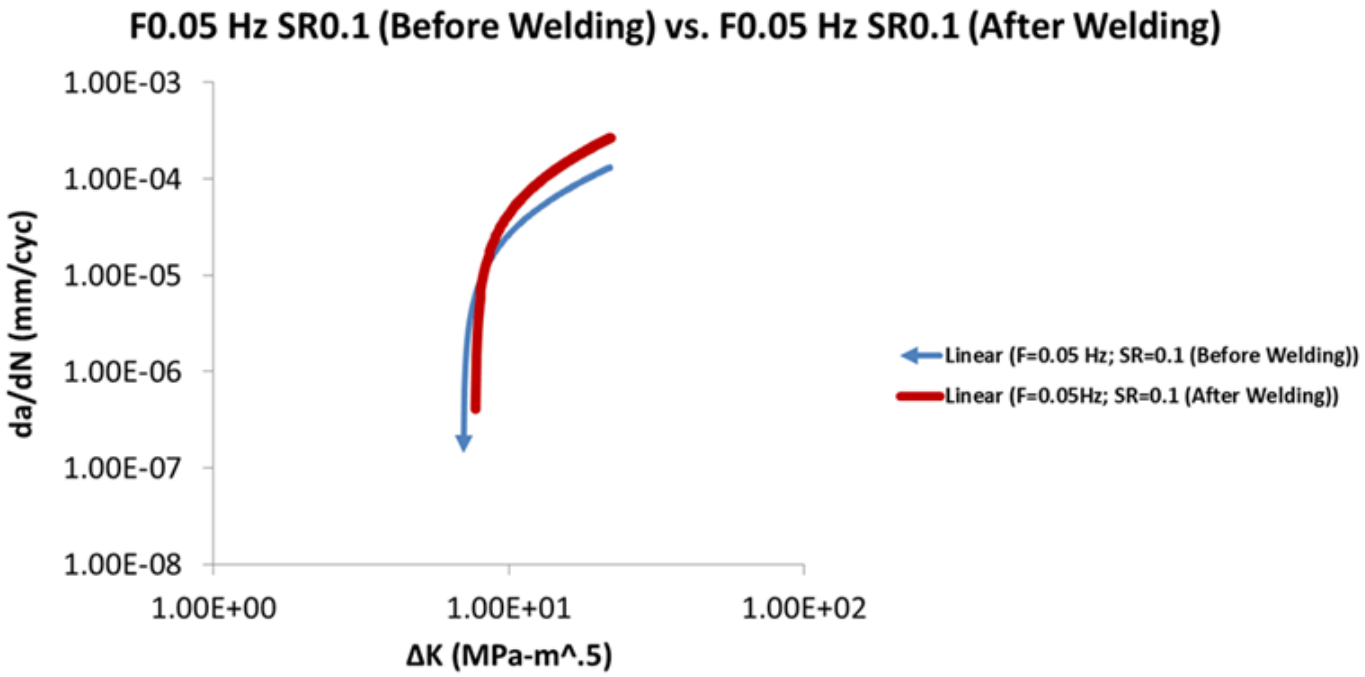

Figure 4.34 Effect of welding on FCG rate of Haynes 282 at a frequency of 0.05 Hz and stress ratio of 0.1 (Trendline Applied to Raw Data).

Table 4.2 Comparison of Paris Law Constants for Haynes 282 unwelded, and welded samples

	BEFORE WELDING		AFTER WELDING	
Test Parameters	Crack growth exponent 'm'	Crack growth intercept 'C'	Crack growth exponent 'm'	Crack growth intercept 'C'
F15 Hz SR0.7	0.82	$1x10^{-7}$	3.1	$1x10^{-6}$
F15 Hz SR0.1	1.02	$1.8x10^{-8}$	1.38	$6.7x10^{-7}$
F0.05 Hz SR0.7	1.83	$4.6x10^{-7}$	1.9	$6.4x10^{-6}$
F0.05 Hz SR0.1	1.76	$7.5x10^{-7}$	2.27	$9.2x10^{-7}$

The FCG exponent is an important parameter to use in assessing the FCG behaviour of materials because it determines the FCG life of the materials [145]. It represents the slope of the plot of *da/dN* versus *ΔK* in the Paris regime. Hence, a steeper slope of the plot in the Paris regime means higher FCG exponent, and that represents an increase in the FCG rate. It can be observed from Table 4.2 that the FCG exponent increases after welding, which suggests a steeper slope and, hence, FCG rate. For instance, at a frequency of 15 Hz and stress ratio of 0.7, the FCG exponent increased from 0.82 to 3.1 after welding. This indicates that there is a 278% increase in the FCG exponent value due to welding. Similarly, at a frequency of 0.05 Hz and stress ratio of 0.1, the FCG exponent increased from 1.76 to 2.27 after welding; this represents an increase of 29% in the FCG exponent value due to welding. Hence, both Figures 4.31 to 4.34 and Table 4.2, substantially demonstrate the deleterious effect of welding on the FCG rate of Haynes 282.

In essence, the lowest level of cracking which was observed at 1100°C/2 h/furnace cooling is not at a tolerable level for service.

The increase in the FCG rate of Haynes 282 after welding is attributable to the occurrence of cracking in the HAZ during the welding process.

The deleterious effect of HAZ cracking on the FCG rate of Haynes 282 after welding can be related to the general influence that cracks exert on the driving force for FCG, stress-intensity factor (K). The magnitude of the stress-intensity factor is directly related to the magnitude of the applied nominal stress, σ_{nom}, and the square root of the crack length, *a*, as shown in the general form of the stress-intensity factor [82]:

$$K = \sigma_{nom}\sqrt{a}\,.f(g) \quad \text{.....(4.7)}$$

where *f(g)* is a parameter that depends on the geometry of the particular member and the crack geometry. Hence, from equation 4.7, it can be deduced that an increase in the crack length will lead to an increase in the driving force for FCG, *K*, and, consequently, result in an increase in the FCG rate. Therefore, one of the ways that HAZ cracks increase the FCG rate of Haynes 282 after welding, is by increasing the crack length of pre-fatigue cracks in Haynes 282. Potentially, this can occur when HAZ cracks interact with the pre-fatigue cracks in Haynes 282. The interaction of HAZ and pre-fatigue cracks can possibly increase the crack length of the pre-fatigue cracks. Consequently, this will increase the driving force for the FCG of the pre-fatigue cracks, and as a result, lead to an increase in the FCG rate of Haynes 282 after welding.

Additionally, another way by which the driving force for FCG rate can be increased is by increasing the stress-intensity field ahead of the pre-fatigue crack. Potentially, this can occur when the stress-intensity field ahead of the pre-fatigue crack combines with the coalesced stress-intensity fields ahead of the HAZ cracks. The amalgamation of the stress-intensity fields of the pre-fatigue crack and that of HAZ cracks, can possibly increase the driving force for the FCG of the pre-fatigue crack, and as a result, lead to an increase in the FCG rate of Haynes 282 after welding.

Due to the importance of the welding process for fabrication and repair of Haynes 282 components and structures, it is imperative that innovative ways of improving the FCG properties of Haynes 282 after welding be developed.

It is known that microstructures that facilitate heterogeneous slip have lower FCG rates. Therefore, this knowledge is used in this work to develop two post weld heat treatments (Heat Treatment B, and Heat Treatment C which is a new thermal treatment schedule) to enhance resistance to FCG in Haynes 282 superalloy. Table 3.3 shows the parameters of the post weld heat treatments. Heat

Treatment B increases the grain size of Haynes 282 after welding from ~250 to ~350 μm. Heat Treatment C, on the other hand, produces coherent gamma prime precipitates of shearable sizes, which are observable under the SEM. As shown in Figures 4.35 to 4.39, these two post weld heat treatments are successful in facilitating the occurrence of heterogeneous slip during the FCG of Haynes 282. The occurrence of precipitate shearing, and presence of slip bands and dislocation pairs are indicative of heterogeneous slip [28]. These features are shown in Figure 4.35 (slip bands), Figure 4.36 (dislocation pairs), and Figure 4.37 (precipitate shearing). The TEM data in Figures 4.35 to 4.37 were obtained from FCG samples that were subjected to the post weld heat treatment C. Additionally, a significant occurrence of crack meandering, and considerable roughness of the fracture surface were observed in fatigue crack samples that were subjected to the Heat Treatment B, as shown in Figures 4.38 and 4.39 respectively.

The two post weld heat treatments developed in this work significantly reduce the FCG rate of Haynes 282 after welding as shown in Figures 4.40 to 4.43. Specifically, Figures 4.40 and 4.41 represent data that show the reduction in the FCG rate of Haynes 282 after welding, due to the use of Heat Treatment C. Figures 4.42 and 4.43, on the other hand, represent data that show the reduction in the FCG rate of Haynes 282 after welding due to the use of Heat Treatment B.

As shown in Figures 4.44 to 4.47, this trend is more discernible when a trendline (created by MS Excel software) is applied to all the data. Furthermore, this decrease in the FCG rate of Haynes 282 after welding due to the use of these two post weld heat treatments is numerically confirmed, in Tables 4.3 and 4.4. Table 4.3 shows the Paris law constants (FCG exponent '*m*', and FCG coefficient '*C*') for Haynes 282 after welding, and post weld heat treatments *A* and *C*. On the other hand, Table 4.4 shows the Paris law constants (FCG exponent '*m*', and FCG coefficient '*C*') for Haynes 282 after welding, and for post weld heat treatments *A* and *B*.

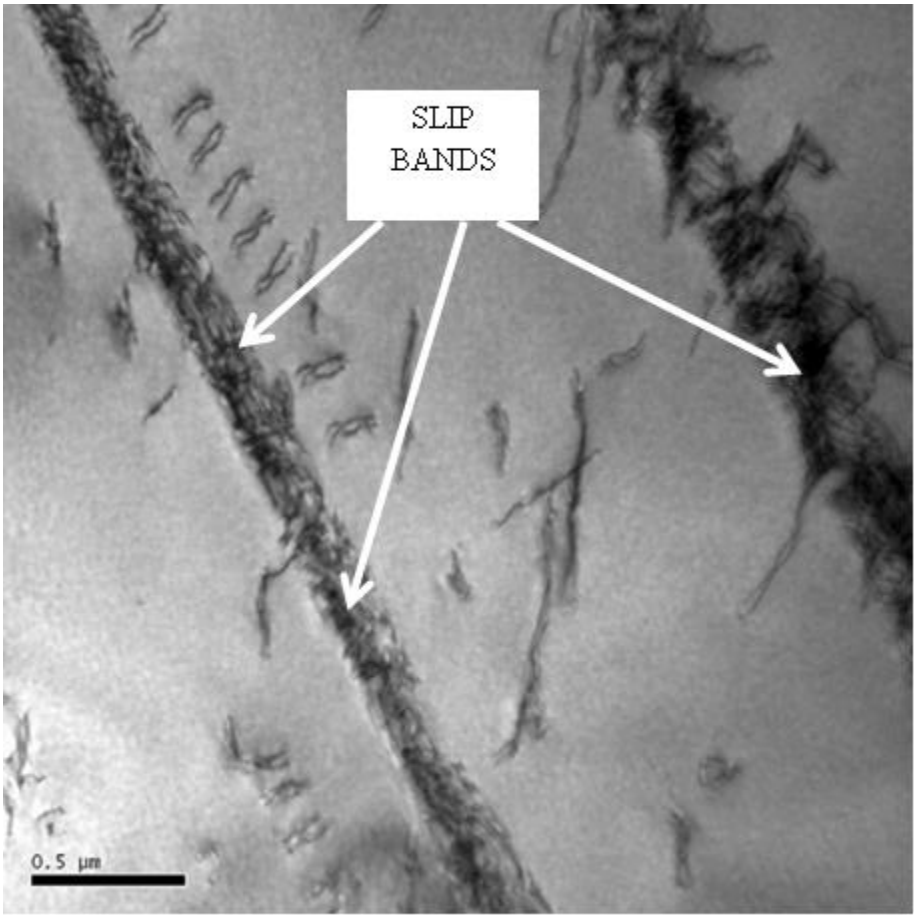

Figure 4.35 TEM micrograph showing slip bands.

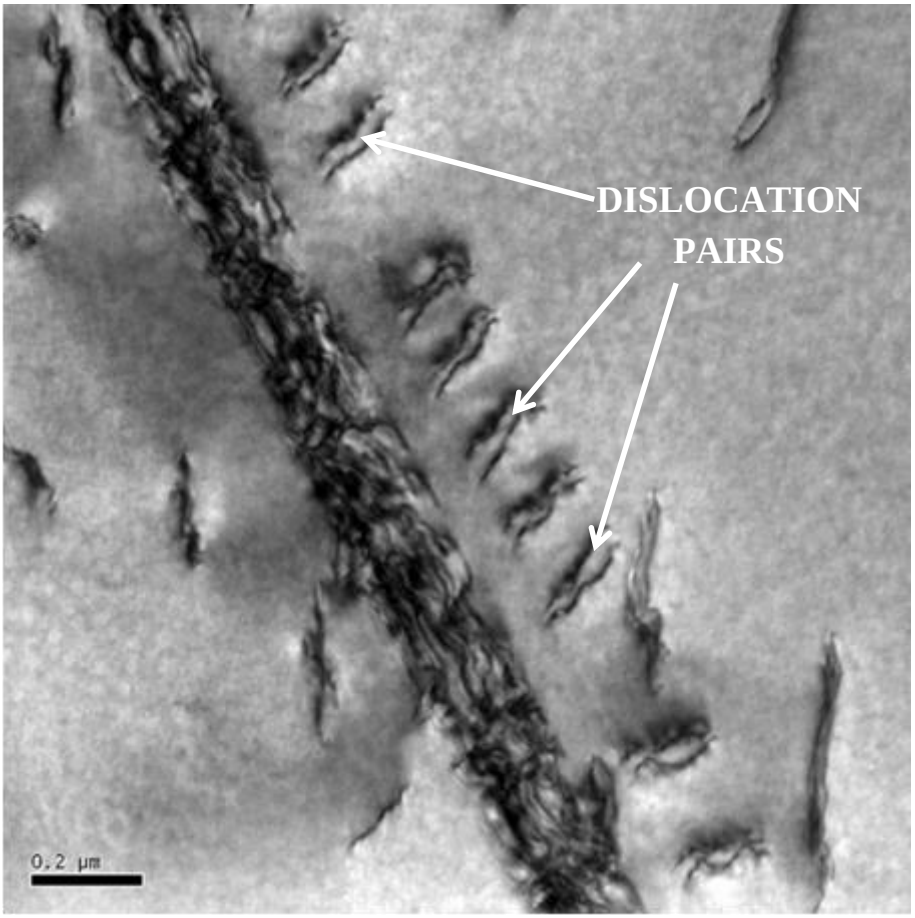

Figure 4.36 TEM micrograph showing dislocation pairs.

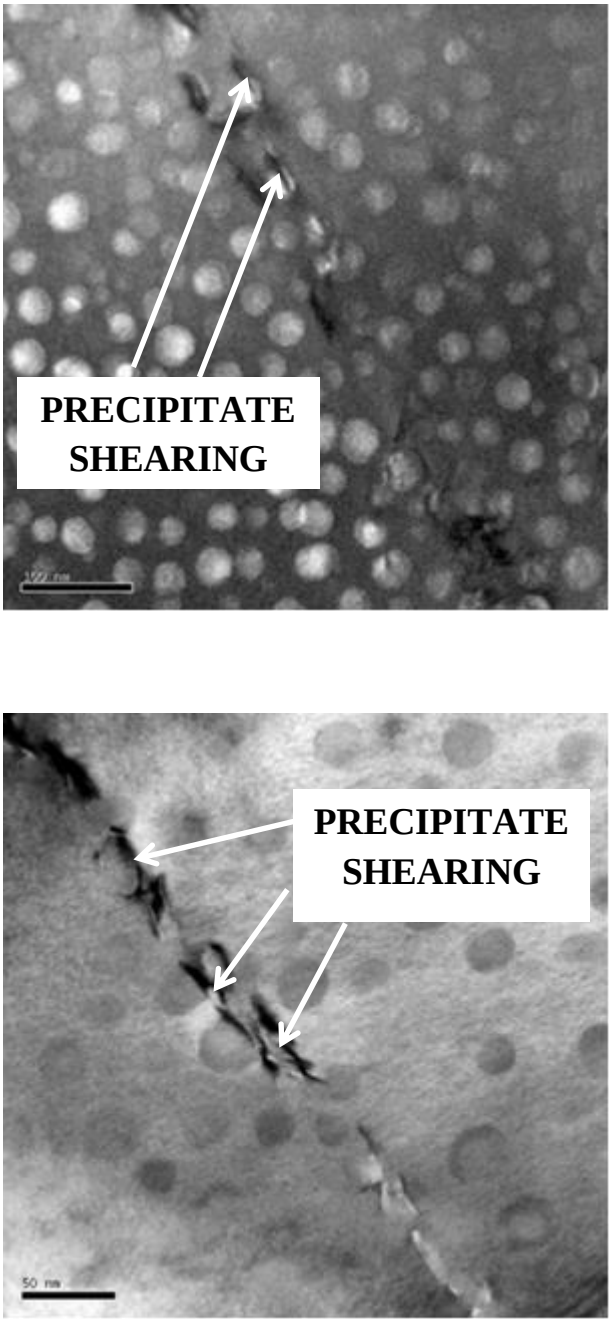

Figure 4.37 TEM micrographs showing precipitate shearing.

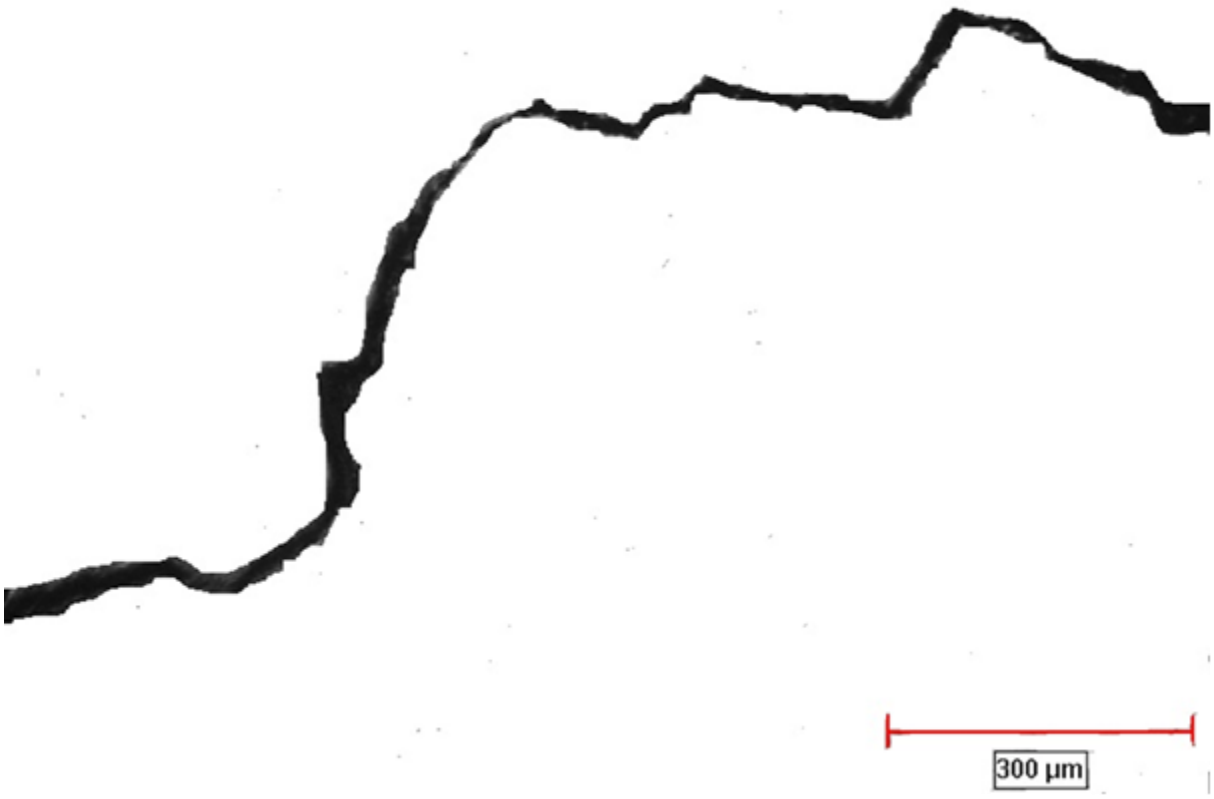

Figure 4.38 Optical microscope micrograph showing fracture profile.

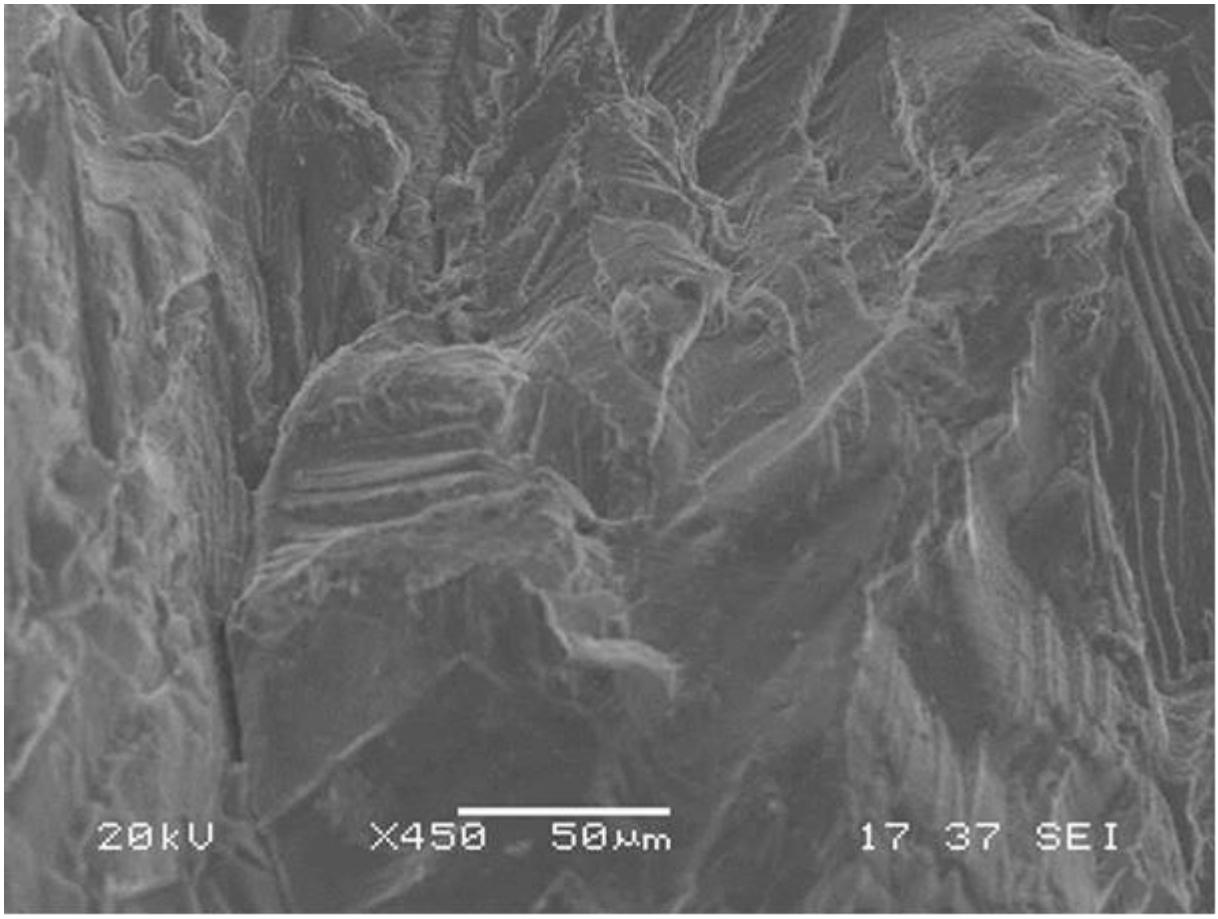

Figure 4.39 SEM micrograph showing roughness of fracture surface.

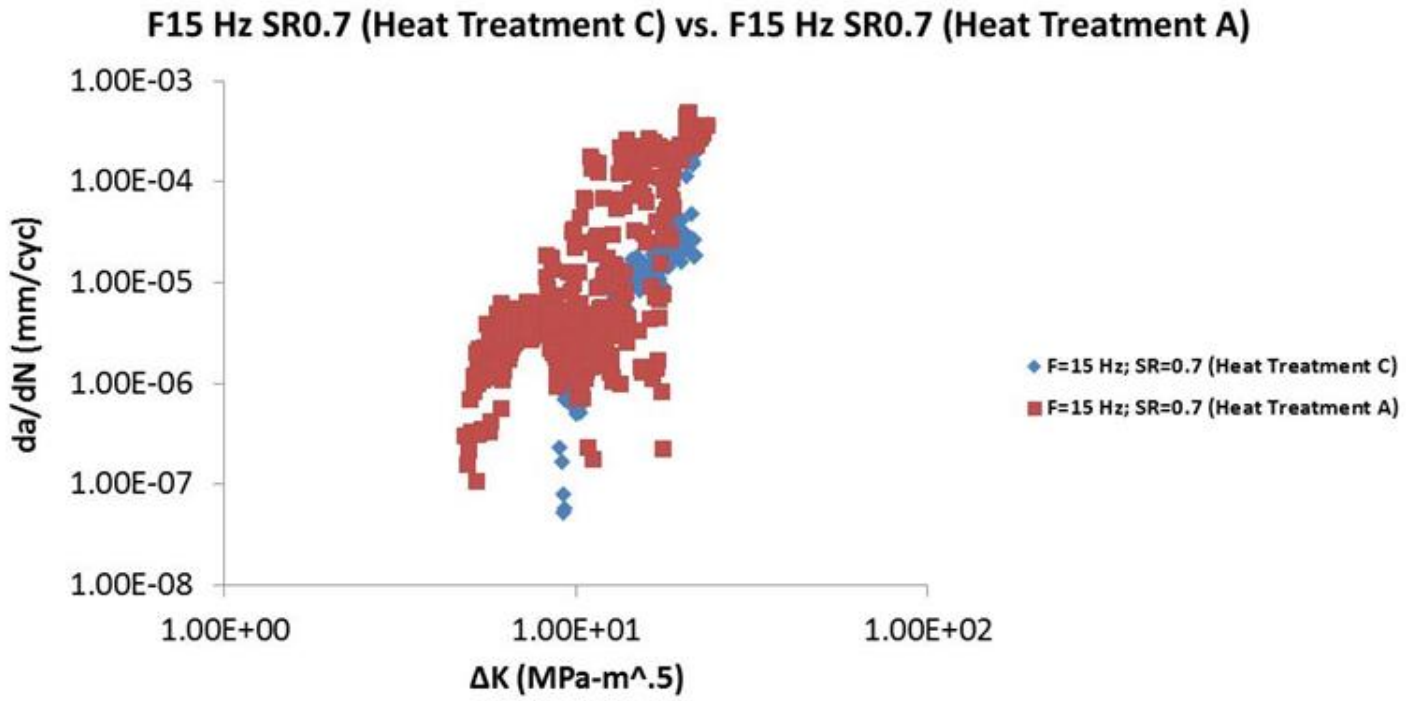

Figure 4.40 Comparison of FCG rate of Haynes 282 samples subjected to Heat treatment C, and Heat treatment A at a frequency of 15 Hz and stress ratio of 0.7 (Raw Data).

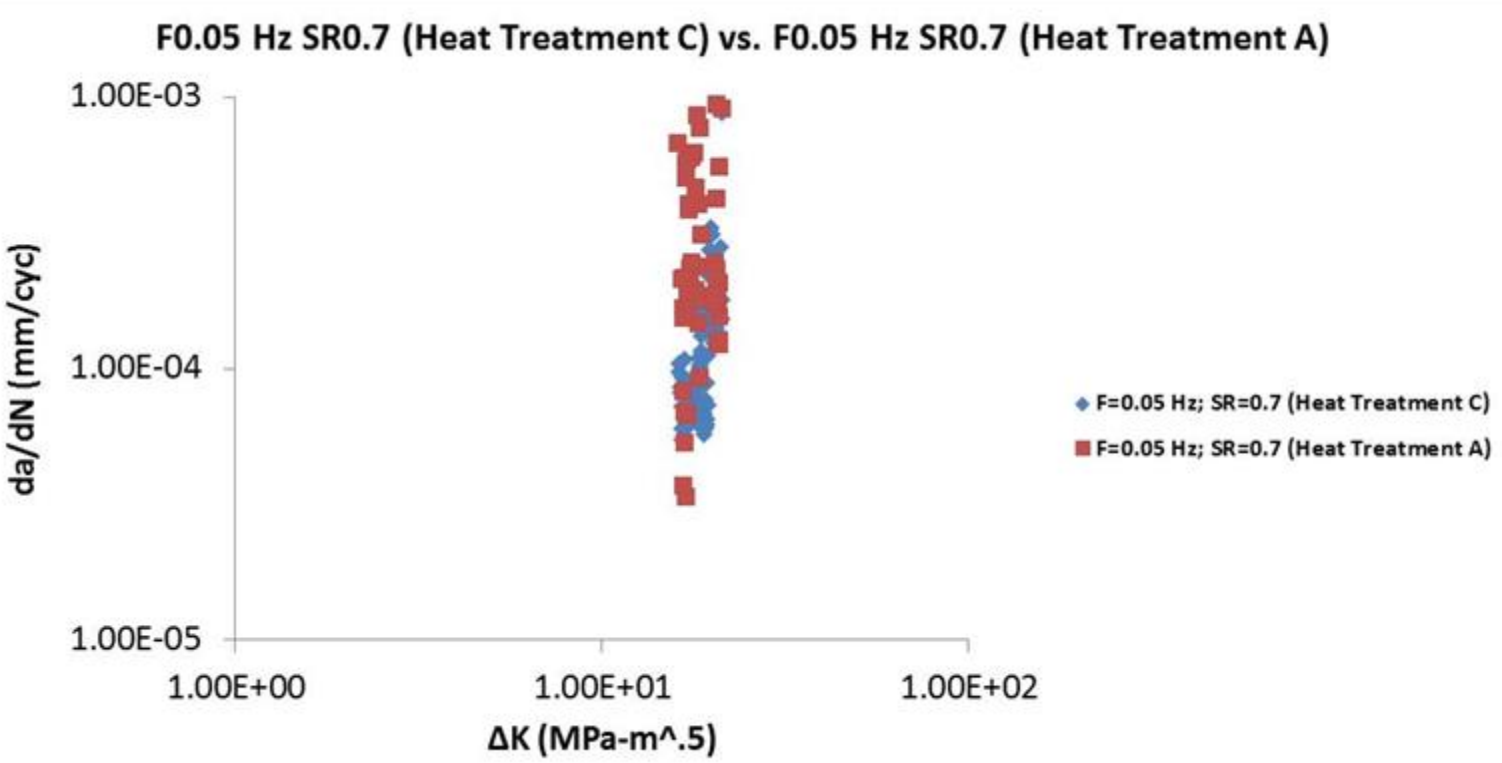

Figure 4.41 Comparison of FCG rate of Haynes 282 samples subjected to Heat treatment C, and Heat treatment A at a frequency of 0.05 Hz and stress ratio of 0.7 (Raw Data).

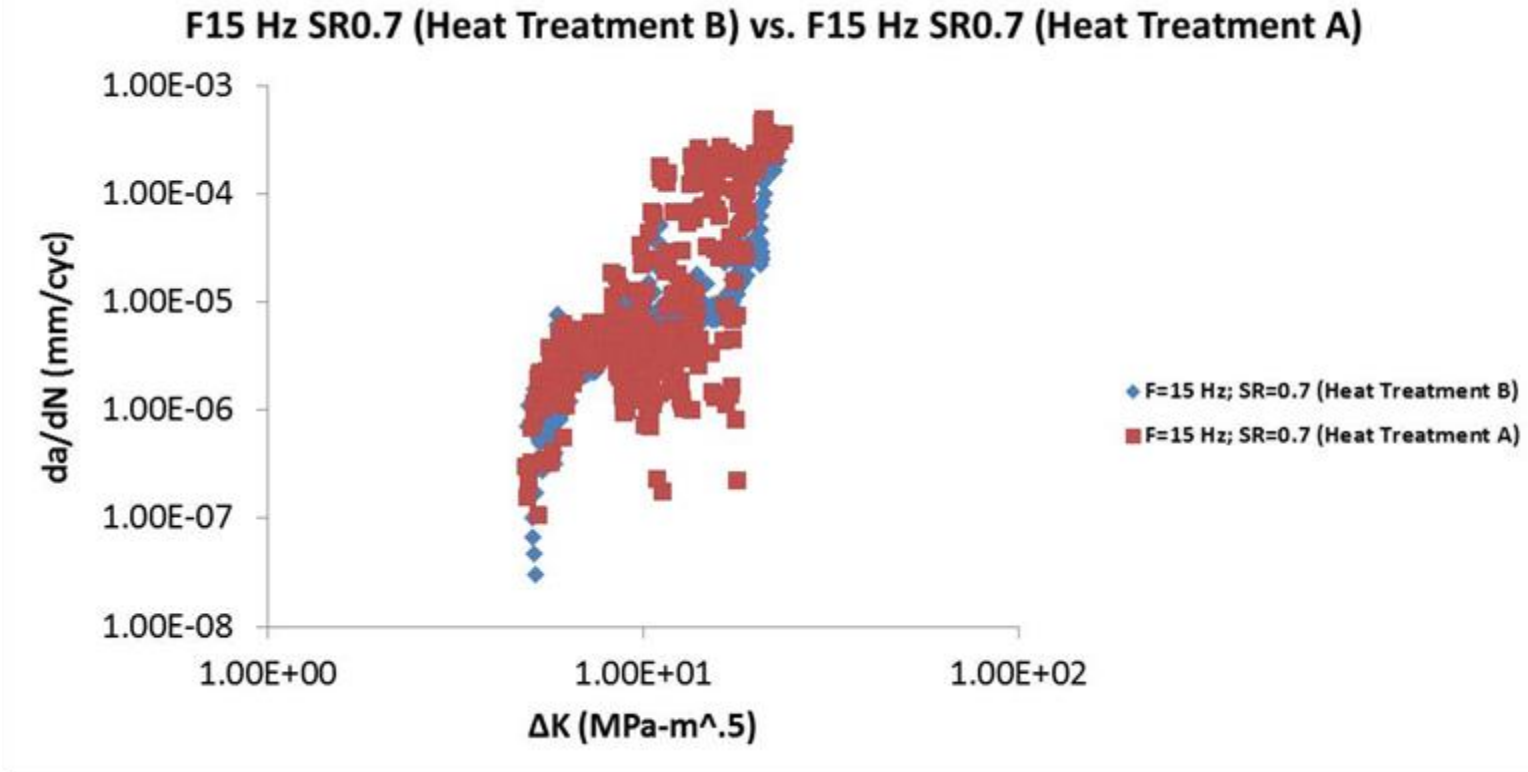

Figure 4.42 Comparison of FCG rate of Haynes 282 samples subjected to Heat treatment B, and Heat treatment A at a frequency of 15 Hz and stress ratio of 0.7 (Raw Data).

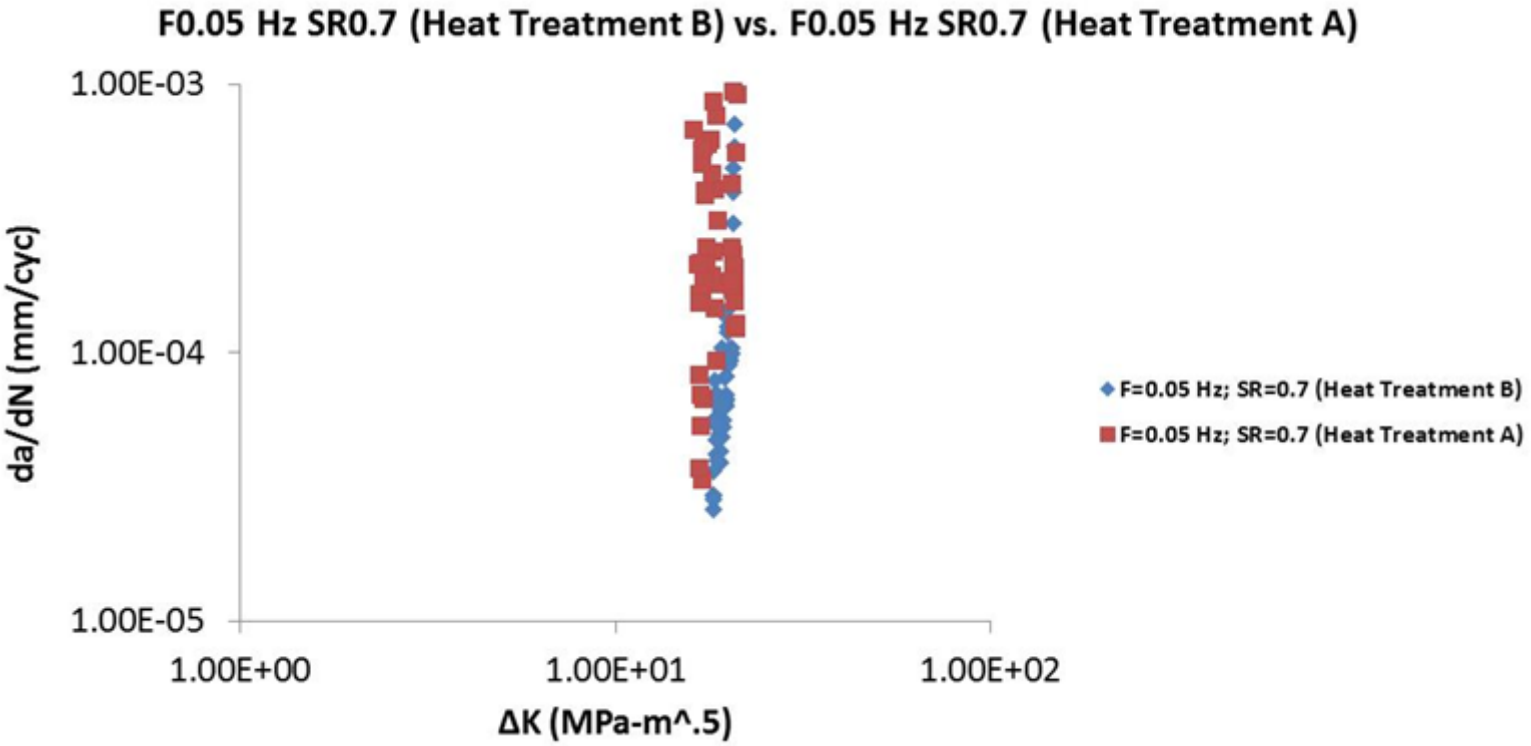

Figure 4.43 Comparison of FCG rate of Haynes 282 samples subjected to Heat treatment B, and Heat treatment A at a frequency of 0.05 Hz and stress ratio of 0.7 (Raw Data).

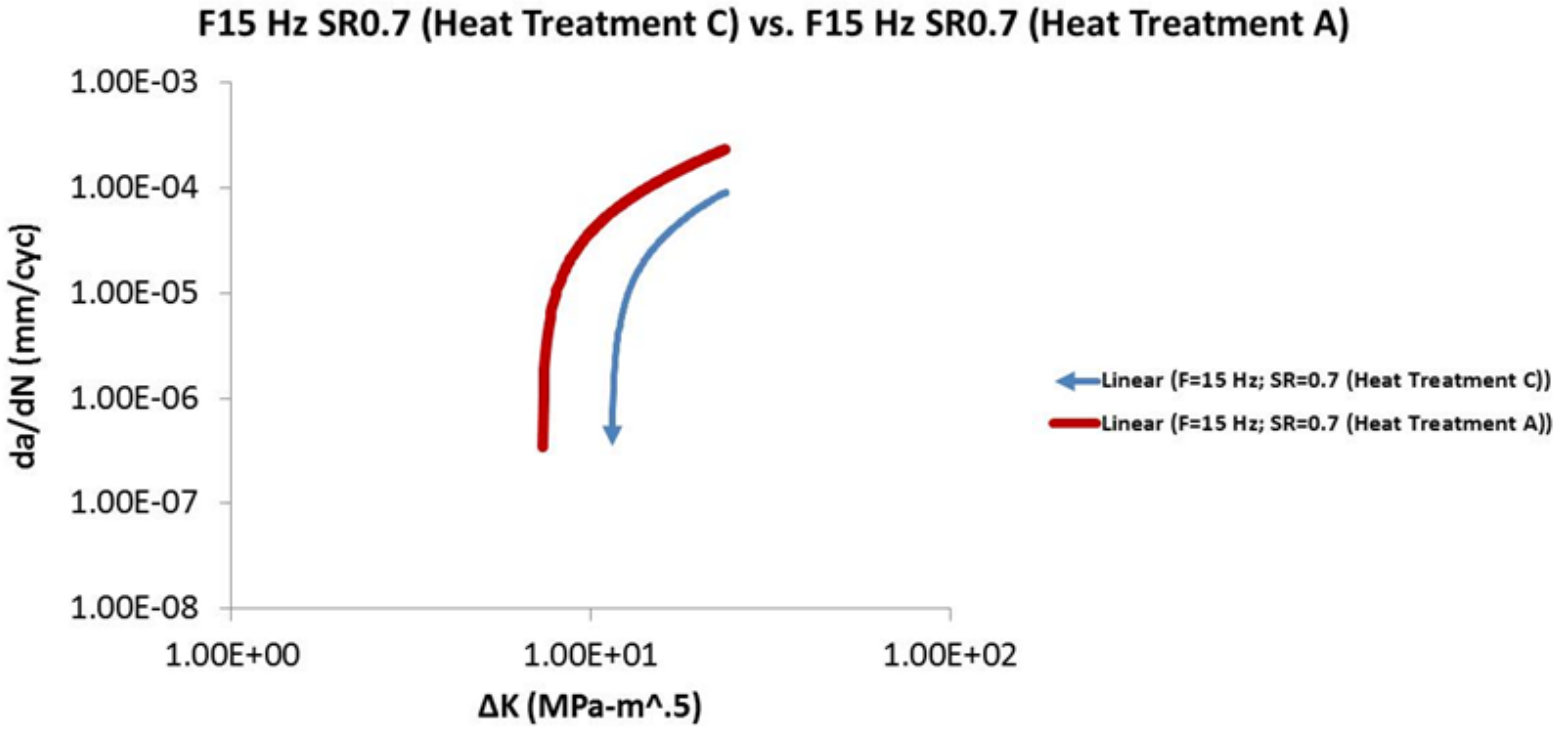

Figure 4.44 Comparison of FCG rate of Haynes 282 samples subjected to Heat treatment C, and Heat treatment A at a frequency of 15 Hz and stress ratio of 0.7 (Trendline Applied to Raw Data).

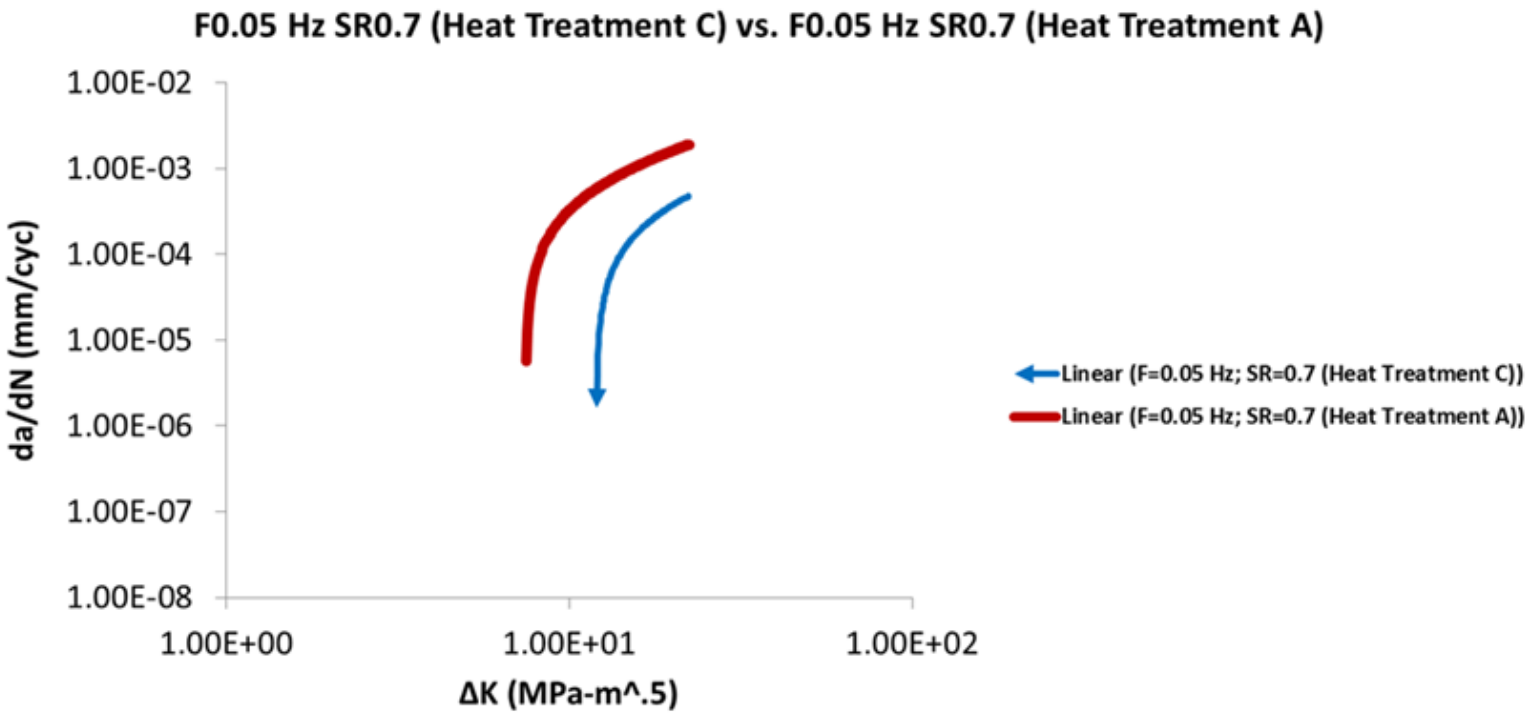

Figure 4.45 Comparison of FCG rate of Haynes 282 samples subjected to Heat treatment C, and Heat treatment A at a frequency of 0.05 Hz and stress ratio of 0.7 (Trendline Applied to Raw Data).

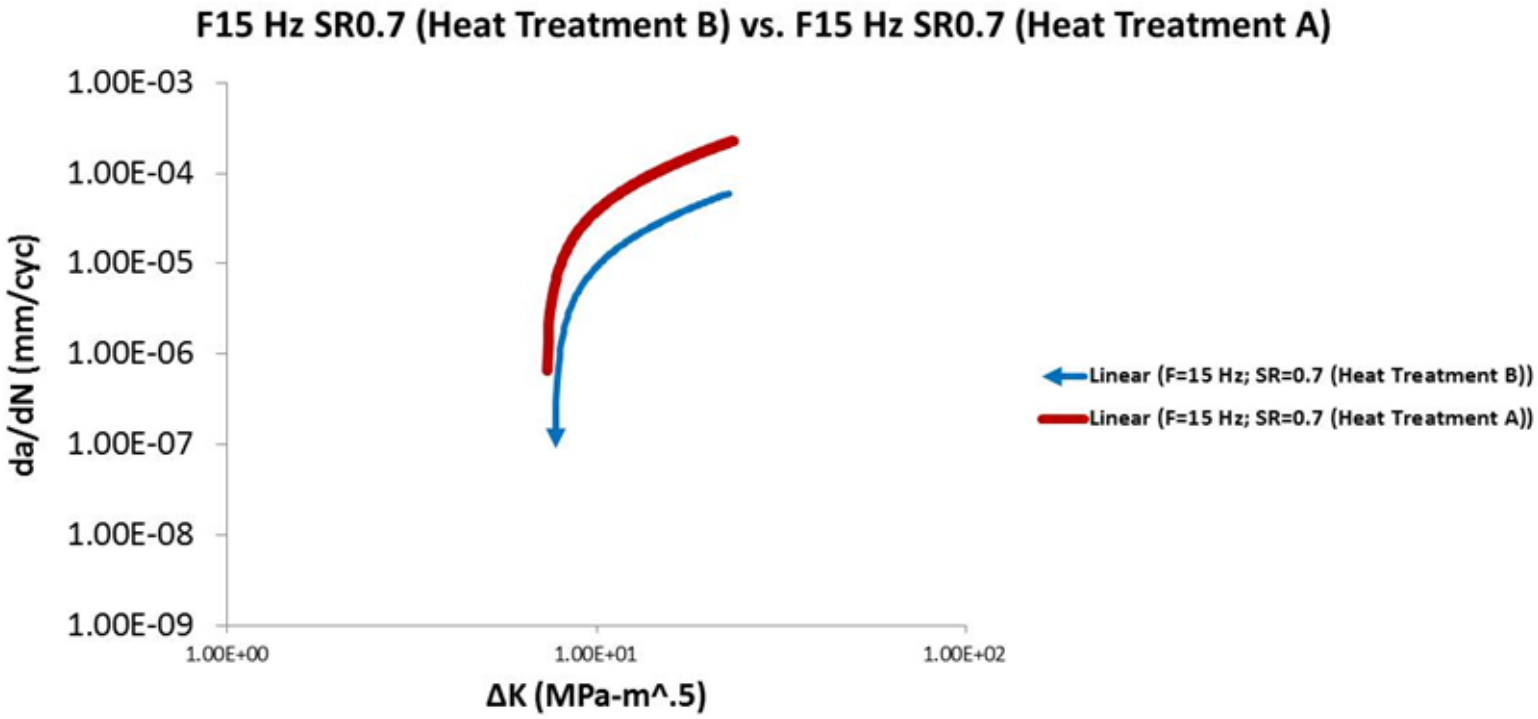

Figure 4.46 Comparison of FCG rate of Haynes 282 samples subjected to Heat treatment B, and Heat treatment A at a frequency of 15 Hz and stress ratio of 0.7 (Trendline Applied to Raw Data).

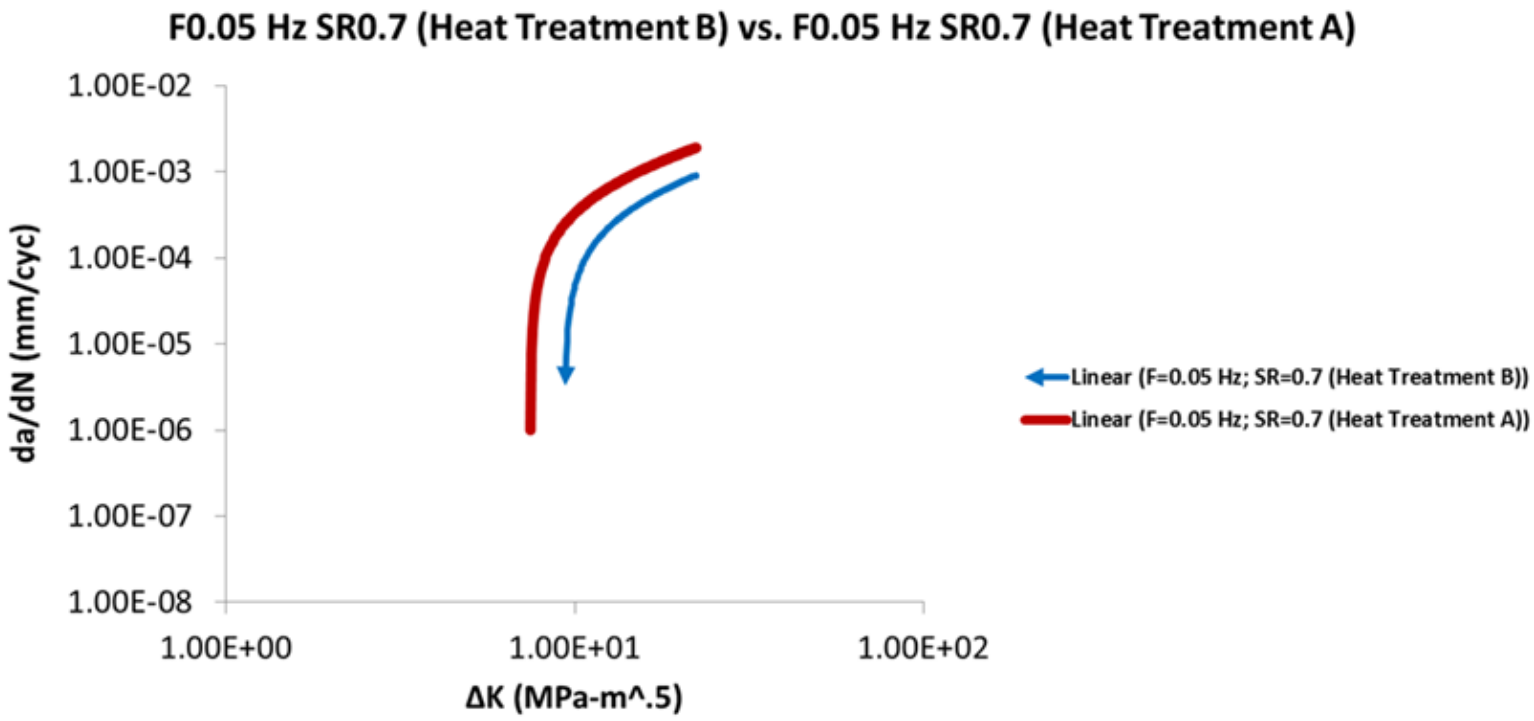

Figure 4.47 Comparison of FCG rate of Haynes 282 samples subjected to Heat treatment B, and Heat treatment A at a frequency of 0.05 Hz and stress ratio of 0.7 (Trendline Applied to Raw Data).

It is observed from Tables 4.3 and 4.4 that in comparison to post weld heat treatment (*A*), the manufacturer's recommended standard thermal treatment for the superalloy, the FCG exponent decreased for Heat Treatments *B* and *C*. This suggests a less steep slope and, hence, lower FCG rate. For instance, at a frequency of 15 Hz and stress ratio of 0.7, the FCG exponent decreases from 1.93 to 0.96 after subjecting welded Haynes 282 Heat Treatment *C*. This indicates that there is a 50% decrease in the FCG exponent value due to the Heat Treatment *C*. Similarly, at a frequency of 15 Hz and stress ratio of 0.7, the FCG exponent decreased from 2.385 to 1.11 after subjecting welded Haynes 282 to Heat Treatment *B*. This represents a decrease of 53% in the FCG exponent value due to the use of Heat Treatment *B*. Hence, both Figures 4.44 to 4.47 and Tables 4.3 and 4.4, substantially demonstrate the immense beneficial effect of the two post weld heat treatments (*B* and *C*) developed in this work on the FCG rate of Haynes 282 after welding.

The decrease in the FCG rate with increasing heterogeneity of slip can be attributed to several factors [146]: increased slip reversibility, less damage accumulation, and deviation of crack from path normal to the load axis.

An increase in slip reversibility creates a condition wherein plastic deformation occurs without a substantial increase in damage [147]. This is because the reversibility of slip facilitates the forward and reverse glide of dislocations, which leads to a decrease in the dislocation density at the crack tip. Hence, less damage is accumulated at the tip of the crack. Furthermore, due to the possibility of slip reversibility during the fatigue process, accumulation of damage at the tip of the crack is reduced when deformation is heterogeneously distributed, and it is unlikely for cross slip to occur [148]. A heterogeneous strain distribution produces less damage accumulation since the differing levels of deformation across the slip planes leads to varying resistance to the reverse glide of dislocations.

Table 4.3 Comparison of Paris Law Constants for Haynes 282 samples subjected to Heat Treatments C & A.

	Heat Treatment C		Heat Treatment A	
Test Parameters	Crack growth exponent 'm'	Crack growth intercept 'C'	Crack growth exponent 'm'	Crack growth intercept 'C'
F15 Hz SR0.7	0.96	$5x10^{-8}$	1.93	$1x10^{-6}$
F0.05 Hz SR0.7	1.45	$5.5x10^{-8}$	2.78	$7.3x10^{-6}$

Table 4.4 Comparison of Paris Law Constants for Haynes 282 samples subjected to Heat Treatments B & A.

	Heat Treatment B		Heat Treatment A	
Test Parameters	Crack growth exponent 'm'	Crack growth intercept 'C'	Crack growth exponent 'm'	Crack growth intercept 'C'
F15 Hz SR0.7	1.11	$1x10^{-7}$	2.39	$7.5x10^{-7}$
F0.05 Hz SR0.7	1.22	$6x10^{-7}$	2.76	$4.3x10^{-6}$

As a result, compared to a homogeneous strain distribution where deformation is relatively the same across the slip planes, the reverse glide of dislocations is enhanced in a heterogeneous strain distribution. Consequently, this leads to a reduced density of dislocations at the crack tip and, hence, less damage accumulation. Invariably, this causes slower FCG rate in microstructures that heterogeneously deform in comparison to those that facilitate homogeneous deformation.

The presence of shearable precipitates leads to reversibility of slip by engendering planar slip. In comparison to Orowan looping, the less resistance to dislocation motion provided by shearable precipitates facilitates slip that occurs in the same plane. The occurrence of planar slip means that the forward and reverse glide of dislocations occurs on the same path. This facilitates reversibility of slip, and consequently, results in less damage accumulation. As a result, the presence of shearable precipitates as produced in Heat Treatment *C* (which is a new thermal treatment schedule developed in this work), reduces the FCG rate of Haynes 282 after welding.

Besides coherent and ordered precipitates, the extent of heterogeneous strain distribution can be influenced by grain size [148] as observed in this work. Although a polycrystal material may have the interior of a grain deforming by a single slip, around the grain boundaries, large numbers of "geometrically necessary" dislocations must be available to enable the deformation of the material to occur as a whole and not break apart at the boundaries [149]. This is because the grain boundaries serve as an obstacle to dislocation motion. Hence, to overcome the resistance to dislocation motion provided by the grain boundaries, the dislocation density must of necessity be increased. Thus, larger grain size means more heterogeneous deformation, since the dislocation density cannot realistically be the same along all regions of the grain boundaries. Furthermore, larger grain size means fewer dislocations are required per unit volume of the grain to move out

of the active slip bands to accommodate grain boundary strains. This means planar slip will be facilitated consequently leading to a decrease in the rate of FCG.

Moreover, in all grains, crack paths are deflected at grain boundaries [28]. Hence, coarse grains, by allowing longer crack lengths before deflecting, promote higher and wider asperities and longer deviations from the perpendicular loading (angle between fatigue loading and direction of FCG). Considerable deviation of the crack path from the perpendicular loading will lead to a reduction in the driving force for FCG; consequently leading to a decrease in the FCG rate. Furthermore, periodic deflections in the fatigue crack at grain boundaries during crystallographic fracture can lead to a relatively tortuous crack path in coarser grained material. The tortuous crack path promotes the occurrence of roughness induced crack closure through the increased roughness of the fracture surface behind the crack tip. The mating of the fracture surfaces behind the crack tip will lead to a closure effect which will invariably lead to a reduction in the FCG rate of the coarser grains.

Hence, in this work, the deleterious effect of welding on the FCG rate of Haynes 282 is successfully nullified by using two post weld heat treatments that created microstructures which facilitates the occurrence of heterogeneous slip: Heat Treatment *B* (which produces larger grains), and Heat Treatment *C* (which produces shearable precipitates, and is a new thermal treatment schedule developed in this work).

CHAPTER 5

SUMMARY, CONCLUSIONS, and SUGGESTION FOR FUTURE WORK

The main objective of this PhD thesis is to methodically study the effect of LBW on the high temperature FCG behaviour of a newly developed aerospace superalloy Haynes 282, and how to mitigate any negative effects. To investigate the effect of LBW on the fatigue properties of Haynes 282, fatigue tests were carried out on both unwelded and welded Haynes 282 samples. Strain-controlled LCF push-pull type of fatigue and FCG tests were performed to evaluate the cyclic deformation characteristics and FCG properties of the newly developed alloy respectively. Additionally, microstructural studies were performed to assess the effects of thermal treatments and LBW on the alloy. The conclusions in this research are summarized as follows:

1. Haynes 282 experiences a relatively short period of initial cyclic hardening followed by a regime of cyclic softening to specimen failure at all the strain amplitudes employed in the work. This gives an indication on the path that the new alloy arrives at its final flow stress level, hence, this information is useful in determining appropriate loading for the alloy during service. This characteristic of Haynes 282 is reported for the first time in this research.
2. The cyclic deformation parameters observed in this work indicate strong fatigue deformation resistance of the newly developed superalloy. These parameters for Haynes 282 are reported for the first time in this study.

3. An increase in the stress ratio leads to an increase in the FCG rate. However, in contrast to the common assumption, the loading frequency is observed to have an effect on the FCG behaviour, which may be attributable to the strain rate effect. Thus, this study demonstrates that the loading frequency can have an effect on the FCG behaviour of Haynes 282 even at room temperature.
4. At a frequency of 15 Hz, the FCG rate consistently increases with an increase in temperature, at all stress intensities. This is attributed to the increase in homogeneity of slip, with increasing temperature, and its associated decrease in roughness induced crack closure.
5. At a frequency of 0.05 Hz, contrary to observations at 15 Hz, the FCG rate decreases with an increase in temperature, over a relatively large stress intensity range (ΔK). This phenomenon is attributed to the lower frequency of 0.05 Hz favouring the occurrence of oxide induced crack closure and dynamic strain ageing, which are both time dependent phenomena.
6. Microstructural analysis of laser beam welded Haynes 282 samples show that LBW of the alloy resulted in cracking in the HAZ. The HAZ cracking of Haynes 282 is attributed to grain boundary liquation caused by subsolidus liquation reaction of M_5B_3 boride particles.
7. An optimum pre-weld heat treatment that minimizes HAZ cracking in Haynes 282 was developed in this research.
8. Laser welding causes a deleterious effect on the FCG behaviour of the material by increasing the FCG rate. The increase in FCG rate is attributed to intergranular liquation cracking that occurs in the HAZ during the welding process.

9. The application of two post weld heat treatments, including a new one developed in this work, produces a considerable improvement in the FCG resistance of laser beam welded Haynes 282 by reducing the FCG rate to a level that is comparable to that of the unwelded material.
10. The effectiveness of the post weld heat treatments in improving FCG resistance is attributable to the microstructures induced by the thermal treatments, which cause enhancement of heterogeneous slip that impedes FCG.

In order to further evaluate the beneficial effect of the new post weld heat treatment developed in this research, it is recommended that other mechanical tests be performed on Haynes 282. These mechanical tests could encompass LCF, tensile, and fracture toughness testing. This is deemed necessary since failure of materials subjected to other forms of loading namely LCF, tensile and impact exists. Hence, if the beneficial effect of the new post weld heat treatment developed in this research is found to extend to these other forms of loading, its usefulness cannot be overemphasized.

REFRENCES

[1] Gardner, N., Lalonde, L.G., Boag, P., Windsor, R., Pole, K. (2006). Aerospace Industry. Historica Canada.

[2] Gregory, Sarah., Horton, Leslie., Miles, Staci., Rolson, Lauren., Skubala, Marcin. (2009). Aerospace Manufacturing Industry.

[3] Pike, L. M. (2008). Development of a fabricable gamma-prime strengthened Superalloy. TMS (The Minerals, Metals and Materials Society).

[4] Haynes 282 alloy. (2008). High temperature alloys. Haynes International, Inc.

[5] ASTM E 606-04. Standard practice for strain-controlled fatigue testing. ASTM International, West Conshohocken, PA 19428-2959, United States, p. 636.

[6] Yulin, Lu. (2005). High-temperature low cycle fatigue and crack growth behaviours of three superalloys: Hastelloy X, Haynes 230, and Haynes 188. PhD Thesis. The University of Tennesse, p. 2, 5.

[7] Ashbaugh, N.E., Buchanan, D.J., Hutson, A.L., John, R., Li, K., Porter, W.J., Stubbs, D.A. (2000). Life prediction methodologies for aerospace materials. University of Dayton research institute.

[8] Chang, K-M. and Xingbo, L. (2001) Effect of ɣ′ content on the mechanical behaviour of Waspaloy alloy system. Materials Science and Engineering. A308, pp. 1-8.

[9] Oshoba, L. O. (2012). A study on Laser Weldability Improvement of Newly Developed Haynes 282 Superalloy. PhD Thesis. The University of Manitoba.

[10] Mott, N.F. (1952). Imperfections in nearly perfects crystals. W. Shockley (Ed.), John Willey and Sons, New York, p. 173.

[11] Mott, N.F. and Nabarro, F.R.N. (1948). Report of conference on strength of solids. Phys. Sci, p. 1.

[12] Decker, R.F. (1969). Strengthening Mechanism in Nickel-Base Superalloys. Climax Molybdenum Company Symposium, Zurich.

[13] Durand-Charre, M. (1997). The microstructure of superalloys. CRC press. Amsterdam, Holland.

[14] Donachie, M.J. and Donachie S.J. (2002). Superalloy a Technical Guide. 2nd edition, ASM International, Materials Park, OH, p. 211.

[15] Raynor, D. and Silcock, J.M. (1970). Strengthening mechanism in gamma-prime precipitating alloys. Met. Sci. J. 4, p.121.

[16] Smith, W.F. (1993). Structure and properties of Engineering alloys. 2nd edition, New York McGraw-Hill, p. 504.

[17] Brown, L.M. and Ham, R.K. (1971). Strengthening methods in crystals. Elsevier Amsterdam, p. 9.

[18] Orowan, E. (1948). Symposium on Internal Stresses in Metals. Institute of Metals, London, p. 45.

[19] Sathian, Sujith. (1999). Metallurgical and Mechanical Properties of Ni-based Superalloy Friction Welds. M.Sc. Thesis. University of Toronto.

[20] Larson, J.M. (1976). Carbide morphology in P/M IN-792. Metall. Transac, 7A (10), p. 1497.

[21] Metals Handbook. (1972). 8th Edition, Vol. 17, American Society for Metals, Metals Park, OH.

[22] Decker, R.F. and Sims, C.T. (1972). The Metallurgy of Nickel-base alloys. The Superalloys. Sims, T.C and Hagel, W.C. Eds., John Wiley and Sons, New York, p 33.

[23] Ross, E.W. and Sims, C.T. (1987). Nickel-Base Alloys. The Superalloys. Sims T.C. and Hagel, W.C. Eds. John Wiley and Sons, New York, p. 97.

[24] Haynes 282 (2008). Heat resistance alloy at a glance. Haynes International, Inc.

[25] Alloy digests Haynes 282. (2006). A publication of ASM International material park, Ohio 44073-0002, U.S.A.

[26] Dieter, G. E. (1988). Mechanical Metallurgy. McGraw-Hill Book Company (UK) Limited.

[27] Stephens, R. R. (1991). In-situ short crack characterization of a nickel-base superalloy at ambient and elevated temperatures. PhD Thesis. The University of Utah.

[28] Schwarzkopf, E. A. (1989). The microstructural dependence of fatigue crack growth rates in a nickel base superalloy. PhD Thesis. Columbia University, pp. 1.

[29] Shyam, A. (2002). Deformation and fatigue behaviour of the nickel base superalloy KM4. PhD Thesis. Michigan Technological University, p. 7, 8.

[30] Coffin, L.F. (1954). Transaction of the American Society of Mechanical Engineers. 76, p. 931-950.

[31] Manson, S. S. (1954). Behaviour of materials under conditions of thermal stress. National Advisory Commission on Aeronautics: Report 1170, Lewis Flight Propulsion Laboratory.

[32] King, J. E. (1987). Fatigue Crack Propagation in Nickel Base Superalloys – Effects of Microstructure, Load Ratio and Temperature. Materials Science and Technology, 3, pp. 750-764.

[33] Andrews, R. G. (1991). High Temperature Fatigue Crack Initiation and Propagation Behaviour in Inconel 718 Turbine discs. M.Eng. Carleton University, p. 1.

[34] Weaver, M. J. Mechanical Property Requirements for Aero Gas Turbine Materials. Materials Science and Technology, 3, pp. 695-700.

[35] R. W. Landgraf. (1970). In Achievement of high fatigue resistance in metals and alloys. American Society of Testing and Materials, Philadelphia, STP 467, pages 3–36.

[36] Paris, P. C. (1964). The Fracture Mechanics Approach to Fatigue, Fatigue – An Interdisciplinary Approach. pp. 107-132.

[37] J. D. Morrow. (1965). In Internal friction, damping and cyclic plasticity. American Society of Testing and Materials, STP 378, page 72.

[38] O. H. Basquin. (1970). Proc. ASTM, 10: 625.

[39] Ritchie, R. O. (1988). Mechanisms of Fatigue Crack Propagation in Metals, Ceramics, and Composites: Role of Crack Tip Shielding. Materials Science and Engineering, 103A, pp. 15-28.

[40] Yablinsky, C. A. (2010). Characterization of fatigue mechanisms in Ni-based superalloys. PhD Thesis. The Ohio State University.

[41] Rice, J. R. (1968). A Path Independent Integral and the Approximate Analysis of Strain Concentration by Notches and Cracks. Journal of Applied Mechanics, Transactions ASME. Vol. 35.

[42] Theocaris, P. S. (1984). Experimental Methods for Determining Stress Intensity Factors, Fracture 84, Advances in Fracture Research. pp. 707-728.

[43] Elber, W. (1971). Damage Tolerance in Aircraft Structures. ASTM 486, American Society of Testing Materials. p. 230.

[44] Bowman, R. R. (1988). The effect of microstructure on the fatigue crack growth resistance of nickel base superalloys. PhD Thesis. Georgia Institute of Technology, p. 23.

[45] Ritchie, R. O. et al. (1980). Engineering Materials Technology, 102, p. 293.

[46] Ritchie, R. O. et al. (1981). Fatigue Thresholds. EMAS Publ. Ltd., Warley, U.K, p. 503.

[47] Wulf, T. (1974). Mechanical properties at high rates of strain. Oxford: The Inst. of Physics. p. 48.

[48] Tanaka, K. and Nojima, T. (1979). Mechanical properties at high rates of strain. Oxford: The Inst. of Physics. p. 48.

[49] Huan, W et al. (2009). Fatigue crack growth behaviours of a new burn-resistant highly-stabilized beta titanium alloy. Rare Metals. 28 (6), pp. 545-549.

[50] Ghonem, H. and Zheng, D. (1992). Frequency interactions in high temperature fatigue crack growth in superalloys. Metallurgical Transactions A, 23A, pp. 3067-3072.

[51] Musuva, J. K. and Radon, J. C. (1979). The effect of stress ratio and frequency on fatigue crack growth. Fatigue of Engineering Materials and Structures, 1, pp. 457-470.

[52] Antolovich, S. D. and Jayaraman, N. (1983). The effect of microstructure on the fatigue behaviour of nickel base superalloys. Fatigue: Environmental and Temperature Effects, Plenum Press, New York, pp.119-144.

[53] Gayda, J. and Miner, R. V. (1983). The effect of microstructure 650°C fatigue crack growth in P/M Astroloy. Metall. Trans. A, 14A, pp. 2301-2308.

[54] Yeun, J. L. and Roy, P. (1985). Effect of grain size on the near threshold fatigue crack propagation of a nickel base precipitation hardened superalloy. Scripta Metall, 19, pp. 17-22.

[55] James, L. A. and Mills, W. J. (1985). Effect of heat treatment and heat to heat variations in the fatigue crack growth response of Alloy 718. Engng. Fract. Mech. 22, pp. 797-817.

[56] Suresh, S. (1983). Crack deflection implications for the growth of long and short fatigue cracks. Metall. Trans. A, 14A, pp. 2375-2385.

[57] Sengupta, A. and Putatunda, S. K. (1994). Influence of dynamic strain aging on the near threshold fatigue crack growth behaviour of a single crystal nickel based superalloy. Scripta Metall. Mater. 31, pp. 1163-1168.

[58] Hicks, M. A. and King, J. E. (1983). Temperature effects on fatigue thresholds and structure sensitive crack growth in a nickel base superalloy. Int. J. Fatigue, 5, pp. 67-74.

[59] Sadananda, K. and Shahinian, P. (1981). Analysis of crystallographic high temperature fatigue crack growth in a nickel base alloy. Metall. Trans. A, 12A, pp. 343-351.

[60] Arc Welding. (2003). Welding Processes Handbook. Woodhead Publishing Ltd.

[61] Ojo, O. A. (2004). On liquation Cracking of Cast Inconel 738LC Superalloy Welds. PhD Thesis. The University of Manitoba.

[62] Chryssolouris, G. (1991). Laser Machining, Theory and Practice. New York: Springer-Velag, pp. 17.

[63] Dahotre, B. N. and Harimkar, P. S. (2008). Laser Fabrication and Machining of Materials. New York, USA: Springer Science & Business Media, LLC.

[64] Kou, S. (2003). Welding Metallurgy. 2nd Edition, John Wiley and Sons Inc., Hoboken.

[65] David, S.A. and Viteck, J.M. (1992). Principle of weld solidification and microstructure in International trends in Welding Science Technology. p. 147.

[66] Solomon, H. D. (1983). Embrittlement of engineering alloys. Briant, C.L and Banjerji, S.K. (Eds.), Academic Press, New York, p. 525.

[67] Savage, W.F. and Nippes, E.F., Erickson, J.S. (1976). Solidification mechanisms in fusion welds. Weld. J., 55, p. 213s.

[68] Savage, W.F. et al. (1976). Microsegregation in partially melted regions in 70Cu-30Ni weldments. Weld. J., 55, p. 181s.

[69] Savage, W.F. et al. (1976). Microsegregation in 70Cu-30Ni weld metal. Weld. J., 55, p. 165s.

[70] Savage, W.F. et al. (1976). Study of weld interface phenomena in a low alloy steel. Weld. J., 55, p. 260s.

[71] Savage, W.F. (1980). Houdremont lecture: solidification, segregation and weld imperfections. Weld. World, 18, p. 89.

[72] Savage, W.F. et al. Weld metal solidification mechanics. Weld. J., 44 (4), p. 175s.

[73] Boettinger, W. J. et al. (1984). Mechanism of microsegregation-free solidification. Mater. Sci., Eng., 65(1), p. 27.

[74] Lancaster, J.F. (1993). Metallurgy of Welding. Chapman and Hall, New York.

[75] Bradley, E. F. (1988). A Technical Guide. ASM International, Metal Park OH, p. 206.

[76] Cieslak, M.J. (1993). Cracking Phenomenon associated with Welding. ASM Handbook, Welding, Brazing and Soldering, ASM International, 16, p. 88.

[77] Borland, J.C. (1960). Generalized theory of super-solidus cracking in welds (and Castings. Brit. Weld. J., 7(8), p. 508.

[78] Radhakrishnan, B. and Thompson, R.G. (1991). A phase diagram approach to study liquation cracking in alloy 718. Metall. Trans. 22A, p. 887.

[79] Chaturvedi, M.C. (2007). Liquation cracking in Heat Affected Zone in Ni-Superalloy Welds. Materials Science Forum, 546-549, p. 1163.

[80] Owczarski, W.A. et al. (1971). A model for Heat Affected Zone cracking in Nickel-Base Superalloy. Welding J., 50, p. 145.

[81] Lin, W. et al. (1993). Analysis of weldability testing technique for heat affected zone liquation cracking. Weld. J., 71(4), p. 135s.

[82] Barsom, J. M. and Stanley, T. R. (1999). Fracture and Fatigue Control in Structures: Applications of Fracture Mechanics. Third Edition. West Conshohocken, PA: American Society for Testing and Materials.

[83] Sims, C.T. et al. (1987). Superalloys II: High Temperature Materials for Aerospace and Industrial Power. John Wiley & Sons - Interscience publication, p. 3.

[84] Srivatsan, T. S. et al. (2004). The tensile deformation, cyclic fatigue and final facture behaviour of dispersion strengthened copper. Mechanics of Materials. 36, pp. 99-116.

[85] Gopinath, K. et al. (2009). Acta Mater. 57, pp. 3450–3459.

[86] Stahl, D. R. et al. (1988). Effect of Temperature, Microstructure, and Stress State on the Low Cycle Fatigue Behaviour of Waspaloy, America Society for Testing and Materials, Philadelphia, pp. 72–750.

[87] Ganesh, S. R. S. and Padmanabhan, K. A. (1994). Int. J. Fatigue 16 (3), pp. 209–215.

[88] Derek Hull, Introduction to Dislocations, first ed. (1965). Pergamon Press Ltd., Great Britain, p. 86.

[89] Lerch, B. A. and Gerold, V. (1987). Metall. Trans A, 18A, pp. 2135-2141.

[90] Wilhelm, M. (1981). Mater. Sci. Engng. 48, p. 91.

[91] Calabrese, C. and Laird C. (1974). Mater. Sci. Engng. 13, p.141.

[92] Lerch, B. A. and Gerold, V. (1985). Acta Metall. 33 (9), pp. 1709–1716.

[93] Clark, J. B. and McEvily, A. J. (1964). Acta Metall. 12, p.1359.

[94] Stubbington, C. A. and Forsyth, P. J. E. (1966) Acta Metall. 14, p. 5.

[95] Sundararaman, M. et al. (1990). TEM investigation of γ' free bands in Nimonic PE 16 under LCF loading at room temperature. Acta Metallurgica et Materialia. 38 (10), pp. 1813-1822.

[96] Lerch, B. A. and Jayaraman, N. (1984). Mater. Sci. Eng. 66, pp. 151–166.

[97] Begum, S. et al. (2009). Effect of Strain Ratio and Strain Rate on Low Cycle Fatigue Behaviour of AZ31 Wrought Magnesium Alloy. Materials Science and Engineering A.

[98] Kim, Y. W. et al. (2003). International Symposium on Gamma Titanium Aluminides, TMS, San Diego.

[99] Berteaux, O. et al. (2006). Intermetallics. p. 14.

[100] Henaff, G. and Gloanec, A. L. (2005). Intermetallics. p. 13.

[101] Praveen, K. V. U. et al. (2004). Room Temperature LCF Behaviour of Superalloy Inconel 718. Transactions of the Indian Institute of Metals. 57 (6), pp. 623-630.

[102] Nirbhay, S. et al. (2001). Bull. Mater. Sci. 24 (2), pp. 169–171.

[103] King, J. E. (1982). Met. Sci. 16 (7), pp. 345–355.

[104] King, J. E. (1981). Fatigue Eng. Mater. 4 (4), pp. 311–320.

[105] Pepe, J.J. and Savage, W.F. (1967). Effect of Constitutional Liquation in 18-Ni maraging steel weldment. Weld. J., 46, p. 411s.

[106] Vincent, R. (1985). Precipitation around welds in nickel-based superalloy IN 718. Acta Metall., 33, p.1205.

[107] Ernst, S. C. et al. Weldability of high-strength, low-expansion superalloys. Weld., J., 68(10), p. 418.

[108] Aronson, A.N. (1963). Constitutional liquation in the Iron-Iron Carbide system. MSc Thesis, Rensselaer Polythenic Institute, Troy, New York.

[109] Tamura, H. and Wantanabe, T. (1973). Mechanism of liquation cracking in the weld heat-affected zone of austenitic stainless steel. Trans. of the Japan Welding Soc., 2, p. 3.

[110] Mclean, D. (1957). Grain boundaries in Metals. Clarendon Press, Oxford.

[111] Hondros, E. D. and Seah, M. P. (1984). Interfacial and Surface microchemistry, in Physical Metallurgy. Ed. Cahn, R.W., 3rd Edition, North Holland, Amsterdam, p. 855.

[112] Mclean, M. and Strang, A. (1984). Effects of trace elements on mechanical properties of superalloys. Met. Technol., 11, p. 454.

[113] Westbrook, J. H. and Aust, K. T. (1963). Solute hardening at Interfaces in high purity lead. Acta Metall., 11, p. 1151.

[114] Aust, K. T. et al. (1968). Solute induced hardening near grain boundaries in zone refined materials. Acta Metall., 16, p. 291.

[115] Eadie, R. L. and Aust, K. T. (1970). Solute induced grain boundaries hardening in Aluminum. Scripta Metall., 4(8), p. 641.

[116] Aust, K. T. (1974). Selective segregation at grain boundaries. Canadian Metallurgical Quarterly, 13(1), p. 133.

[117] Karlsson, L. and Norden, H. (1988). Non-Equilibrium grain boundary segregation of boron in austenitic stainless steel, II fine scale segregation behaviour, precipitation behaviour and distribution of elements IV. Acta Metall., 36(1), p.13.

[118] Chen, W. and Chaturvedi, M. C. (1998). Grain boundary segregation of boron in IN 718. Metall. Mater. Trans. A., 29A, p.1947.

[119] Guttmann, M. (1975). Equilibrium segregation in a ternary solution: A model for temper embrittlement. Surf. Sci., 53, p. 213.

[120] Kujanpaa, V. P. et al. (1987). Characterisation of Heat Affected Zone cracking in austenitic stainless steel welds. Weld., J., 66, p 221s.

[121] Hoffelner, W. et al. (1979). Effect of Aging treatments on the microstructure of the Ni-based superalloy IN-738", Werktofftech, 10(84).

[122] Huang, X. and Chaturvedi, M. C. (1994). An investigation of microstructure and HAZ microfissuring of cast alloy 718, 625, 706 and various derivatives. (Ed. Loria E.A), p. 871.

[123] Huang, X. et al. (1997). The effects of grain boundary segregation of boron in cast alloy 718 on HAZ microfissuring- A SIMS analysis. Acta Materialia 45(8), p. 3095.

[124] Benhadad, S. et al. (2002). The influence of minor elements on weldability of IN 718 type superalloy. Metallurgical and Materials Transaction A., 33A, p.2005.

[125] Guo, H. et al. (2000). Effect of Sulphur on hot ductility and HAZ microfissuring in alloy 718 weld. Sci. and Technol. of Welding and Joining, 5(6), p.378.

[126] Guo, H. et al. (1999). Interdependence of character of grain boundaries, intergranular segregations of boron and grain boundary liquation in simulated weld heat affected zone in IN 718. Scripta Mater., 40(3), p. 383.

[127] Guo, H. et al. (1999). Effect of Boron concentration and grain size on Weld Heat Affected Zone Microfissuring in IN 718 base superalloys. The Sci. and Technol. of Welding and Joining, 4(4), p. 257.

[128] Idowu, O. I. et al. (2009). Crack free Electron beam welding of Allvac 718Plus Superalloy. Weld. J., 88 (8), p. 179s.

[129] Vishwakarma, K. and Chaturvedi, M.C. (2008) "A study of HAZ Microfissuring in a newly developed Allvac 718 Plus Superalloy. Superalloy TMS. p. 241.

[130] Lin, W. (1991). A methodology for quantifying heat affected zone liquation cracking susceptibility. PhD Dissertation. The Ohio State University, Columbus, Ohio.

[131] Qian, M. (2001). An Investigation of repair weldability of Waspaloy and Alloy 718. PhD Dissertation. The Ohio State University, Columbus, Ohio.

[132] Scott, W. S. (1991). A study of weld HAZ liquation cracking in Cast Ni-based superalloy. PhD Dissertation. The Ohio State University, Columbus, Ohio.

[133] Ojo, O. A. and Chaturvedi, M. C. (2007). Liquation Microfissuring in the weld Heat Affected Zone of an Overaged Precipitation-Hardened Nickel-base Superalloy. Metall. & Mater. Trans. A, 38A, p. 356.

[134] Owczarski, W. A. (1969). Some Minor Element Effects on Weldability of Heat Resistant Nickel Base Superalloys, in Effects of Minor Elements on the Weldability of High Nickel Alloys. Proceedings of a Symposium Sponsored by the Welding Research Council, New York, 6.

[135] Smith, C. S. (1948). Grains, Phases, and Interfaces: An interpretation of microstructure. Trans. AIME, 175, p. 15.

[136] Kokawa, H. et al. (1991). Effect of Grain boundaries on Isothermal solidification during transient liquid phase brazing. Metall., Trans. A. 29A (7), p. 1627.

[137] Askay, I. A. et al. (1974). Wetting under Chemical and Nonequilibrium Conditions", J. Phys. Chem., 78(12), p.1178.

[138] Chatain, D. et al. (2001). Role of Solid/Liquid interface faceting in rapid penetrations of a liquid phase along Grain boundaries. Acta Mater., 49, p. 1123.

[139] Lin, W. et al. (1993). Analysis of weldability testing technique for heat affected zone liquation cracking. Weld. J., 71(4), p. 135s.

[140] Lundin, C. D. et al. (1993). Weld HAZ characterization of modified 800 alloys, Proceedings of the International Trends in Welding Science and Technology", Gatlinburg, Tennessee, USA, 262, p. 65.

[141] Kelly, T. J. (1990). Welding metallurgy of investment cast Ni-based superalloys in Proc. Symp. on weldability of materials. Detroit, MI, ASM Inter. Patterson, R.A, and Mahin, K.W, (Eds)., Materials park, OH, p.151.

[142] Cam, G. and Kocak, M. (1998). Progress in Joining of Advance Materials. Int, Mater. Rev., 43(1), p.1.

[143] Thompson, R. G. (1988). Microfissuring of Alloy 718 in the weld Heat Affected zone. J. Met., 7, p. 44.

[144] Thakur, A. et al. (2003). On Crack-free welding of Inconel 738. Int. J. Join Mater., 15(14), p. 21.

[145] Malarvizhi, S. et al. (2008). Investigations on the influence of post weld heat treatment on fatigue crack growth behaviour of electron beam welded AA2219 alloy. International Journal of Fatigue. 30 (2008), pp. 1543-1555.

[146] Antolovich, S. D and Jayaraman, N. The effect of microstructure on the fatigue behaviour of Ni base superalloys. pp. 119-144.

[147] Lindigkeit, J. et al (1979). The effect of grain size on the FCP behaviour of age hardened alloys in inert and corrosive environment. Acta. Met., 27, pp. 1717-1726.

[148] King, J. E. (1982). Effects of grain size and microstructure on threshold values and near threshold crack growth in powder-formed Ni-base superalloy. Metal Science. 16, pp. 345-355.

[149] Ashyby, M. F. (1970). The deformation of plastically non-homogeneous materials. Philos. Mag., 21, 399

LIST OF PUBLICATIONS FROM THE PhD RESEARCH

1. Buckson, R. A. and Ojo, O. A. (2012). Cyclic deformation characteristics and fatigue crack growth behaviour of a newly developed aerospace superalloy Haynes 282. Materials Science and Engineering A, 555, pp. 63-70. (FULL PAPER – PUBLISHED)

2. Buckson, R. A. and Ojo, O. A. (2015). Analysis of the influence of laser welding on fatigue crack growth behaviour in a newly developed nickel-base superalloy. Journal of Materials Engineering and Performance, 24(1), pp. 353-361. (FULL PAPER – PUBLISHED)

3. Buckson, R. A. and Ojo, O. A. (2012). Low cycle fatigue and fatigue crack propagation behavior of a newly developed aerospace superalloy Haynes 282. Canada Society for Mechanical Engineering. CSME Conference. (FULL PAPER – PUBLISHED)

4. Buckson, R. A. and Ojo, O. A. (2011). Fatigue behaviour of a newly developed aerospace superalloy Haynes 282. Manitoba Institute for Materials. Manitoba Materials Conference.

5. Buckson, R. A. and Ojo, O. A. (2013). Increased fatigue crack growth resistance of a newly developed aerospace superalloy Haynes 282. Manitoba Institute for Materials. Manitoba Materials Conference.